Performance Testing of Aero-Naut CAM Folding Propellers

Or D. Dantsker[*] and Marco Caccamo [†]

Technical University of Munich, Garching, Germany

Robert W. Deters [‡]

Embry-Riddle Aeronautical University - Worldwide, Daytona Beach, FL 32114

Michael S. Selig[§]

University of Illinois at Urbana–Champaign, Urbana, IL 61801

The increase in popularity of unmanned aerial vehicles (UAVs) has been driven by their use in civilian, education, government, and military applications. However, limited on-board energy storage significantly limits flight time and ultimately usability. The propulsion system plays a critical part in the overall energy consumption of the UAV; therefore, it is necessary to determine the most optimal combination of possible propulsion system components for a given mission profile, i.e. propellers, motors, and electronic speed controllers (ESC). Hundreds of options are available for the different components with little performance specifications available for most of them. By examining a variety of existing long-endurance aircraft, Aero-Naut CAM carbon folding propellers were identified as the most commonly used type of commercial-off-the-shelf propeller. However, no performance data exist in the open literature for the Aero-Naut CAM carbon folding propellers. This paper describes the performance testing of 40 Aero-Naut CAM carbon propellers in 2-blade configuration with diameters of 9 to 16 in with various pitch values. The propellers were tested at rotation rates of 3,000 to 7,000 RPM and advancing flows of 8 to 80 ft/s, depending on the propeller and testing equipment limitations. Results are presented for the 40 propellers tested under static and advancing flow conditions with several key observations being discussed. The data produced will be available for download on the UIUC Propeller Data Site and on the Unmanned Aerial Vehicle Database.

Nomenclature

ESC	=	electronic speed controller	P	=	propeller power, propeller pitch
PWM	=	pulse width modulation	P/D	=	propeller pitch-to-diameter ratio
RPM	=	rotations per minute	Q	=	torque
UAV	=	unmanned aerial vehicle	R	=	universal gas constant
			Re	=	Reynolds number
c	=	chord	T	=	thrust, ambient temperature
C_P	=	power coefficient	V	=	flow speed
C_T	=	thrust coefficient			
D	=	propeller diameter	η	=	propeller efficiency
J	=	advance ratio	μ	=	viscosity
n	=	propeller rotation rate	ρ	=	density of air
p	=	ambient pressure			

[*]Researcher, Department of Mechanical Engineering, or.dantsker@tum.de
[†]Professor, Department of Mechanical Engineering, mcaccamo@tum.de
[‡]Assistant Professor, Department of Engineering and Technology, AIAA Member. detersr1@erau.edu
[§]Professor Emeritus, Department of Aerospace Engineering, AIAA Associate Fellow. m-selig@illinois.edu

American Institute of Aeronautics and Astronautics

I. Introduction

In recent years, there has been an uptrend in the popularity of UAVs driven by the desire to apply these aircraft to areas such as precision farming, infrastructure and environment monitoring, surveillance, surveying and mapping, search and rescue missions, weather forecasting, and more. A key commonality across the aforementioned applications is the necessity of sensing. Notably, the majority of the aforementioned applications require continuous collection and processing of visual data (e.g. visible, IR, UV, and multi-spectral). The traditional approach for small size UAVs is to capture data on the aircraft, stream it to the ground through a high power data-link, process it remotely (potentially off-line), perform analysis, and then relay commands back to the aircraft as needed.[1–3] Since the inception of unmanned aircraft, a key design constraint has been energy storage as limited on-board energy storage significantly limits flight time and ultimately usability. Given the finite energy resources found onboard an aircraft (battery or fuel), traditional designs greatly limit aircraft endurance as significant power is required for propulsion, actuation, and the continuous transmission of visual data.

To truly enable a variety of applications, the overarching goal is to create a computationally-intensive, long-endurance solar-powered unmanned aircraft that would carry a high-performance embedded computer system to perform all required computations online and only downlink final results, saving a significant amount of energy. Currently, such an aircraft is in development: UIUC-TUM Solar Flyer,[4–6] which is shown in Fig. 1. The completed 4.0 m (157 in) wingspan aircraft will weigh approximately 2.5 kg (88 oz) and be instrumented with an integrated autopilot and high-fidelity data acquisition system with an integrated 3D graphics processing unit. Given the objective, to operate continuously during all-daylight hours, the aircraft will be powered by solar array, specifically gallium arsenide (GaAs) solar cells from Alta Devices, which hold the world record for solar efficiency and power density. The solar array will be used in conjunction with a maximum power point tracking (MPPT) charge controller and a small lithium polymer battery that will act as an energy buffer.

The critical choice in the UIUC-TUM Solar Flyer's development then becomes what type of propulsion system to use. A mission-based propulsion system optimization tool was developed[7] to select the most optimal combination of possible propulsion system components for a given mission profile, i.e. propellers, motors, and ESC. Currently, there

Figure 1: The UIUC-TUM Solar Flyer aircraft shown with solar arrays.

American Institute of Aeronautics and Astronautics

are hundreds of propeller and dozens of motor and ESC options in the radio control model market for an airframe of this size, yielding thousands of possible choices. Therefore, the problem becomes gathering component parameters with often scarce performance specifications. Based on examination of existing long endurance aircraft, Aero-Naut CAM carbon folding propellers[8] were identified as good candidates as these propellers are well known throughout the UAV industry.[9–12] However, little performance data exist in the open literature for the Aero-Naut CAM carbon folding propellers or other folding propellers. Figure 2 shows the profile of several Aero-Naut CAM carbon propellers (single blade is shown). Currently, a CAM 13×6.5 propeller is being used on the UIUC-TUM Solar Flyer, and based on recent testing, it is oversized for the application. Therefore, it was desired to test a range of Aero-Naut CAM folding propellers with diameters (D) of 9 to 13 in and a variety of pitches (P). Note that for completeness, 14 to 16 in CAM folding propellers were also tested in order to show that these larger blade propellers are indeed oversized for the UIUC-TUM Solar Flyer.

Previous works have measured the performance and efficiency parameters of propellers as well as other electric UAV propulsion system components. Brandt[13,14] and Uhlig[15,16] explored the performance of low-Reynolds number propellers at slow speeds and past stall. Lundstrom performed a similar test using an automotive-based testing rig.[17,18] Deters looked into the performance of propellers for both small/micro air vehicles,[19,20] later expanding his work to look at static performance of propellers for quadrotors.[21,22] Lindahl[23] tested large UAV propellers in a wind tunnel while Chaney[24] and Dantsker[25,26] did so using automotive based rigs. Lindahl also tested the effects of using different motors with a given propeller. Drela has done extensive work testing and modelling motors and propellers.[27–29] Green[30] and Gong[31] have modelled and tested the efficiency of ESCs. Gong has also tested a propeller-motor combination in a wind tunnel[32] as well as create an in-flight thrust measurement system.[33]

This paper describes the performance testing of 40 Aero-Naut CAM carbon folding propellers in 2-blade configuration with diameters of 9 to 16 in with various pitch values. In the following sections, the paper presents the experimental methodology, including the equipment, testing procedure, calibration, data reduction, and wind tunnel corrections. Results and discussion are then given including the performance results for the 40 propellers for static and advancing flow conditions. Finally, a summary and statement of future work is given.

Figure 2: A photo of several Aero-Naut CAM carbon folding propeller blades (taken from Aero-Naut[8]).

American Institute of Aeronautics and Astronautics

II.   Experimental Methodology

A.   Equipment

Propeller tests were conducted in the UIUC low-turbulence subsonic wind tunnel using a propeller testing balance adapted and validated to several previous works.[14, 16, 34] The wind tunnel is an open-return type with a 7.5:1 contraction ratio. The rectangular test section is 2.8×4.0 ft (0.853×1.22 m) in cross section and 8-ft (2.44-m) long. To account for the boundary-layer growth at the side wall, the width increases by approximately 0.5 in (1.27 cm) over the length of the test section. In order to have low turbulence levels at the test section, a 4-in (10.2-cm) honeycomb and four anti-turbulence screens are in the settling chamber. The resulting turbulence intensity for an empty tunnel has been measured to be less than 0.1%.[35] A 125-hp (93.2-kW) AC motor driving a five-bladed fan is used to control the test-section speed up to 160 mph (71.5 m/s). The maximum test-section speed for these tests was 80 ft/s (24.4 m/s). Test-section speeds were measured using a MKS differential pressure transducer connected to static ports at the settling chamber and at the beginning of the test section. For test-section speeds below 40 ft/s, a MKS 220 1-torr transducer was used, and for speeds greater than 40 ft/s, a MKS 221 10-torr transducer was used. Ambient pressure was measured using a Setra Model 270 pressure transducer, and ambient temperature was measured using an Omega GTMQSS thermocouple.

Propeller performance was measured using the thrust and torque balance shown in Fig. 3. Thrust was measured outside of the tunnel test section using a T-shaped pendulum balance that pivoted about two flexural pivots and was constrained on one side by a load cell.[13] Interface SM S-Type load cells with load capacities of 25 lb (111 N) were used. The balance was designed to allow the load cell to be placed in 10 different locations in order to use the full range of the load cell based on the thrust produced. The load cell locations ranged from 3.25 in (8.26 cm) from the pivot point to 7.75 in (19.69 cm) in 0.5-in (1.27-cm) increments. A preload weight was added to the balance on the opposite side to the load cell. This preload weight kept the load cell in tension during all aspects of testing to make sure the load cell would not slip during negative thrust conditions at high advance ratio.

The torque from the propeller was measured using a 100 oz-in (0.708 N-m) reaction torque sensor (RTS) from Transducer Techniques. The torque cell was placed between the motor sting and the support arm of the thrust balance. To remove the torque cell, motor sting, balance support arm, and any wires from the propeller slipstream and test section velocity, a fairing surrounded the setup as shown in Fig. 4. The fairing spanned the test section from the floor to the ceiling in order to keep the test section flow symmetric. The motor sting was long enough for all the propellers to be more than 1.5 diameters from the fairing in order to minimize the effect of the fairing on the propeller performance.

Propeller RPM was measured by shining a red laser with a wavelength of 630–680 nm through the propeller disc area to a phototransistor with a rise time of 5 μsec. The output from the phototransistor was amplified so that the maximum voltage when the laser shines on the receiver was over 5 V. As the propeller spins, the propeller blades block the laser beam, and the receiver output voltage drops to around zero. Each time the propeller RPM was measured, the voltage was recorded at 40,000 Hz for 30,000 samples. The high rate and sample number was used so that the resulting square wave was captured and the voltage peaks could be counted. The RPM was calculated by dividing the number of peaks by the sample time and by the number of propeller blades (2). The phototransistor rise time and the sample rate have been more than sufficient in finding the typical RPM values for the propellers tested. This measurement technique was compared to results from a handheld digital tachometer, and the results agreed.

During the tests, the propellers were driven by the Hacker A40-14L 14-pole (355 kV) brushless electric motor using a Castle Creations Edge 75 electronic speed controller (ESC). The propeller blades were mounted to the motor using a 2-bladed, 40mm diameter Aero-Naut Folding Turbo spinner using a 42 mm diameter Aeronaut yoke; using this hinged mounting setup, the blades are free to rotate forwards/backwards. To simplify the laboratory setup, a Mean Well
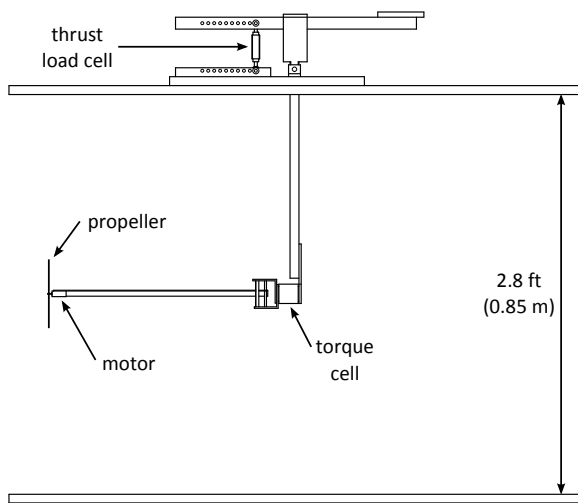
Figure 3: Propeller thrust and torque balance.
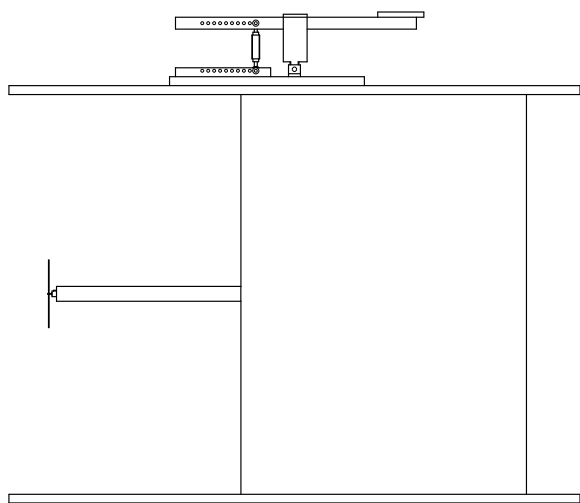
Figure 4: Propeller balance enclosed in fairing.

SE-1500-27, 27 V, 1500 W power supply was used to power the motor and speed controller. To set the rotational speed of the motor, the speed controller was connected to a modified ServoXciter EF from Vexa Control. While designed to test RC servos by adjusting the pulse width modulation (PWM) signal to the servo, the ServoXciter also works well as the throttle for the motor. A voltage from the computer would be sent to ServoXciter, and in turn the ServoXciter would then send a pulse-width signal to the speed controller to control the motor speed.

B. Testing Procedure

All voltages from the testing equipment were recorded by a National Instruments PCI-6031E 16-bit analog-to-digital data acquisition (DAQ) board connected to a personal computer. The DAQ board is capable of measuring 32 differential analog inputs simultaneously at a maximum sample rate of 100 kS/s. As mentioned earlier, propeller RPM measurements were recorded at 40,000 Hz for 30,000 samples. This high sample rate required the RPM measurement to be taken separately from the rest of the measurements. All other measurements (thrust, torque, dynamic pressure, atmospheric pressure, and temperature) were taken simultaneaously immediately afterwards at a rate of 3,000 Hz for 3,000 samples. This method has been more than suffecient as differences in motor speed have been observed to change less than 1% during these time periods. A LabVIEW® program was written to read the DAQ board as well as control the motor speed and wind tunnel speed.

For static performance tests, the propeller thrust and torque were measured along with the ambient pressure and temperature at different RPM values. For advancing flow performance tests, the propeller RPM was set and the tunnel speed was increased from 8 ft/s to 40 ft/s by 2 ft/s increments. During this test, a MKS 1-torr pressure transducer was used to measure the tunnel speed. At each velocity, the propeller thrust and torque were measured along with the tunnel speed and ambient pressure and temperature. If the torque value became too close to zero, the test was stopped because the propeller was approaching the windmill brake state. If the propeller reached 40 ft/s before the windmill brake state was achieved, the same RPM was used for tunnel speeds of 34 ft/s to 80 ft/s by 2 ft/s increments using a MKS 10-torr transducer to measure the tunnel speed. Again the test would terminate early if the propeller was close to windmilling.

American Institute of Aeronautics and Astronautics

The overlap with the 1-torr and 10-torr tests were to ensure consistent data between low and high speed tests. Typically at least three RPM values were tested to measure any Reynolds number effects.

C. Calibration

Since the DAQ board only records voltages from the transducers and load cells, each voltage is converted to a physical measurement through calibration curves. The pressure transducer that measured the ambient pressure and the thermocouple that measured ambient temperature used manufacturer supplied calibration equations to convert the voltages to pressure and temperature. The MKS differential pressure transducers used to measure tunnel pressures also used manufacturer calibration slopes.

The load and torque cells do not use manufacturer supplied calibration values. Instead the calibration slopes are found during testing. Thrust calibration used precisely measured weights and a pulley system to create a "thrust" on the load cell. By increasing and decreasing a known force on the load cell, a linear relationship between the thrust and voltage was calculated. For torque calibration, the precision weights were used with a moment arm to create a known torque. By increasing and decreasing this torque, a linear relationship between the torque and voltage was calculated. These calibration proceedures were performed regularly to ensure consistent results, and any change in the slopes were typically 1% or less. Additionally, a validation test was performed where a previously tested propeller was re-tested, which showed excellent agreement.

D. Data Reduction

As mentioned in Section A, the ambient pressure and temperature were measured using a pressure transducer and thermocouple, respectively. Air density was then calculated from the equation of state

$$p = \rho RT \tag{1}$$

where R is the universal gas constant. The standard value of 1716 ft^2/s^2/°R (287.0 m^2/s^2/K) for air was used.

Propeller power is calculated from the measured propeller torque by

$$P = 2\pi nQ \tag{2}$$

Performance of a propeller is typically given in terms of the thrust and power coefficients, defined as

$$C_T = \frac{T}{\rho n^2 D^4} \tag{3}$$

$$C_P = \frac{P}{\rho n^3 D^5} \tag{4}$$

where nD can be considered the reference velocity and D^2 can be considered the reference area. When the propeller is in a freestream flow, the advance ratio is defined in terms of the velocity and the rotation rate.

$$J = \frac{V}{nD} \tag{5}$$

The efficiency of a propeller is a measure of the useful power (TV) divided by the input power (P).

$$\eta = \frac{TV}{P} \tag{6}$$

Putting the efficiency in term of C_T, C_P, and J yields

$$\eta = \frac{C_T J}{C_P} \tag{7}$$

American Institute of Aeronautics and Astronautics

E. Wind Tunnel Corrections

Two wind tunnel corrections were used to account for the effects of testing a propeller in front of a fairing and in a closed test section. Since the propellers are tested on a sting in front of a fairing, the air velocity seen by the propellers will be less than the velocity measured at the begining of the test section. To account for this lower velocity, a velocity correction factor was developed based on the propeller size and its distance from the fairing.

Since the fairing spanned the test section from the floor to ceiling, the fairing was modeled as an airfoil using source panels. In order to satisfy the boundary condition of no cross flow at the tunnel side walls, reflections of the airfoil were included. The strength of each source panel and the flowfield surrounding the airfoil was then found using the method described in Anderson.[36] Using 100 sets of reflection pairs, the cross flow at the tunnel side walls was found to be less than $2 \times 10^{-6}\%$ of the freestream. The resulting 2D flowfield from the source panels was assumbed to be the same along the span of the fairing.[20] The propeller size is small compared to the height of the tunnel, so any wall effects from the floor and ceiling were assumed to be negligible. Since the propeller will see different corrected velocities along its disk area, a weighted average was used to calculate a single velocity reduction factor $k_{fairing}$ expressed as

$$\frac{V_{c_{fairing}}}{V_{\infty}} = k_{fairing} \tag{8}$$

In order to simplify the calculations needed during testing, a series of correction factors were tabulated beforehand covering the full range of propeller sizes and locations. During a test, the correction factor was found by interpolation using the current propeller size and location.

To account for testing a propeller in a closed test section, the classic Glauert[37,38] correction was used. The flow around a propeller in a closed test section is different than the flow in free air. For a propeller producing thrust, the velocity in the propeller slipstream is greater than the nominal test section velocity. Since the same volume of air must pass ahead of the propeller as it does behind the propeller from continuity, the velocity outside of the slipstream must be lower. The pressure outside of the slipstream is also higher than the pressure ahead of the propeller, so the thrust measured is larger than the thrust produced at the same velocity in free air. Another way to describe the results is that the thrust measured would occur at a lower velocity in free air. To determine that lower velocity, the correction factor is found from

$$\frac{V_c}{V_{\infty}} = 1 - \frac{\tau \alpha}{2\sqrt{1+2\tau}} \tag{9}$$

where $\tau = T/\rho A V_{\infty}^2$ and $\alpha = A/C$. This correction is the first approximation of the iterative method described by Glauert, but for the propeller sizes, thrust values, and freestream speeds from this series of tests, the correction factor from Eq. 9 agrees with the full iterative method to a difference of less than 1%.

III.   Results and Discussion

A total of 40 Aero-Naut CAM carbon folding propellers, with diameters from 9 to 16 inches, were tested in static conditions (no-freestream) and in advancing flow in the wind tunnel. Table 1 lists the specific diameters and pitches for the propellers that were tested. The static and wind tunnel performance data of these propellers are presented in Figs. 5–86. This data will be available for download on the UIUC Propeller Data Site[39] and on the Unmanned Aerial Vehicle Database.[40] Several trends were observed during testing and from the results generated, which are discussed below.

First, it was visually observed that propellers with the same diameter but different pitch numbers had different blade geometries. This observation is important to note as propeller manufactures often use the same geometry for different pitch propellers and only vary the blade incidence to achieve varied pitches. However, this is not the case with the

Aero-Naut CAM carbon folding propellers. It was confirmed through caliper measurements that the maximum chord varies among different pitch propellers for a given diameter. This difference in geometry existed for each diameter that was tested for this paper.

It was also observed that the geometry of propellers with a given pitch-to-diameter (P/D) ratio were not merely scaled between diameters, i.e. the geometry of the 16×8 propeller (P/D=0.5) is not a scaled-up version of the geometry of the 13×6.5 propeller, nor is it of 10×5 propeller. Thus, given different geometries for identical pitch-to-diameter (P/D) ratios, propeller performance cannot simply be Reynolds number scaled based on diameter and RPM as it would be for identically scaled propellers.[20] For example, the 7,000 RPM curves for the 13×6.5 propeller in Fig. 61 would scale to approximately 4,600 RPM for the 16×8 propeller, i.e. between the 4,000 and 5,000 RPM curves in Fig. 85; although the thrust and power coefficient curves are visually similar for the two propellers, the efficiency curves show a pronounced difference. The 16×8 propeller reaches an estimated peak efficiency of 81% at an advance ratio of 0.53 for approximately 4,600 RPM while the 13×6.5 propeller reaches a peak efficiency of 74% at an advance ratio of 0.42 for 7,000 RPM. The implications of this observation is that performance testing must be done for any Aero-Naut CAM carbon folding propeller of interest in order to determine its performance.

Next, it was observed that with increasing pitch for a given propeller diameter, the thrust, power, and efficiency coefficient curves shift up and to the right, correlating to greater values at greater advance ratios; this general trend is expected. This effect is visible up to pitch-to-diameter ratios of approximately 0.8 to 1.0, depending on the propeller diameter; as stated above, since the propeller geometries are different between different propeller diameters, trends vary between propellers. Beyond a P/D ratio of 0.8 to 1.0, the curves flatten out with decreases in performance and efficiency for some diameters. However, the propellers with P/D ratios of greater than 0.8 to 1.0 are able to operate at much greater advance ratios than those propellers with lower P/D ratios; this type of tradeoff is required where propeller diameter becomes constrained while thrust and/or velocity targets must still be met, e.g. aircraft configuration/geometry limiting propeller clearance. It should be noted that the performance curves for propellers with high P/D ratios are incomplete because of the 80 ft/s speed limitation set by the structural design of the propeller balance fairing.

Similarly as expected, as pitch increases for a given propeller diameter, the static (zero velocity) thrust and power coefficients increases. The power coefficient curve, which starts with values of approximately half the thrust coefficient curve, is observed to increase much more rapidly than the thrust coefficient curve. For propellers with P/D ratios of greater than 1.0, the curves sometimes overlap.

Finally, it was observed that with increasing RPM for a given propeller, the performance and efficiency will increase up to a certain RPM value . This effect is well observed in the literature and is due to Reynolds number effects at low RPMs dampening performance and efficiency. Therefore, once RPM is sufficiently high, these effects lessen and performance and efficiency is approximately constant. These effects are more visible for propellers with smaller diameters and therefore blade chords, which are thus operating at lower Reynolds number.

American Institute of Aeronautics and Astronautics

Table 1: List of Aero-Naut CAM Carbon Folding Propellers Tested

Aero-Naut CAM Carbon Folding Propellers									
9×4	10×4	11×4	12×5	12.5×6	13×5	14×6	15×6	16×6
9×5	10×5	11×6	12×6	12.5×7	13×6.5	14×8	15×8	16×8
9×6	10×6	11×7	12×6.5	12.5×9	13×8	14×9	15×10	
9×7	10×7	11×8	12×8		13×10	14×12		
	10×8	11×10	12×9		13×11			
	10×12	11×12	12× 10					
			12× 13					

Aero-Naut CAM 9×4 Folding Propeller

(a)

(b)

(c)
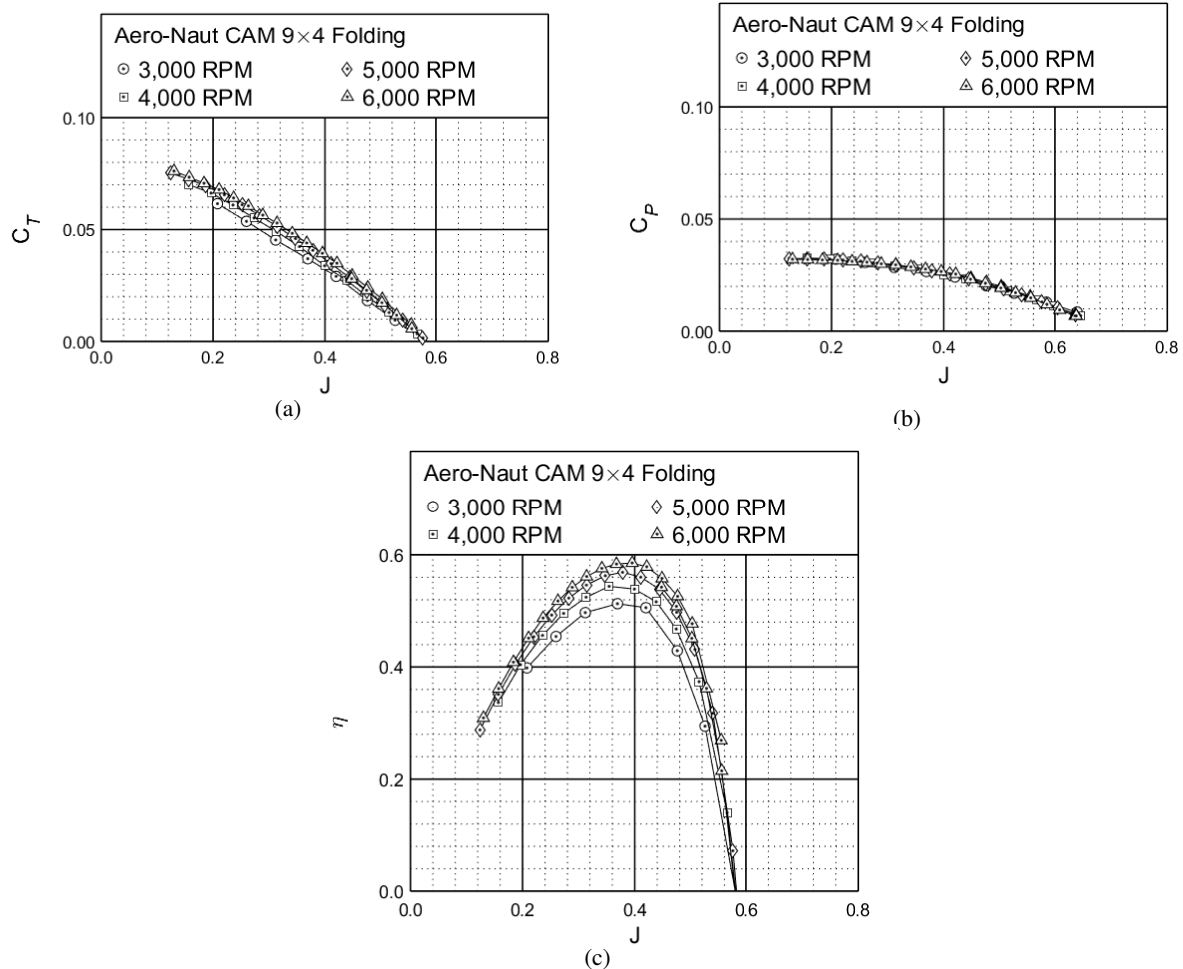
Figure 5: Performance of the Aero-Naut CAM 9×4 folding propeller: (a) thrust coefficient, (b) power coefficient, (c) efficiency.

American Institute of Aeronautics and Astronautics
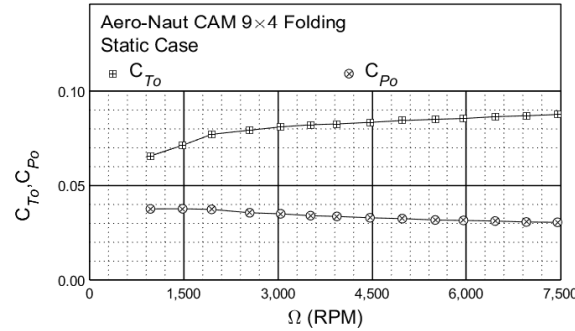
Figure 6: Static performance of the Aero-Naut CAM 9×4 folding propeller: thrust and power coefficient.

**Aero-Naut CAM 9×5 Folding Propeller**

(a)

(b)

(c)
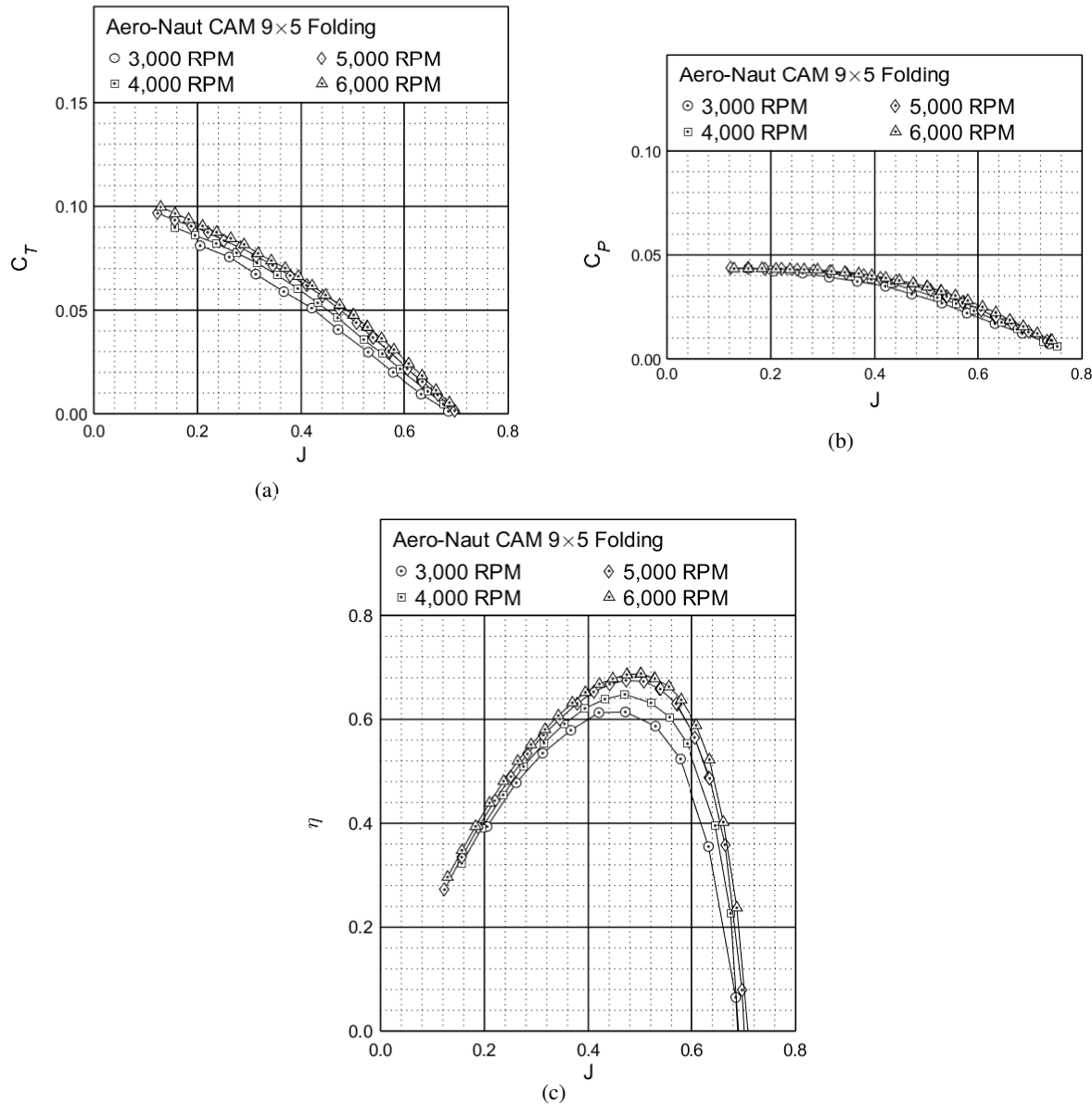
Figure 7: Performance of the Aero-Naut CAM 9×5 folding propeller: (a) thrust coefficient, (b) power coefficient, (c) efficiency.
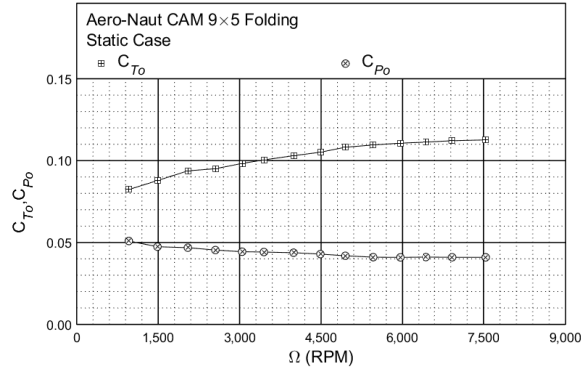
Figure 8: Static performance of the Aero-Naut CAM 9×5 folding propeller: thrust and power coefficient.

**Aero-Naut CAM 9×6 Folding Propeller**

(a)

(b)

(c)
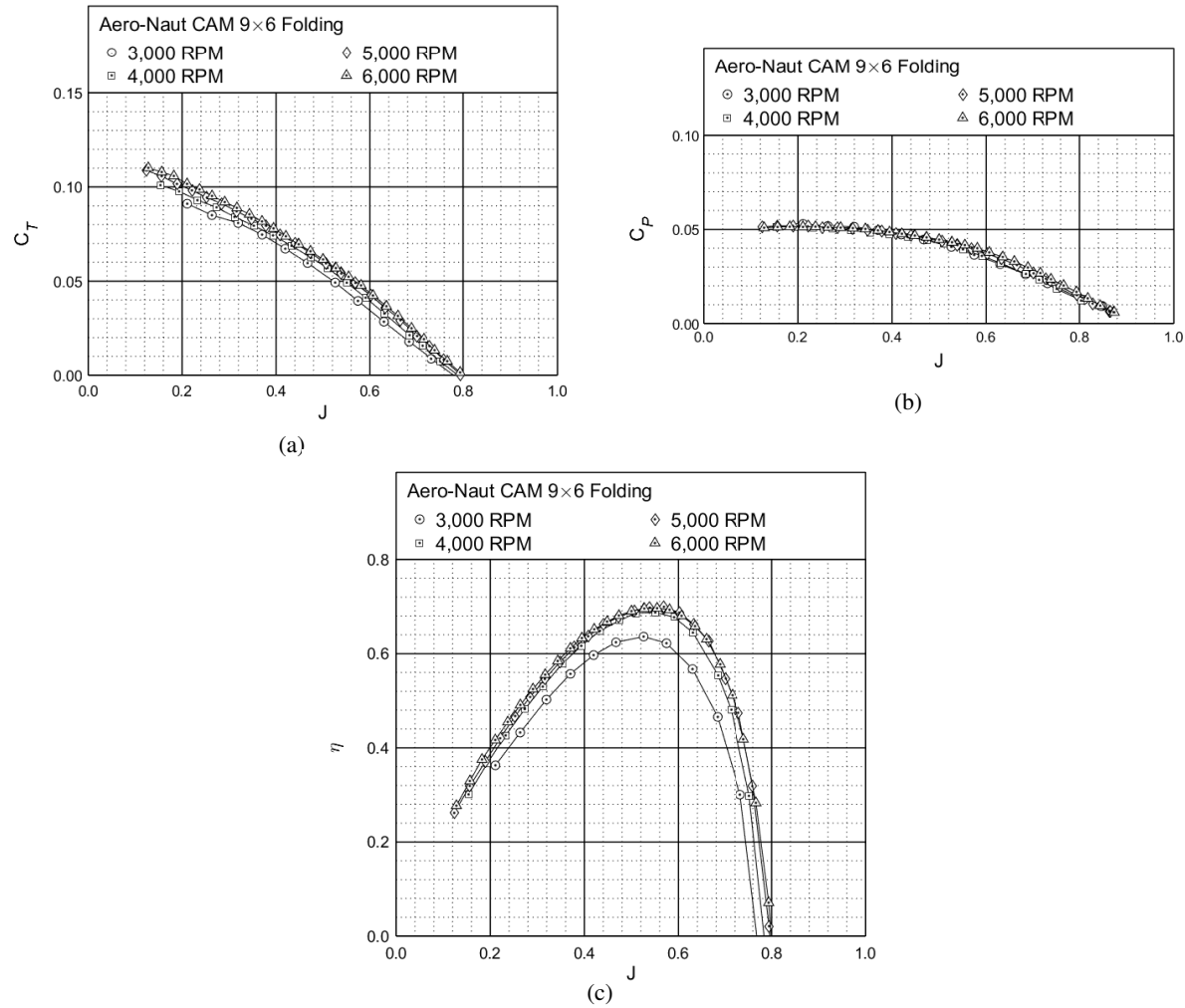
Figure 9: Performance of the Aero-Naut CAM 9×6 folding propeller: (a) thrust coefficient, (b) power coefficient, (c) efficiency.
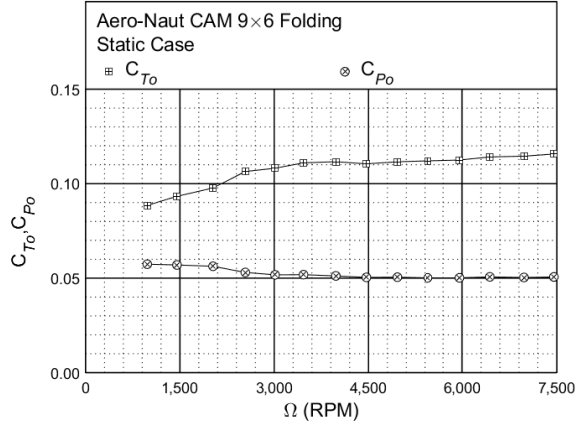
Figure 10: Static performance of the Aero-Naut CAM 9×6 folding propeller: thrust and power coefficient.

Aero-Naut CAM 9×7 Folding Propeller

(a)

(b)

(c)
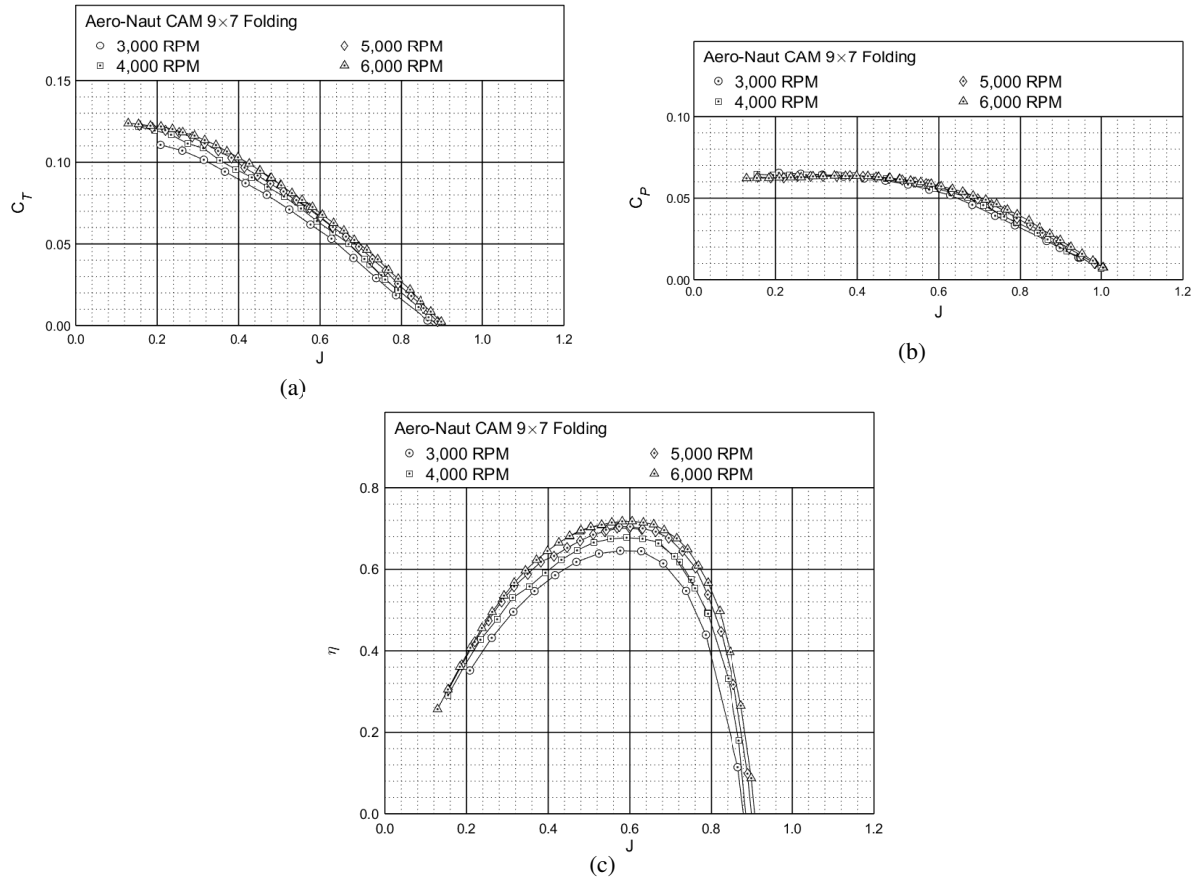
Figure 11: Performance of the Aero-Naut CAM 9×7 folding propeller: (a) thrust coefficient, (b) power coefficient, (c) efficiency.
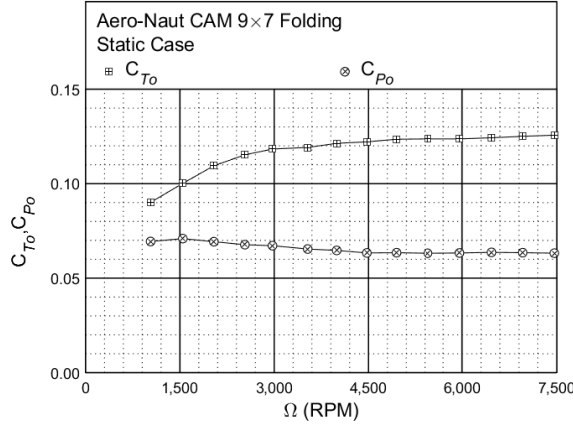
Figure 12: Static performance of the Aero-Naut CAM 9×7 folding propeller: thrust and power coefficient.

Aero-Naut CAM 10×4 Folding Propeller

(a)

(b)

(c)
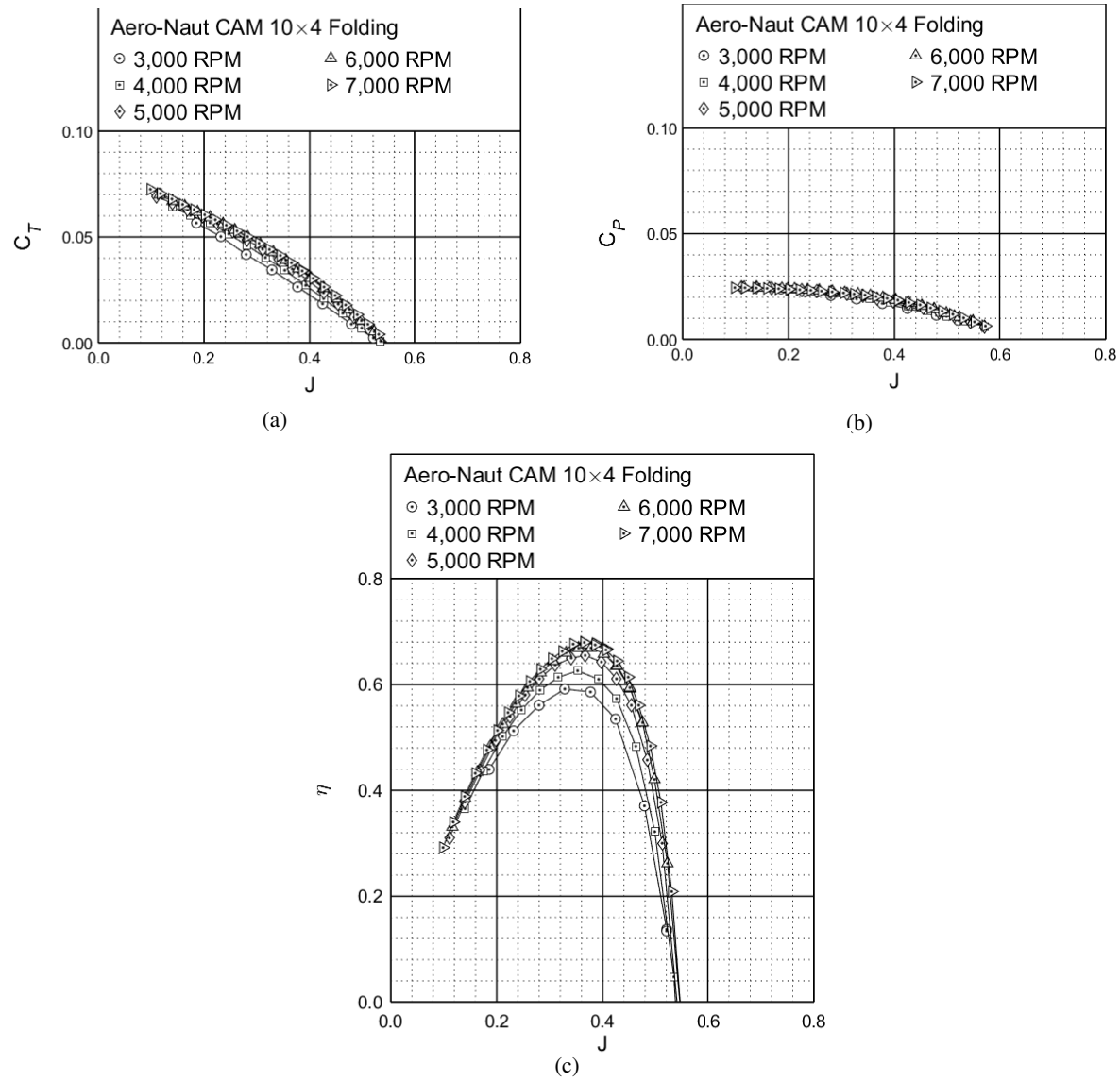
Figure 13: Performance of the Aero-Naut CAM 10×4 folding propeller: (a) thrust coefficient, (b) power coefficient, (c) efficiency.

American Institute of Aeronautics and Astronautics
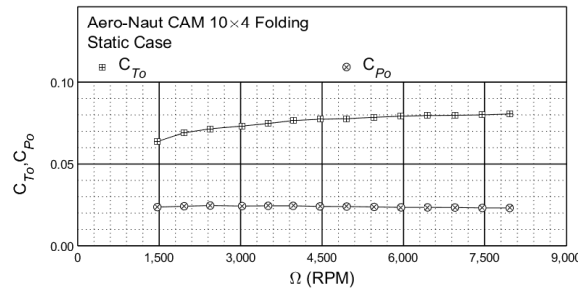
Figure 14: Static performance of the Aero-Naut CAM 10×4 folding propeller: thrust and power coefficient.

Aero-Naut CAM 10×5 Folding Propeller

(a)

(b)

(c)
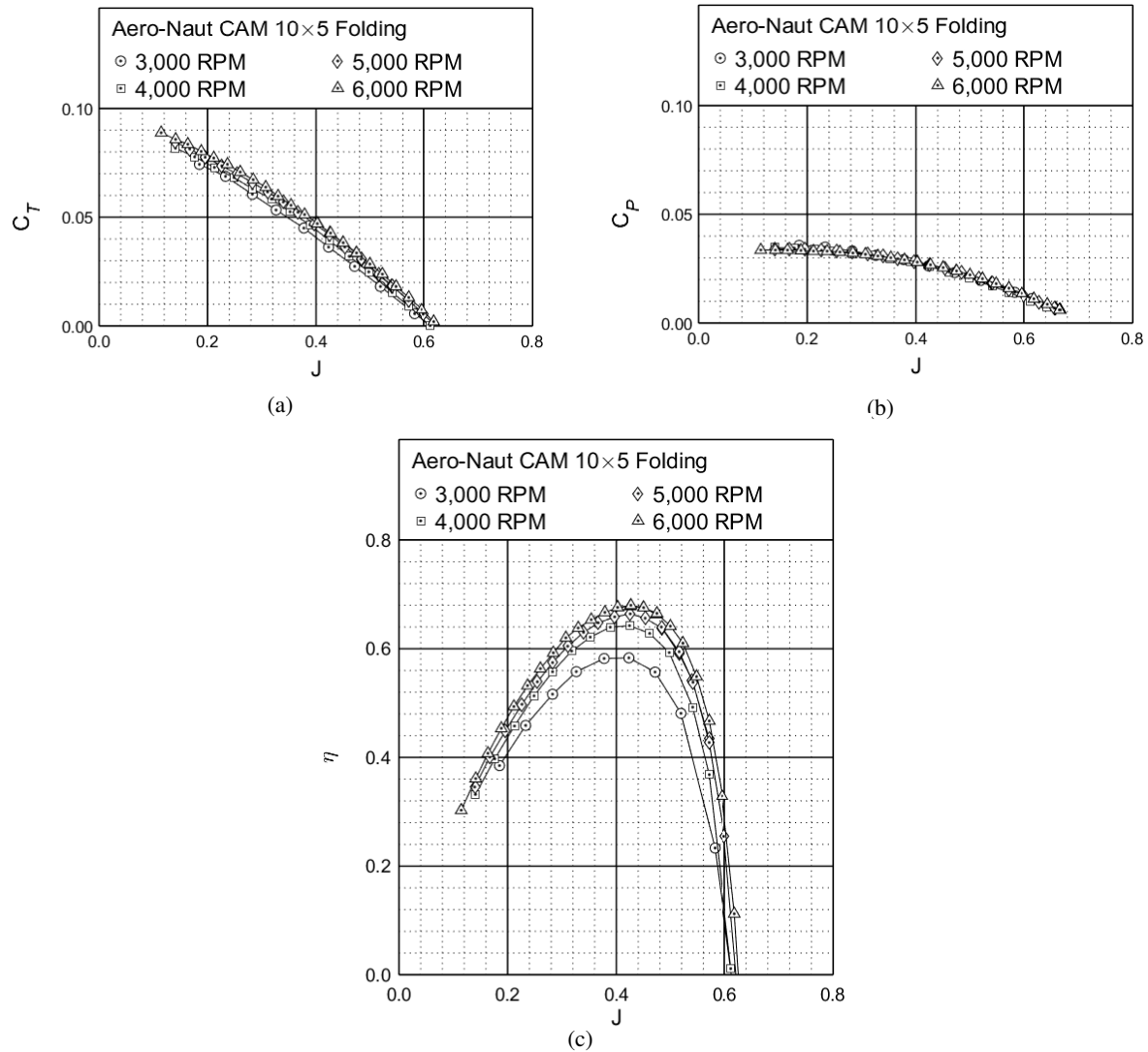
Figure 15: Performance of the Aero-Naut CAM 10×5 folding propeller: (a) thrust coefficient, (b) power coefficient, (c) efficiency.

American Institute of Aeronautics and Astronautics
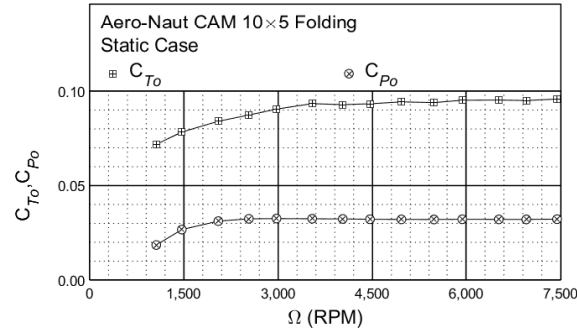
Figure 16: Static performance of the Aero-Naut CAM 10×5 folding propeller: thrust and power coefficient.

Aero-Naut CAM 10×6 Folding Propeller



(a)

(b)

(c)
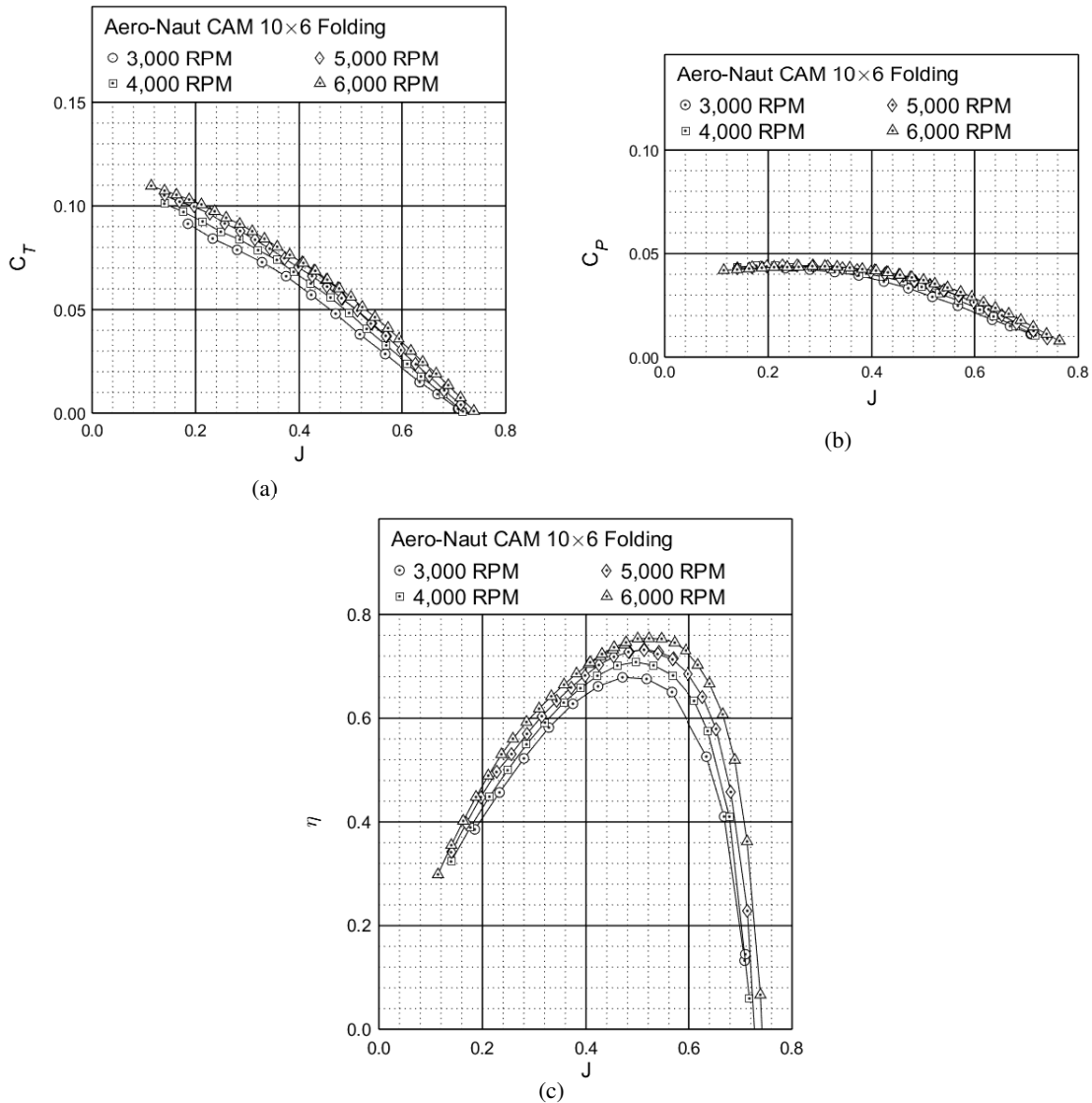
Figure 17: Performance of the Aero-Naut CAM 10×6 folding propeller: (a) thrust coefficient, (b) power coefficient, (c) efficiency.
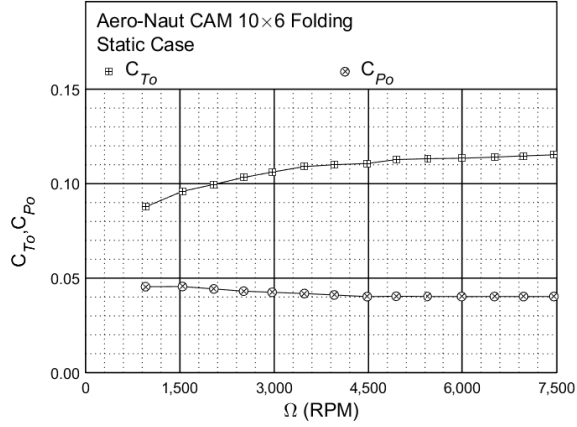
Figure 18: Static performance of the Aero-Naut CAM 10×6 folding propeller: thrust and power coefficient.

Aero-Naut CAM 10×7 Folding Propeller


(a)

(b)

(c)
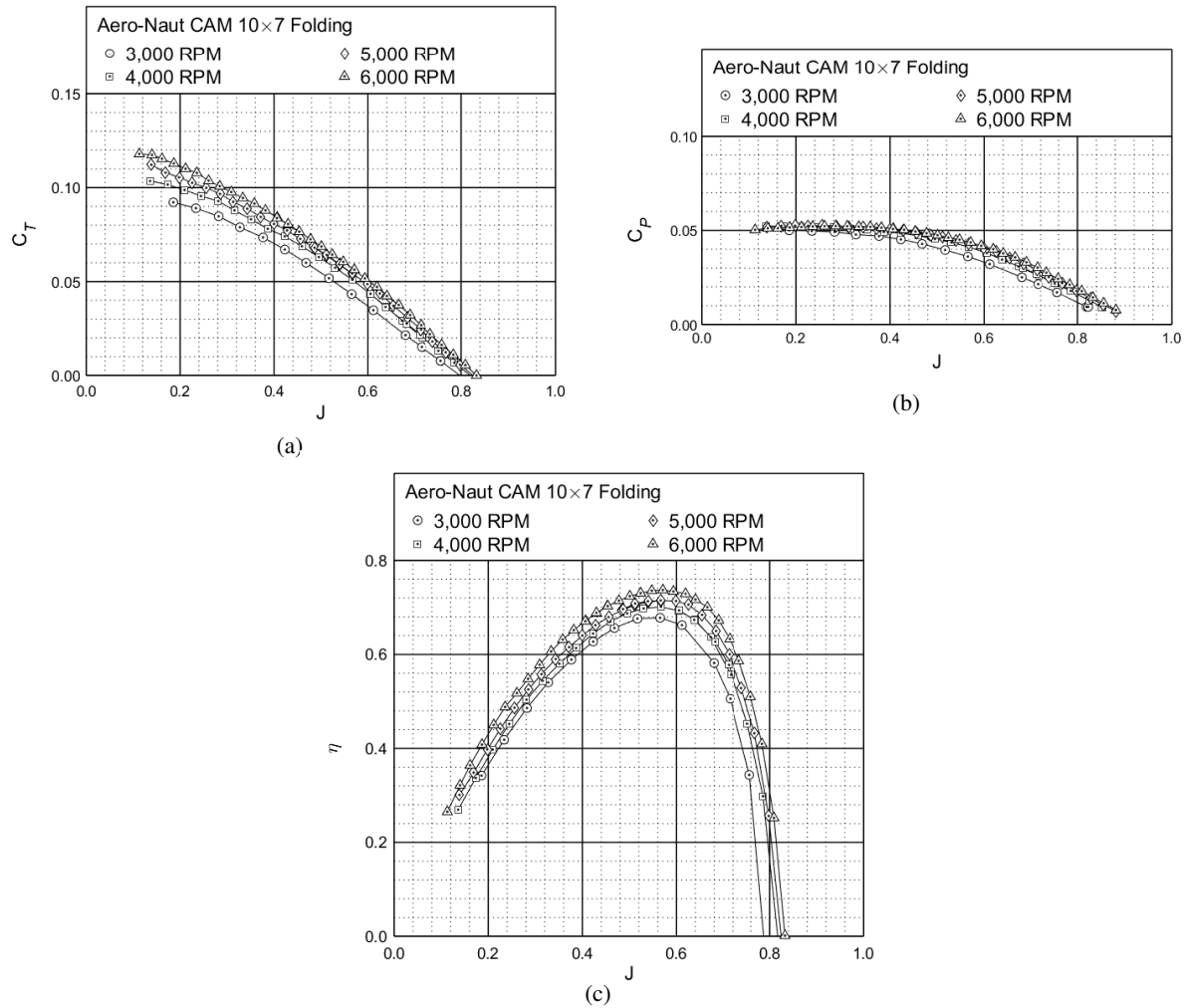
Figure 19: Performance of the Aero-Naut CAM 10×7 folding propeller: (a) thrust coefficient, (b) power coefficient, (c) efficiency.
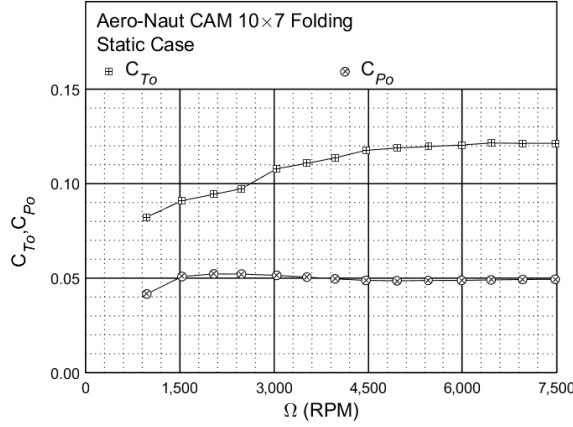
Figure 20: Static performance of the Aero-Naut CAM 10×7 folding propeller: thrust and power coefficient.

Aero-Naut CAM 10×8 Folding Propeller

(a)

(b)

(c)
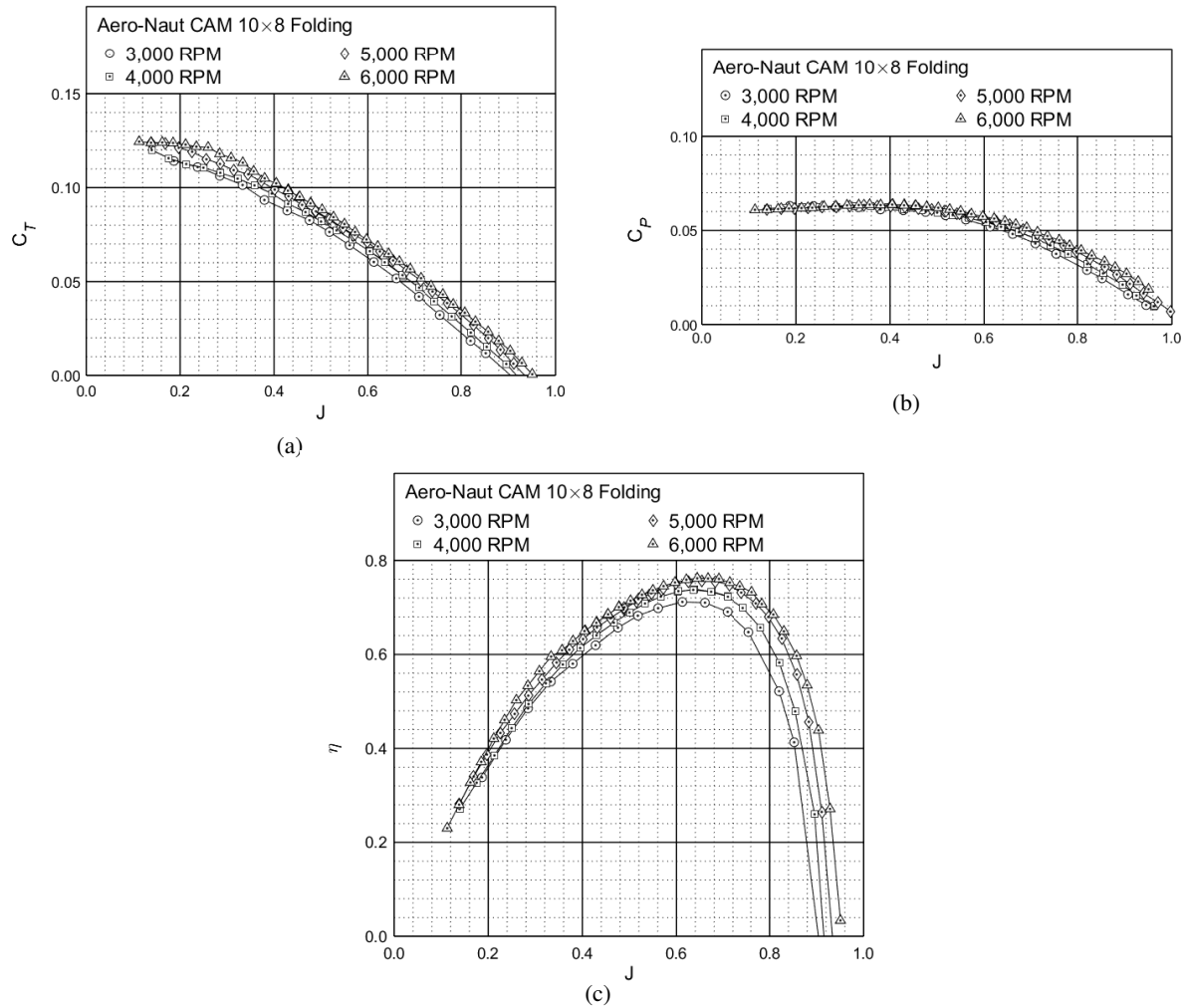
Figure 21: Performance of the Aero-Naut CAM 10×8 folding propeller: (a) thrust coefficient, (b) power coefficient, (c) efficiency.

American Institute of Aeronautics and Astronautics
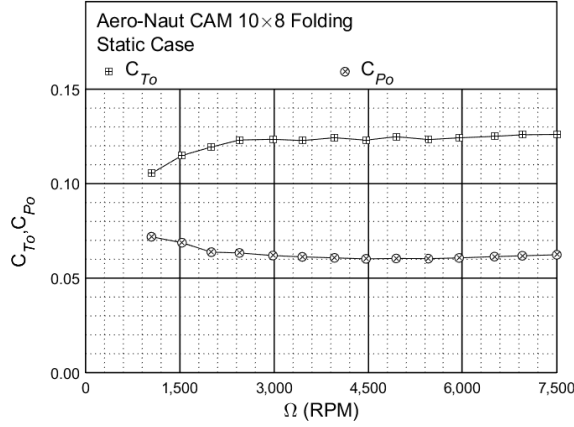
Figure 22: Static performance of the Aero-Naut CAM 10×8 folding propeller: thrust and power coefficient.

## Aero-Naut CAM 10×12 Folding Propeller

(a)

(b)

(c)
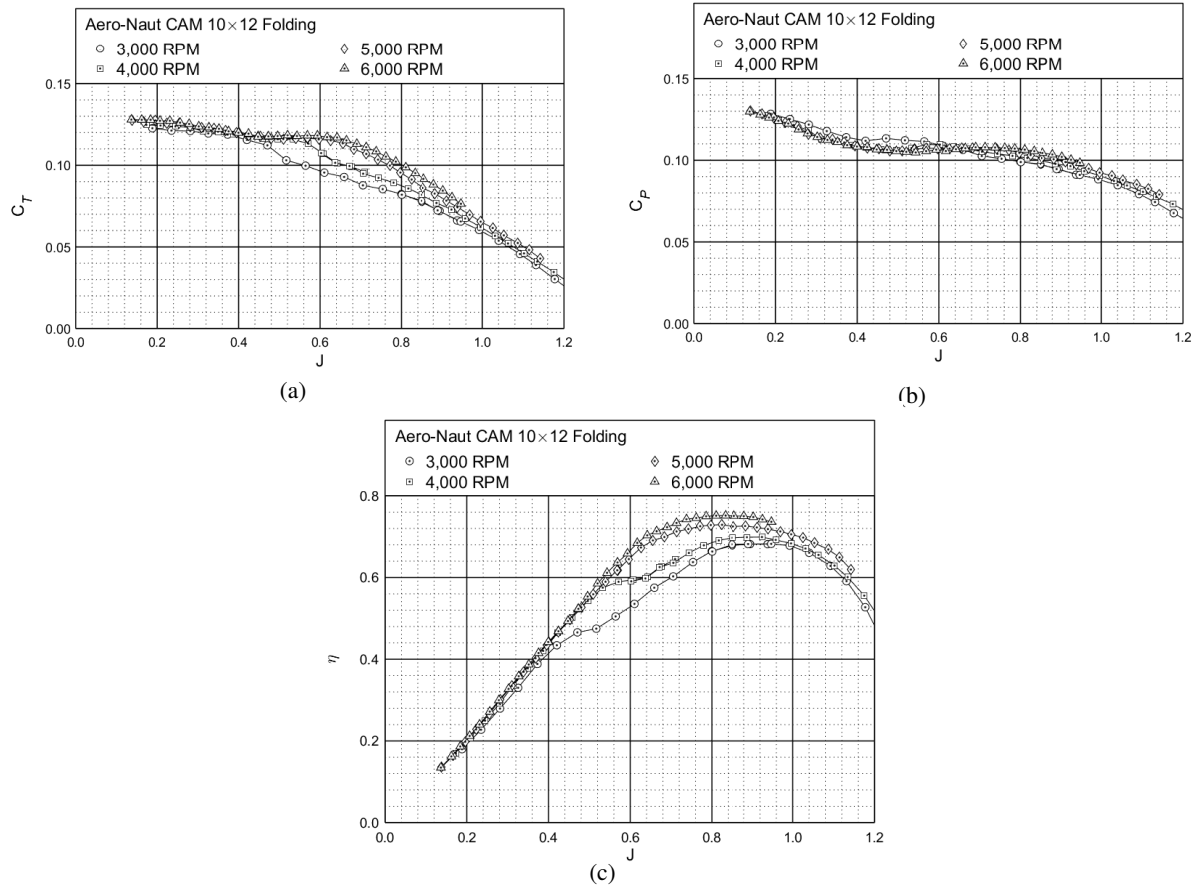
Figure 23: Performance of the Aero-Naut CAM 10×12 folding propeller: (a) thrust coefficient, (b) power coefficient, (c) efficiency.
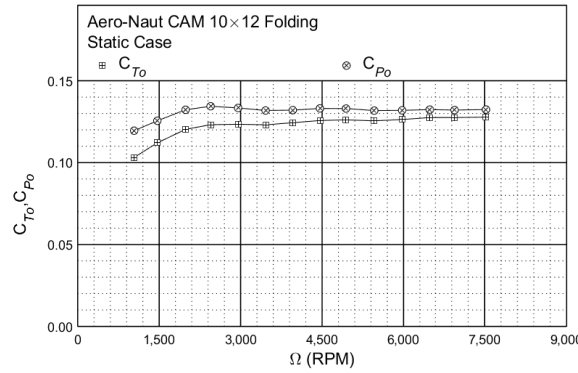
Figure 24: Static performance of the Aero-Naut CAM 10×12 folding propeller: thrust and power coefficient.

Aero-Naut CAM 11×4 Folding Propeller

(a)

(b)

(c)
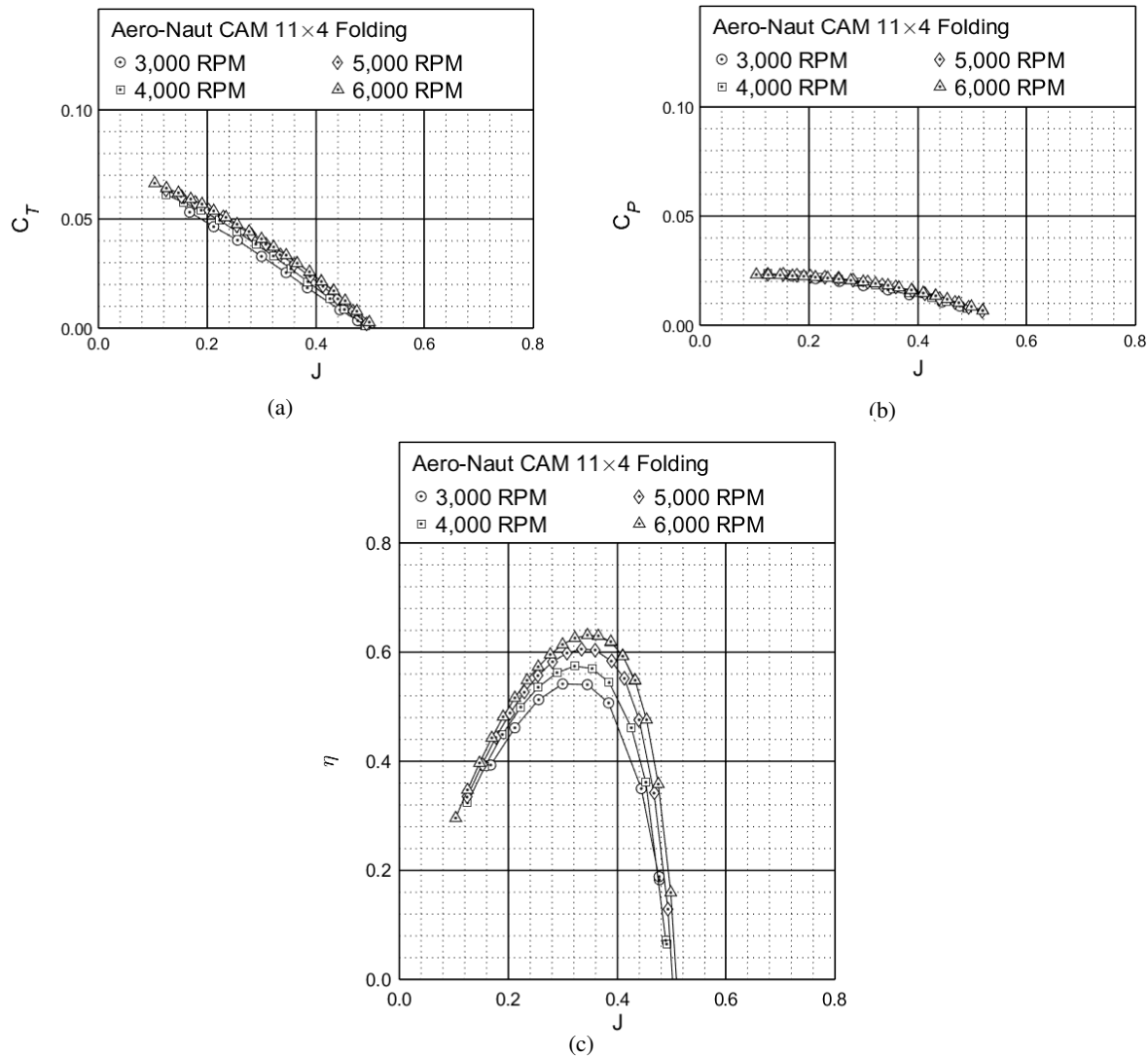
Figure 25: Performance of the Aero-Naut CAM 11×4 folding propeller: (a) thrust coefficient, (b) power coefficient, (c) efficiency.

American Institute of Aeronautics and Astronautics
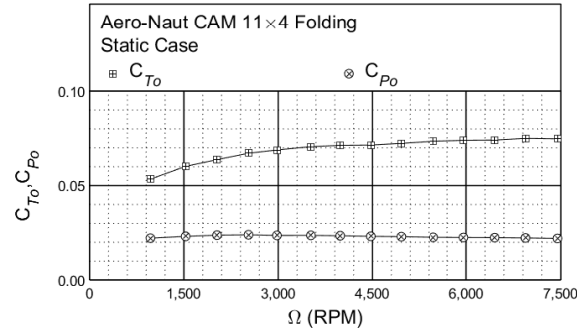
Figure 26: Static performance of the Aero-Naut CAM 11×4 folding propeller: thrust and power coefficient.

**Aero-Naut CAM 11×6 Folding Propeller**

(a)

(b)

(c)
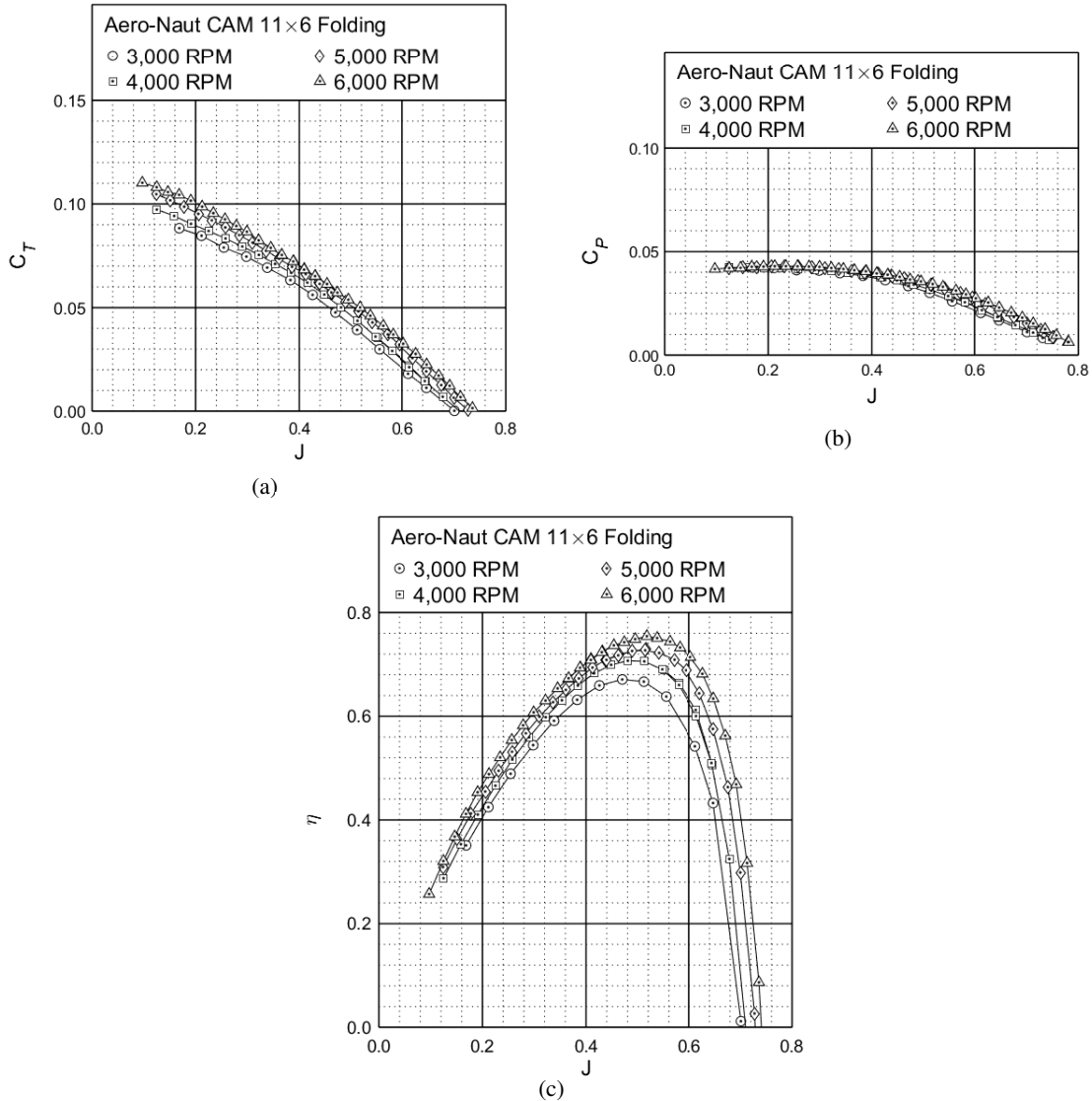
Figure 27: Performance of the Aero-Naut CAM 11×6 folding propeller: (a) thrust coefficient, (b) power coefficient, (c) efficiency.
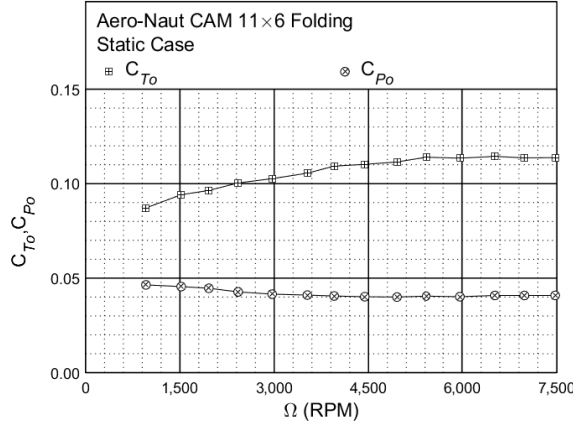
Figure 28: Static performance of the Aero-Naut CAM 11×6 folding propeller: thrust and power coefficient.

Aero-Naut CAM 11×7 Folding Propeller

(a)

(b)

(c)
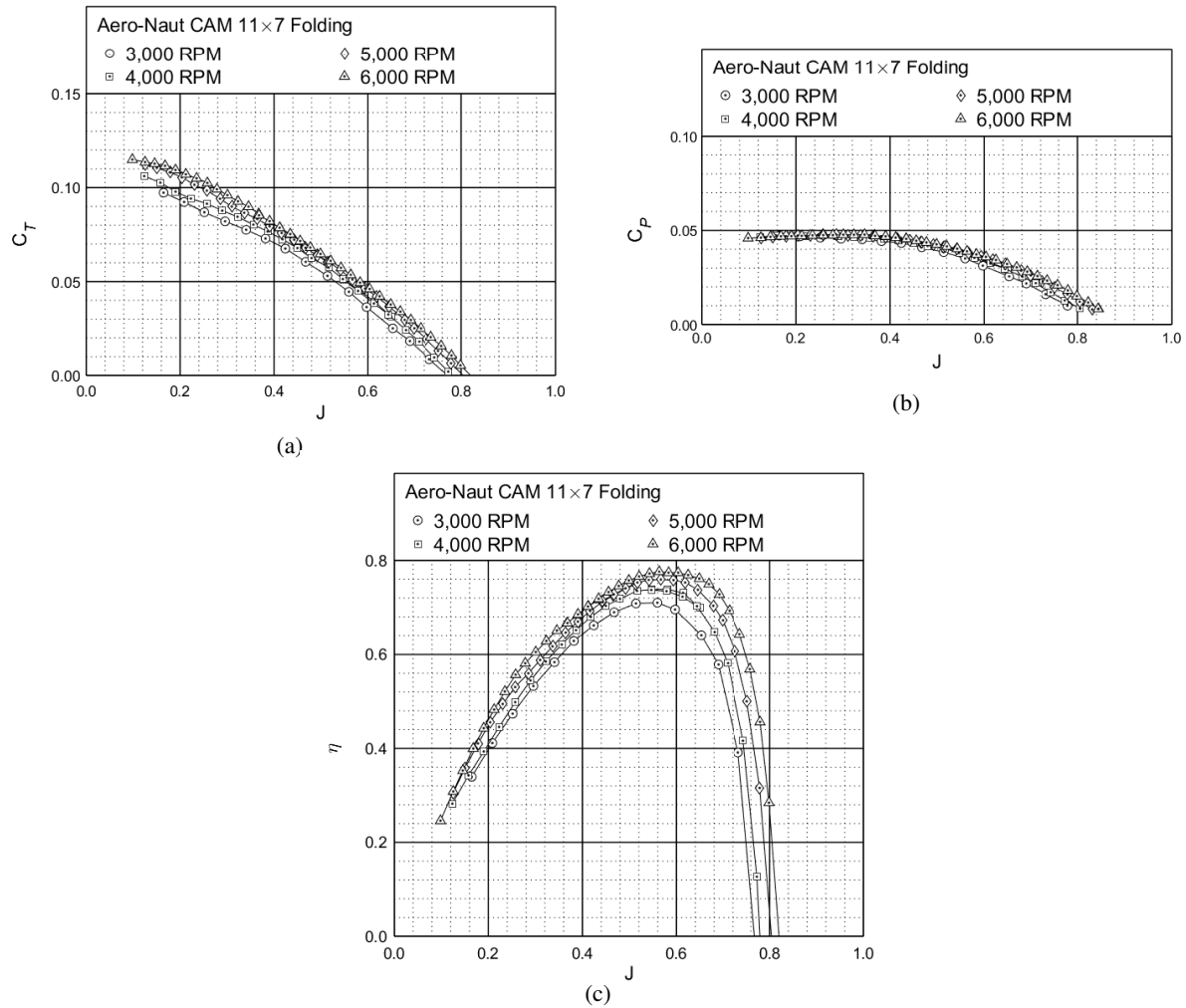
Figure 29: Performance of the Aero-Naut CAM 11×7 folding propeller: (a) thrust coefficient, (b) power coefficient, (c) efficiency.
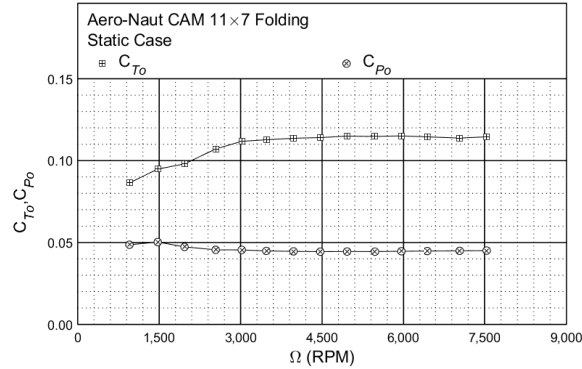
Figure 30: Static performance of the Aero-Naut CAM 11×7 folding propeller: thrust and power coefficient.

**Aero-Naut CAM 11×8 Folding Propeller**

(a)

(b)

(c)
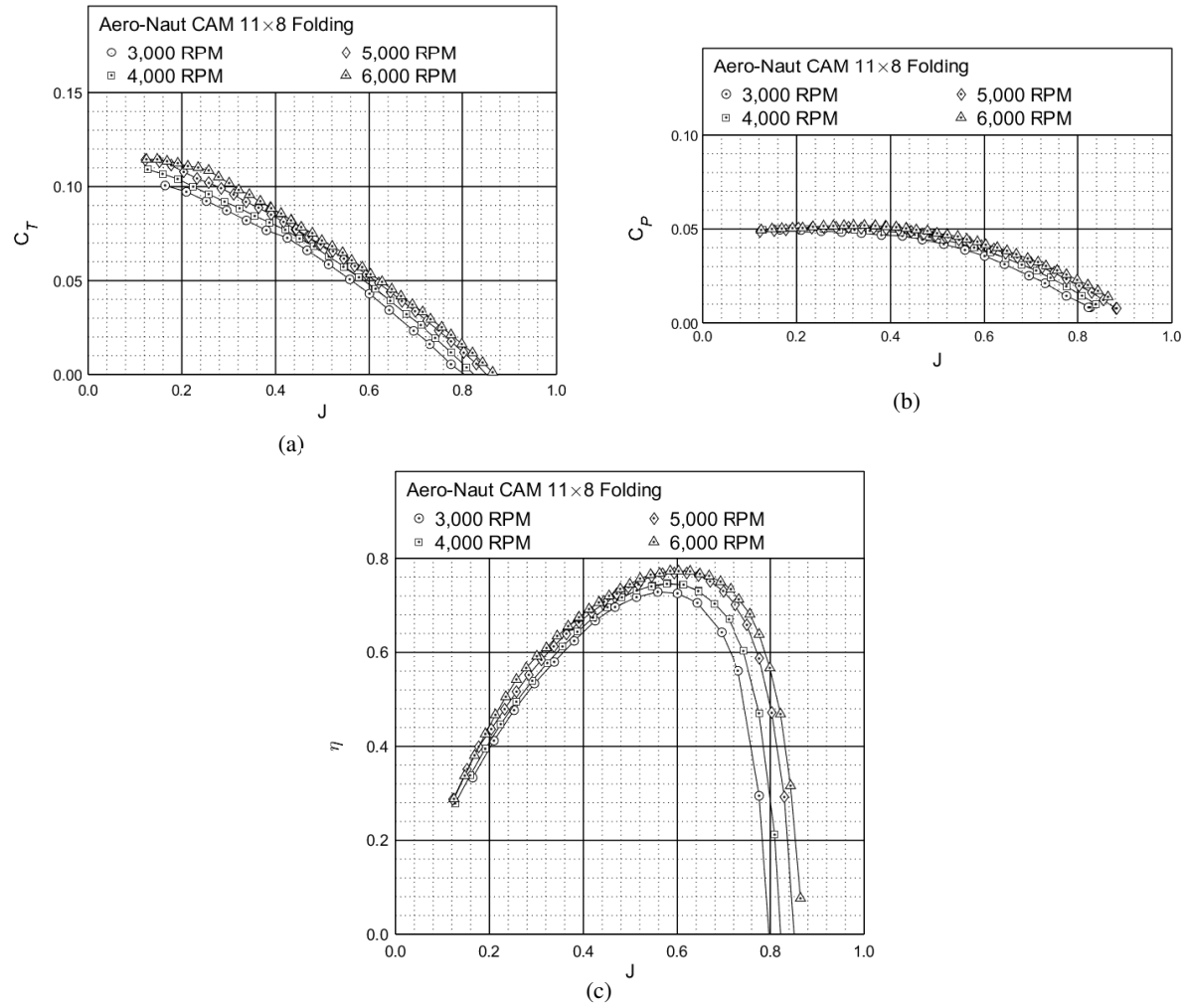
Figure 31: Performance of the Aero-Naut CAM 11×8 folding propeller: (a) thrust coefficient, (b) power coefficient, (c) efficiency.
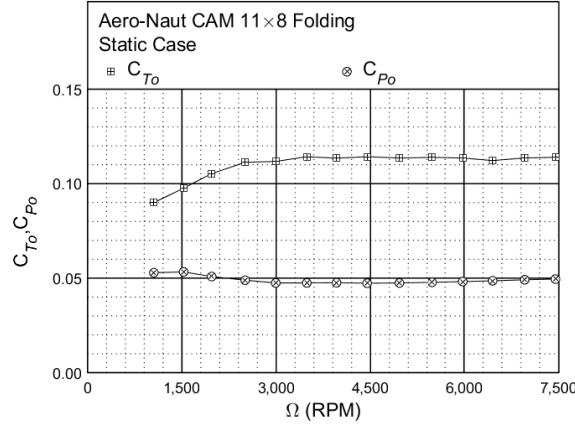
Figure 32: Static performance of the Aero-Naut CAM 11×8 folding propeller: thrust and power coefficient.

Aero-Naut CAM 11×10 Folding Propeller

(a)

(b)

(c)
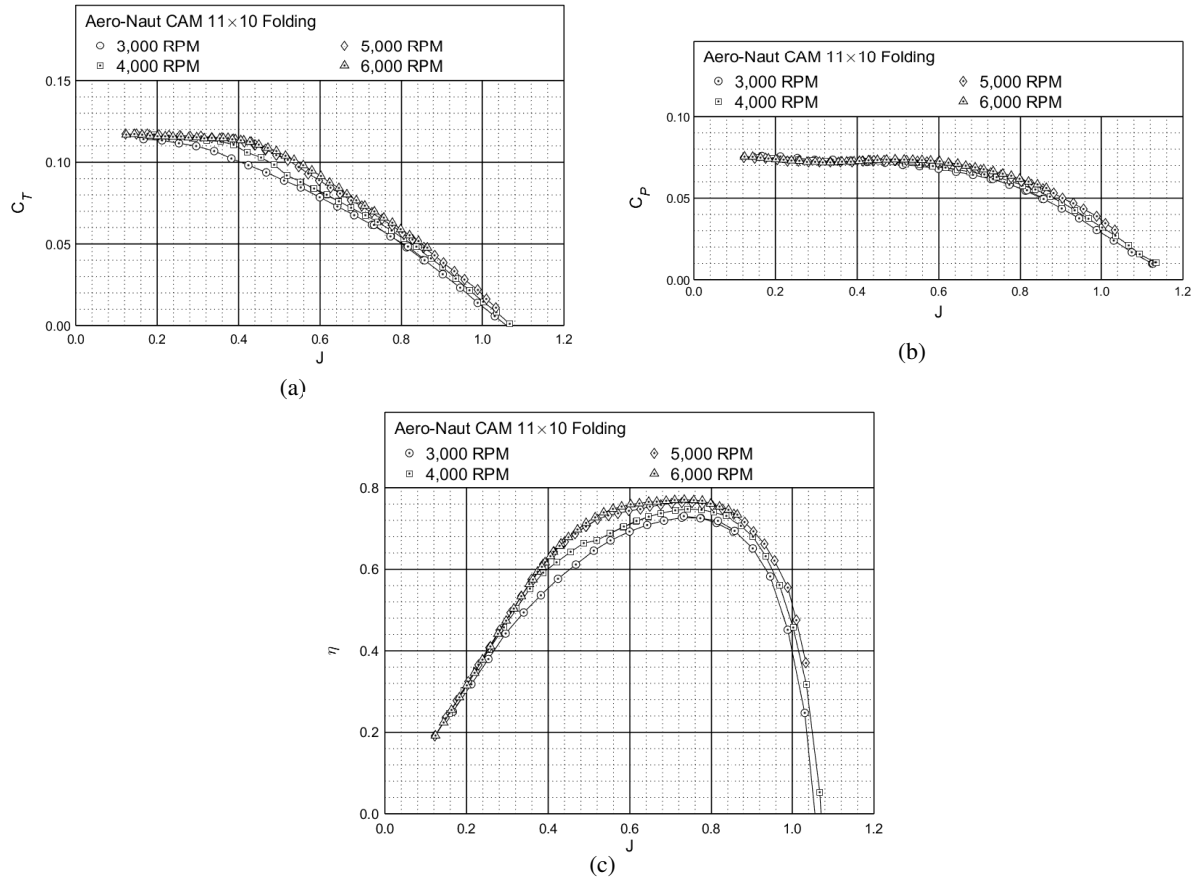
Figure 33: Performance of the Aero-Naut CAM 11×10 folding propeller: (a) thrust coefficient, (b) power coefficient, (c) efficiency.

American Institute of Aeronautics and Astronautics
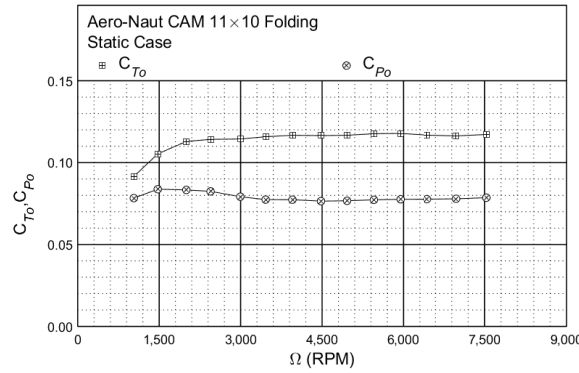
Figure 34: Static performance of the Aero-Naut CAM 11×10 folding propeller: thrust and power coefficient.

Aero-Naut CAM 11×12 Folding Propeller


(a)

(b)

(c)
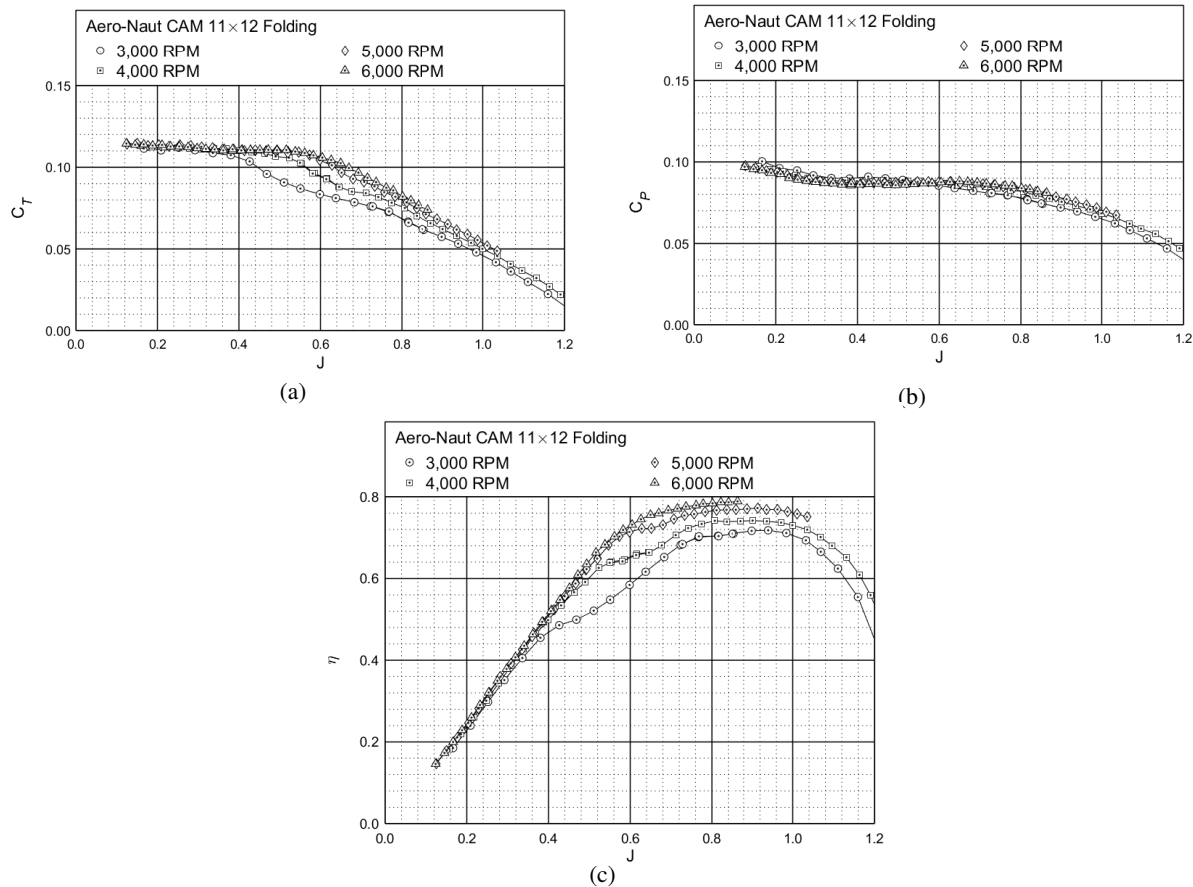
Figure 35: Performance of the Aero-Naut CAM 11×12 folding propeller: (a) thrust coefficient, (b) power coefficient, (c) efficiency.

American Institute of Aeronautics and Astronautics
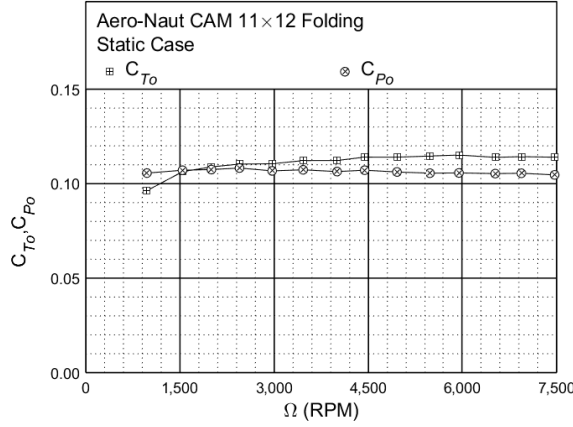
Figure 36: Static performance of the Aero-Naut CAM 11×12 folding propeller: thrust and power coefficient.

**Aero-Naut CAM 12×5 Folding Propeller**

(a)

(b)

(c)
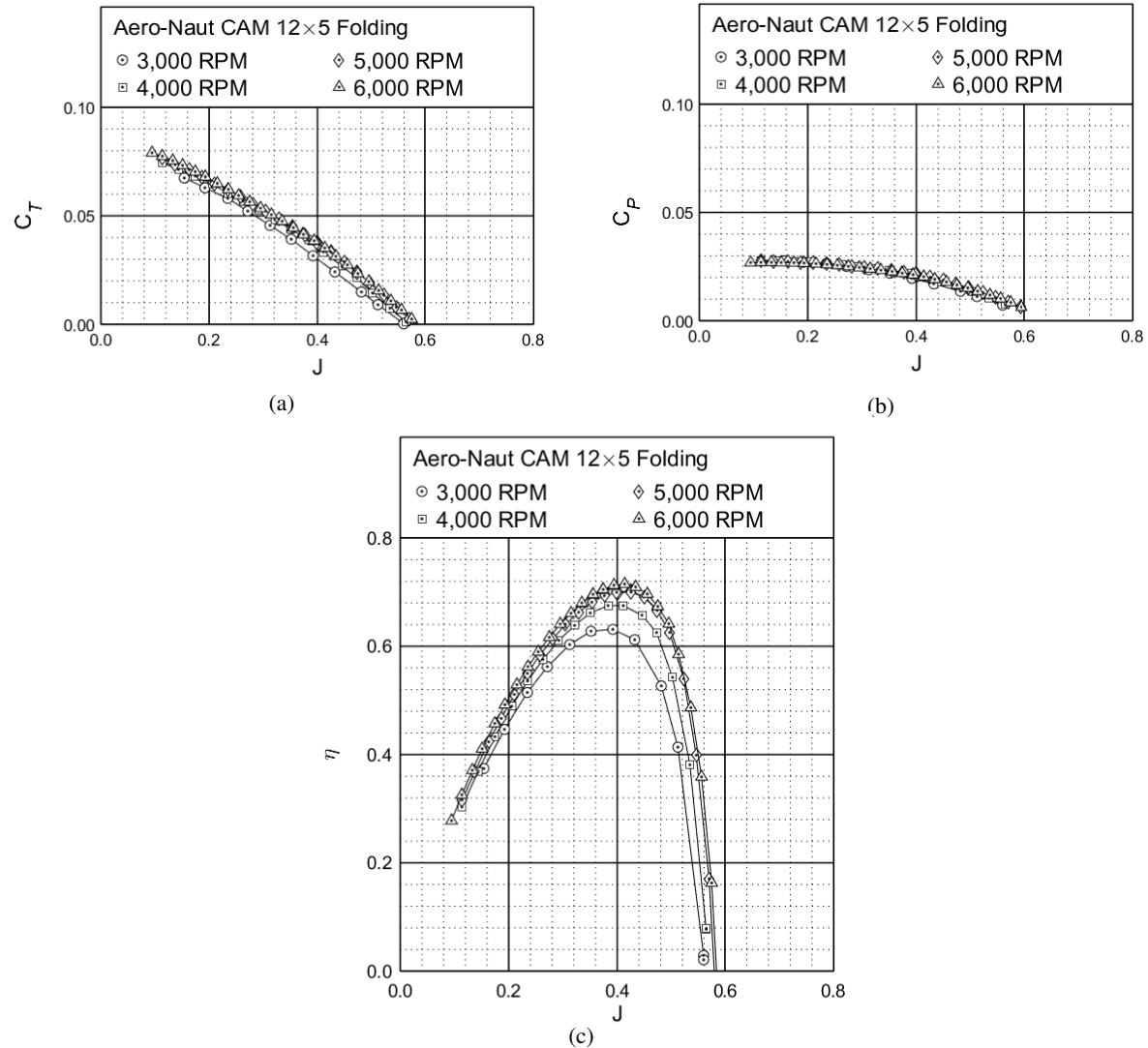
Figure 37: Performance of the Aero-Naut CAM 12×5 folding propeller: (a) thrust coefficient, (b) power coefficient, (c) efficiency.
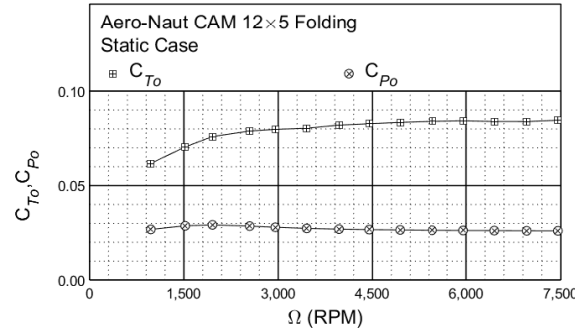
Figure 38: Static performance of the Aero-Naut CAM 12×5 folding propeller: thrust and power coefficient.

**Aero-Naut CAM 12×6 Folding Propeller**

(a)

(b)

(c)
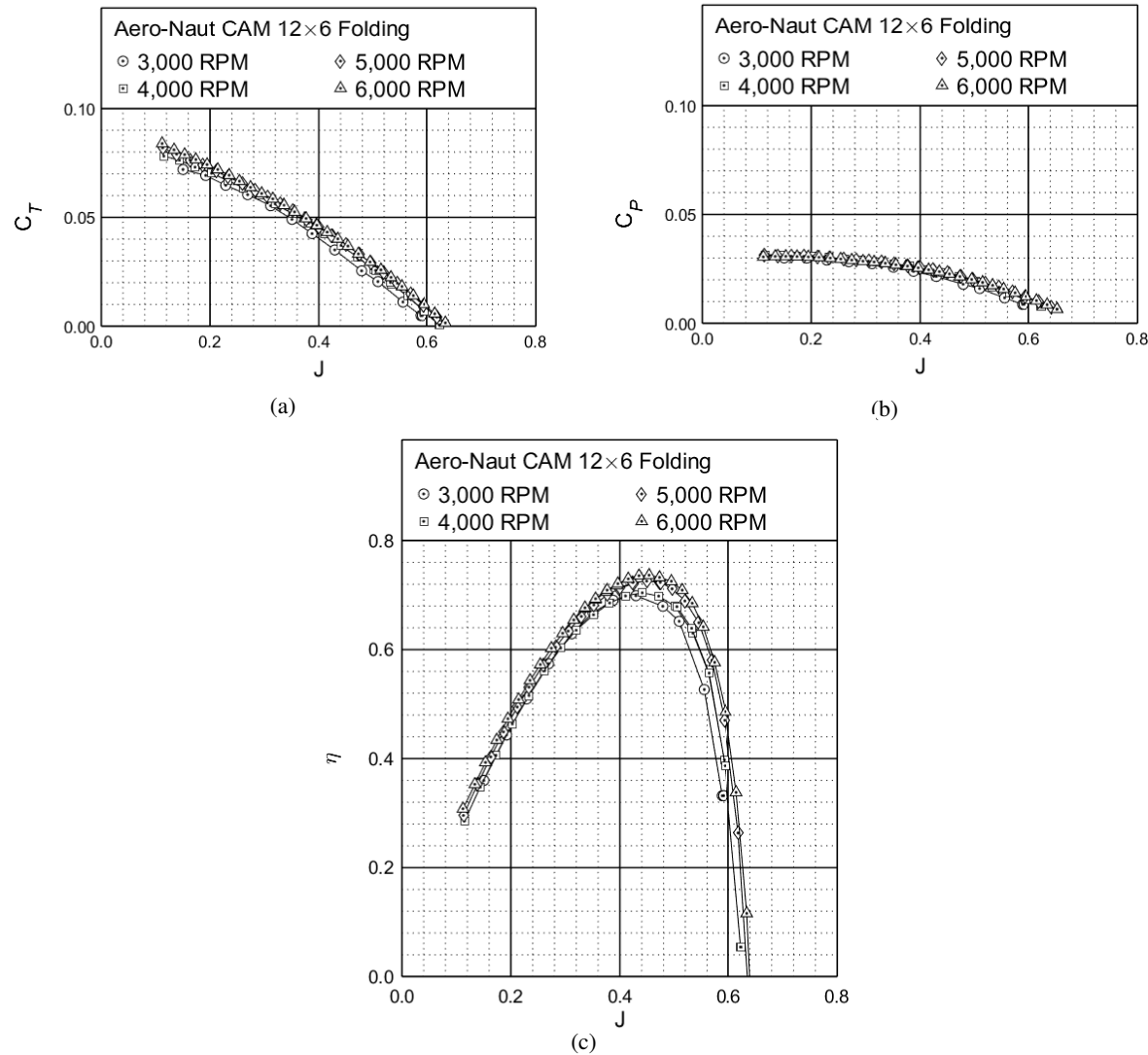
Figure 39: Performance of the Aero-Naut CAM 12×6 folding propeller: (a) thrust coefficient, (b) power coefficient, (c) efficiency.
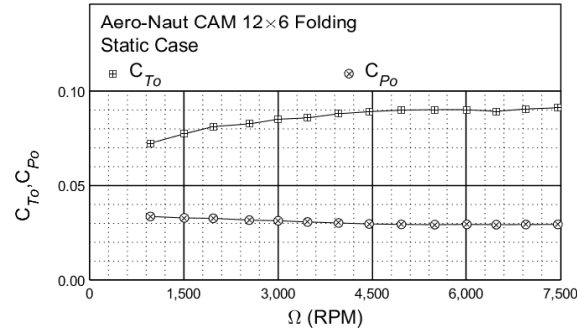
Figure 40: Static performance of the Aero-Naut CAM 12×6 folding propeller: thrust and power coefficient.

Aero-Naut CAM 12×6.5 Folding Propeller

(a)

(b)

(c)
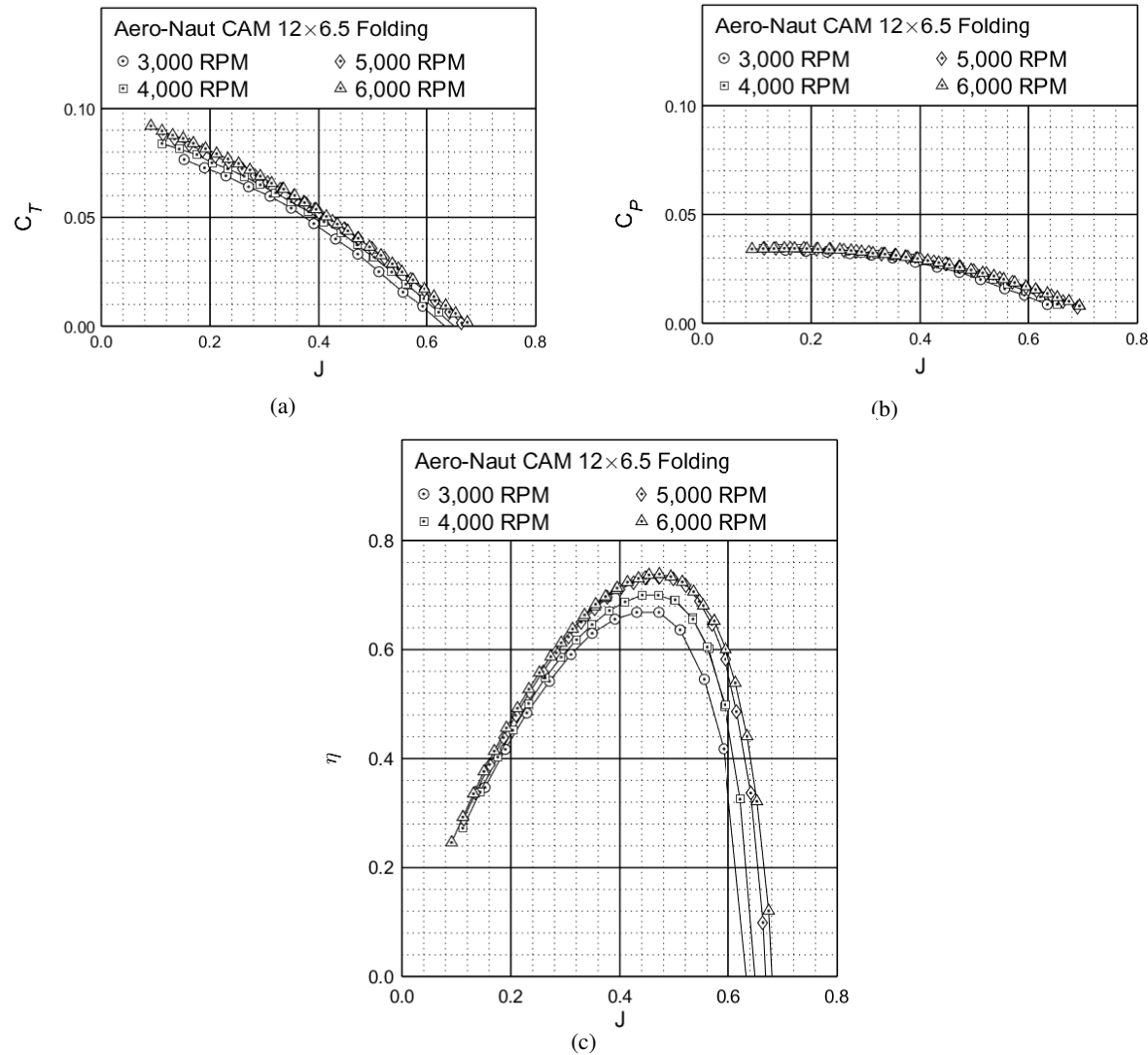
Figure 41: Performance of the Aero-Naut CAM 12×6.5 folding propeller: (a) thrust coefficient, (b) power coefficient, (c) efficiency.
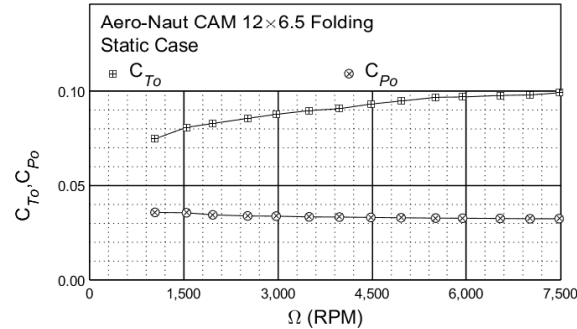
Figure 42: Static performance of the Aero-Naut CAM 12×6.5 folding propeller: thrust and power coefficient.

**Aero-Naut CAM 12×8 Folding Propeller**

(a)

(b)

(c)
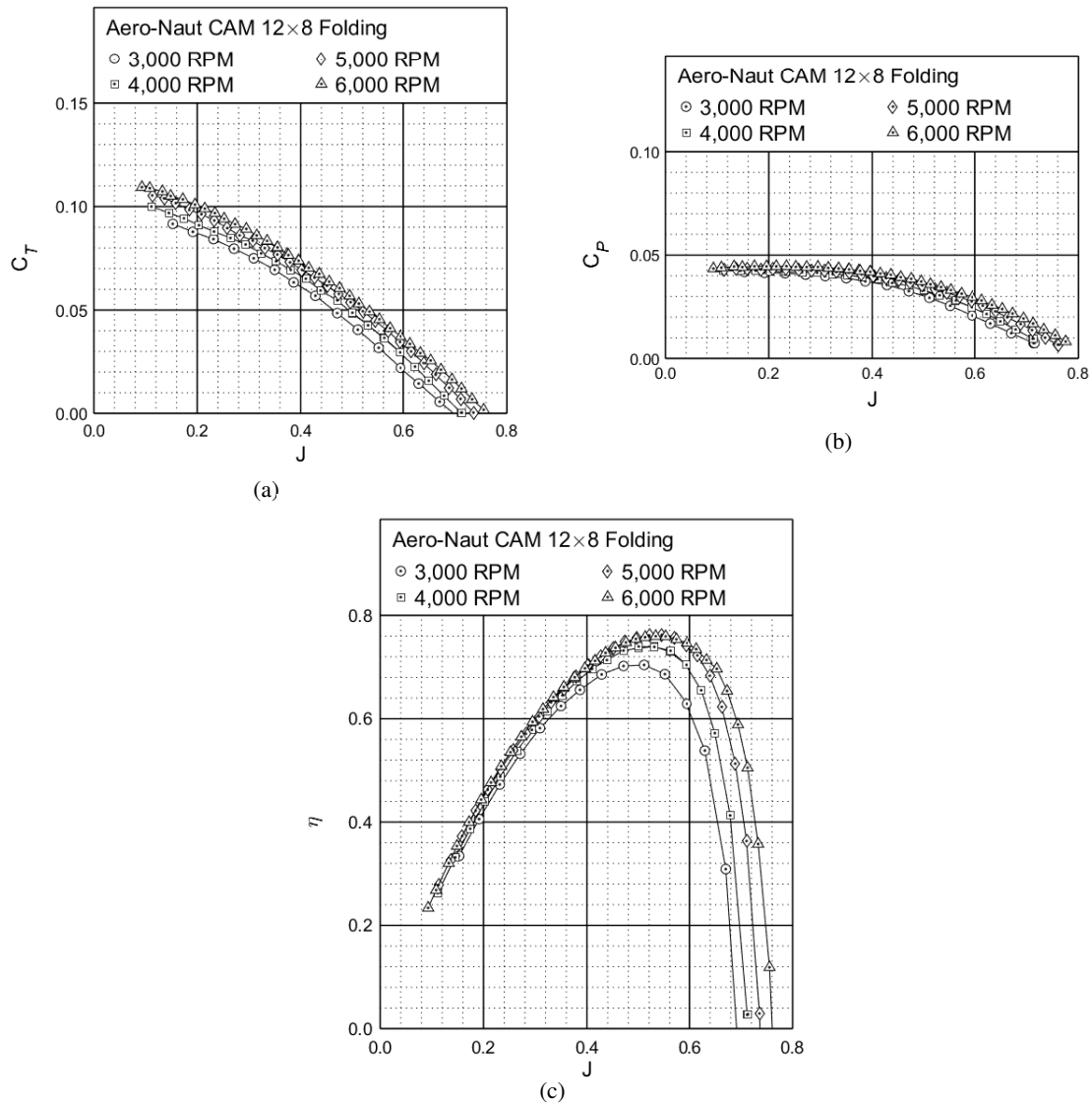
Figure 43: Performance of the Aero-Naut CAM 12×8 folding propeller: (a) thrust coefficient, (b) power coefficient, (c) efficiency.
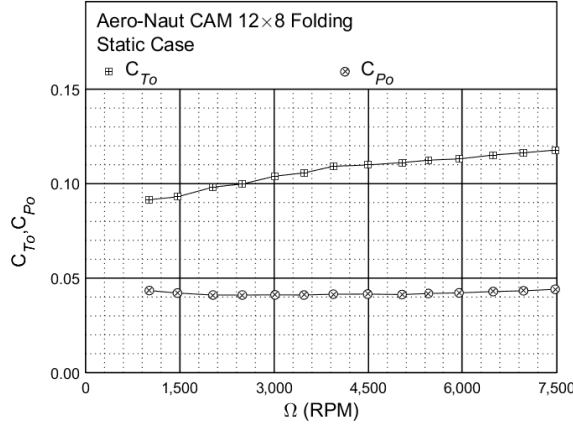
Figure 44: Static performance of the Aero-Naut CAM 12×8 folding propeller: thrust and power coefficient.

Aero-Naut CAM 12×9 Folding Propeller

(a)

(b)

(c)
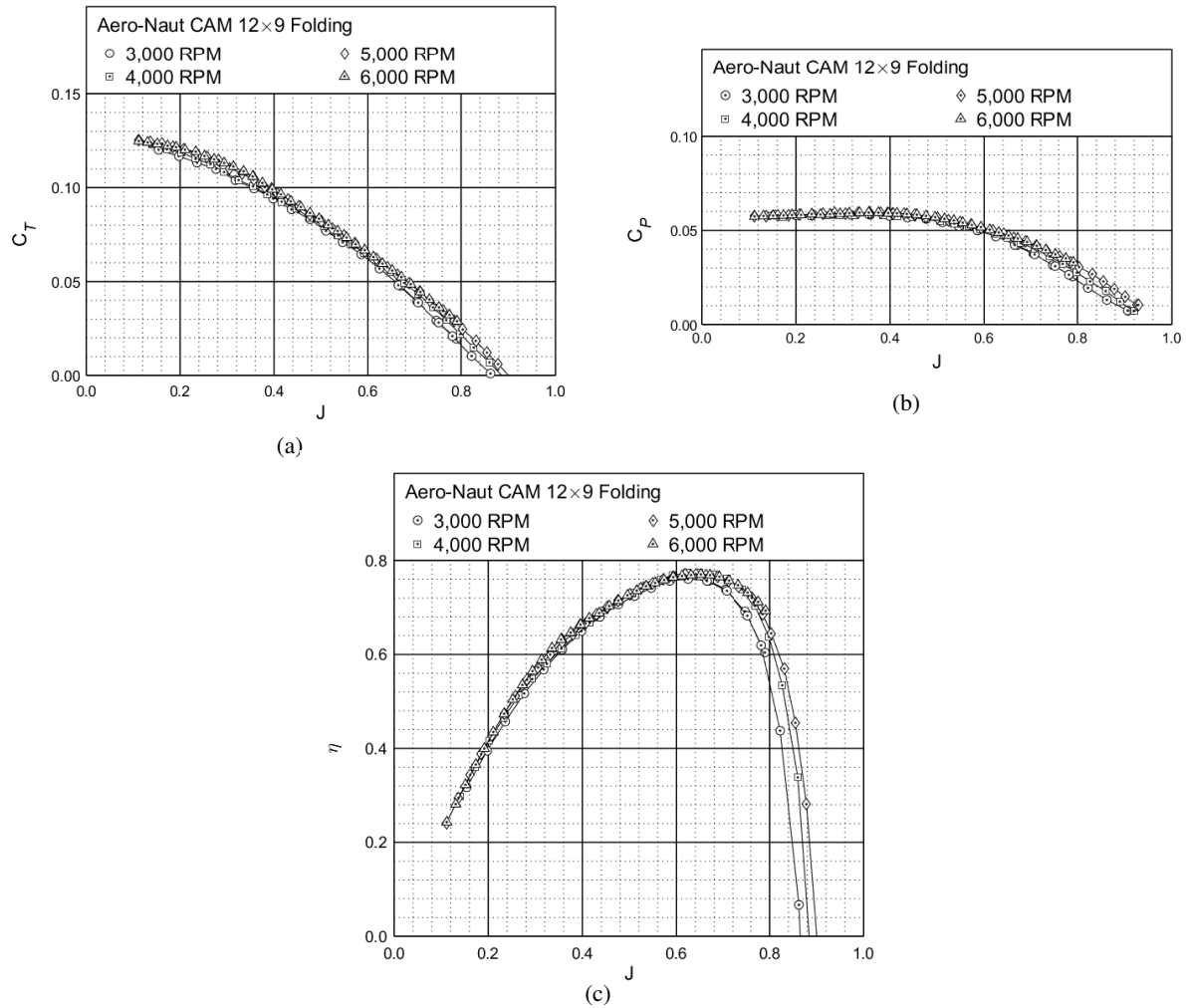
Figure 45: Performance of the Aero-Naut CAM 12×9 folding propeller: (a) thrust coefficient, (b) power coefficient, (c) efficiency.
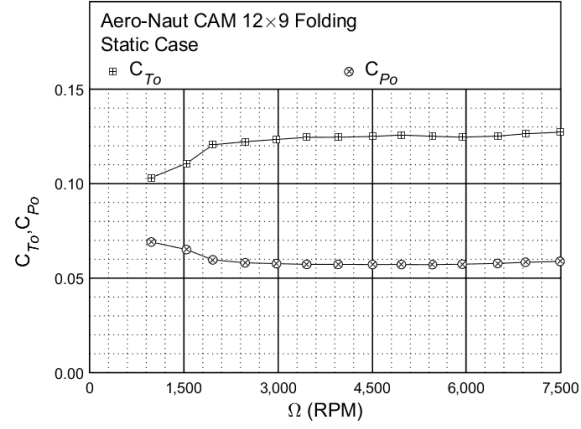
Figure 46: Static performance of the Aero-Naut CAM 12×9 folding propeller: thrust and power coefficient.

Aero-Naut CAM 12×10 Folding Propeller

(a)

(b)

(c)
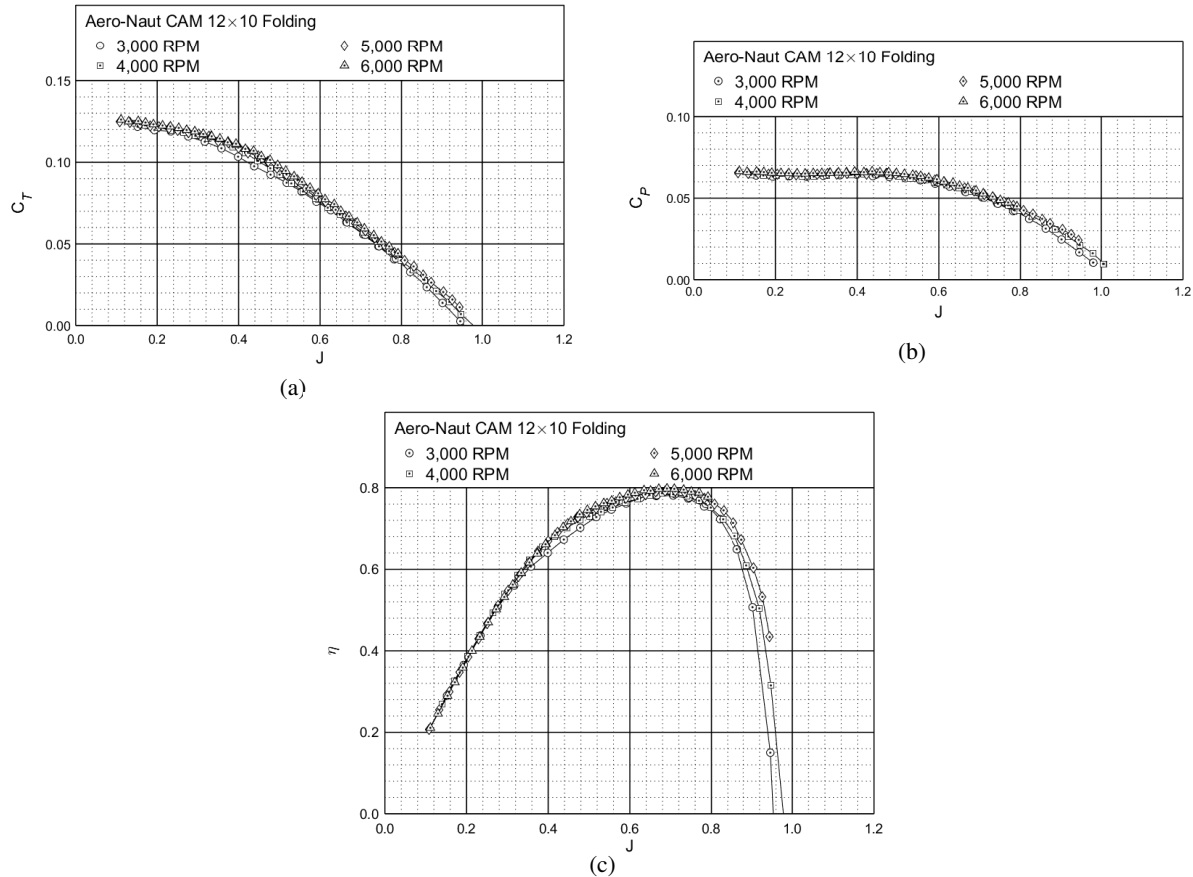
Figure 47: Performance of the Aero-Naut CAM 12×10 folding propeller: (a) thrust coefficient, (b) power coefficient, (c) efficiency.
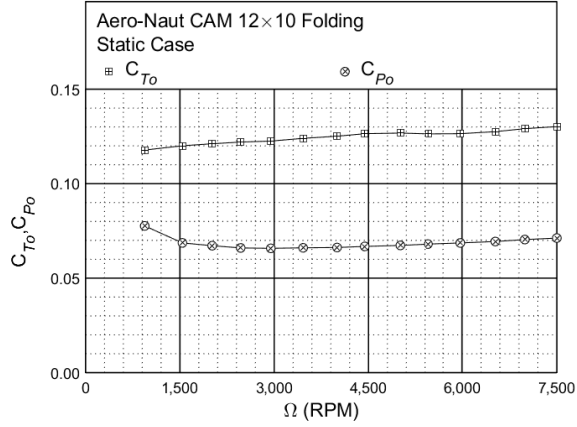
Figure 48: Static performance of the Aero-Naut CAM 12×10 folding propeller: thrust and power coefficient.

Aero-Naut CAM 12×11 Folding Propeller

(a)

(b)

(c)
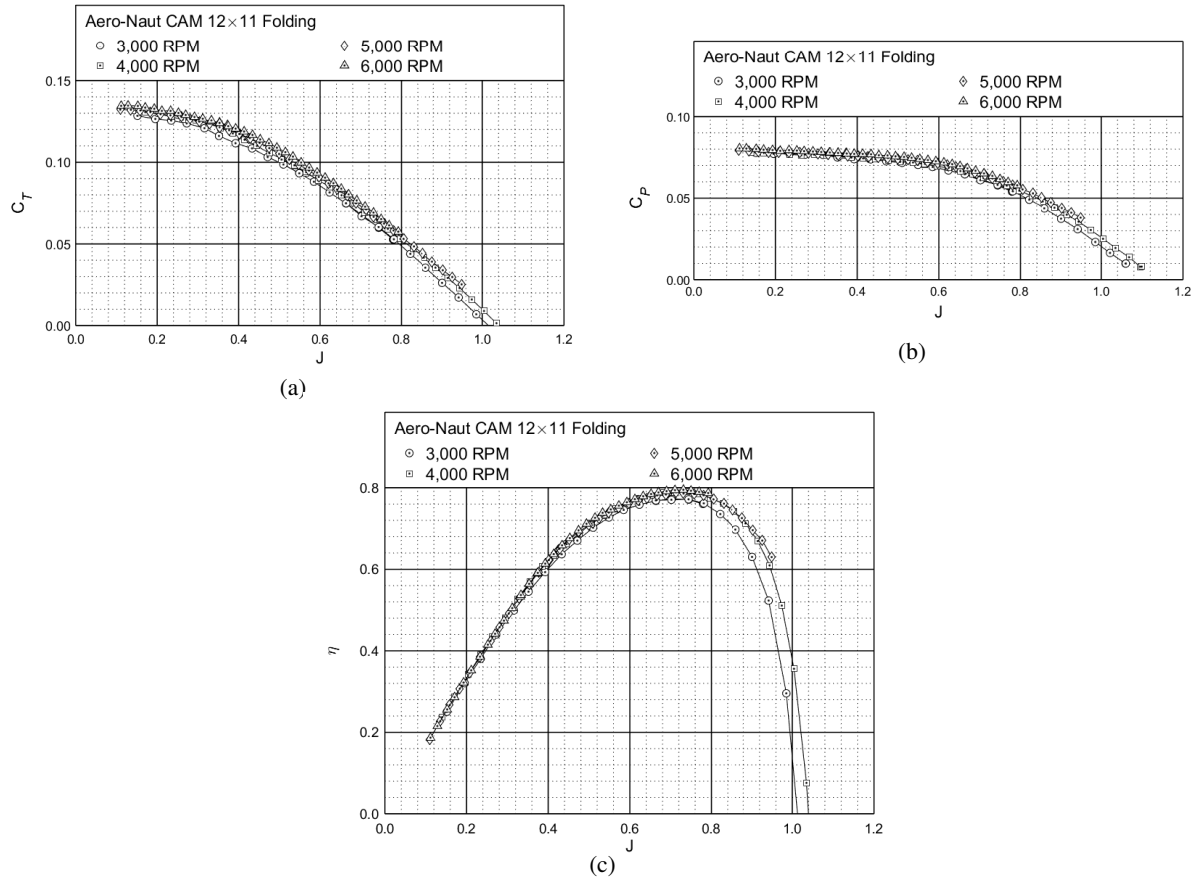
Figure 49: Performance of the Aero-Naut CAM 12×11 folding propeller: (a) thrust coefficient, (b) power coefficient, (c) efficiency.
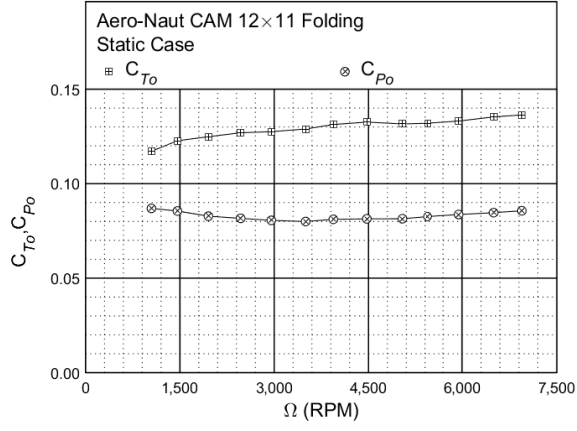
Figure 50: Static performance of the Aero-Naut CAM 12×11 folding propeller: thrust and power coefficient.

Aero-Naut CAM 12×13 Folding Propeller

(a)

(b)

(c)
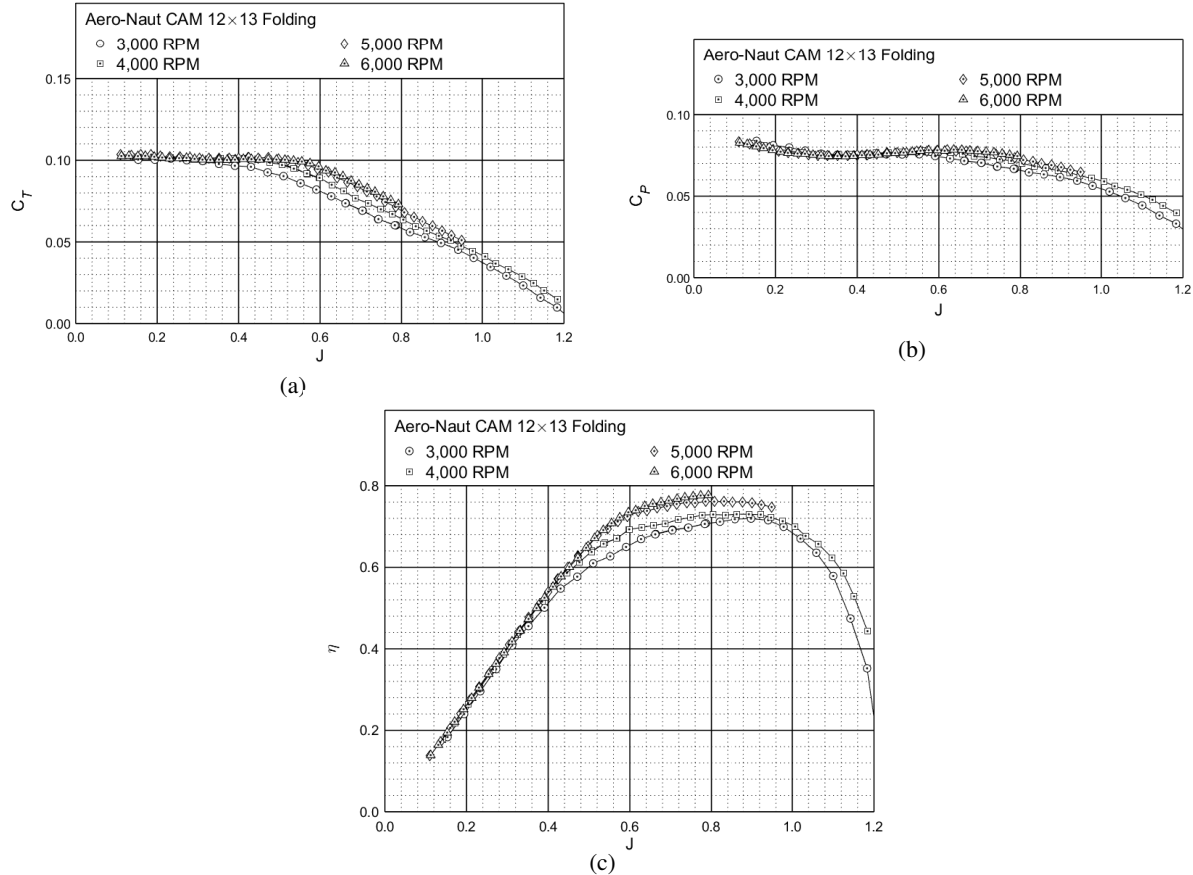
Figure 51: Performance of the Aero-Naut CAM 12×13 folding propeller: (a) thrust coefficient, (b) power coefficient, (c) efficiency.

American Institute of Aeronautics and Astronautics
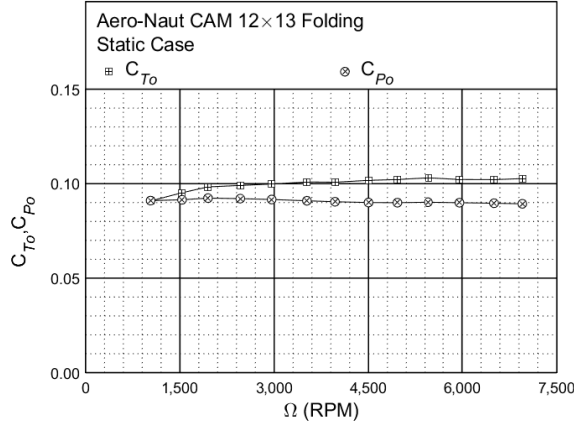
Figure 52: Static performance of the Aero-Naut CAM 12×13 folding propeller: thrust and power coefficient.

Aero-Naut CAM 12.5×6 Folding Propeller

(a)

(b)

(c)
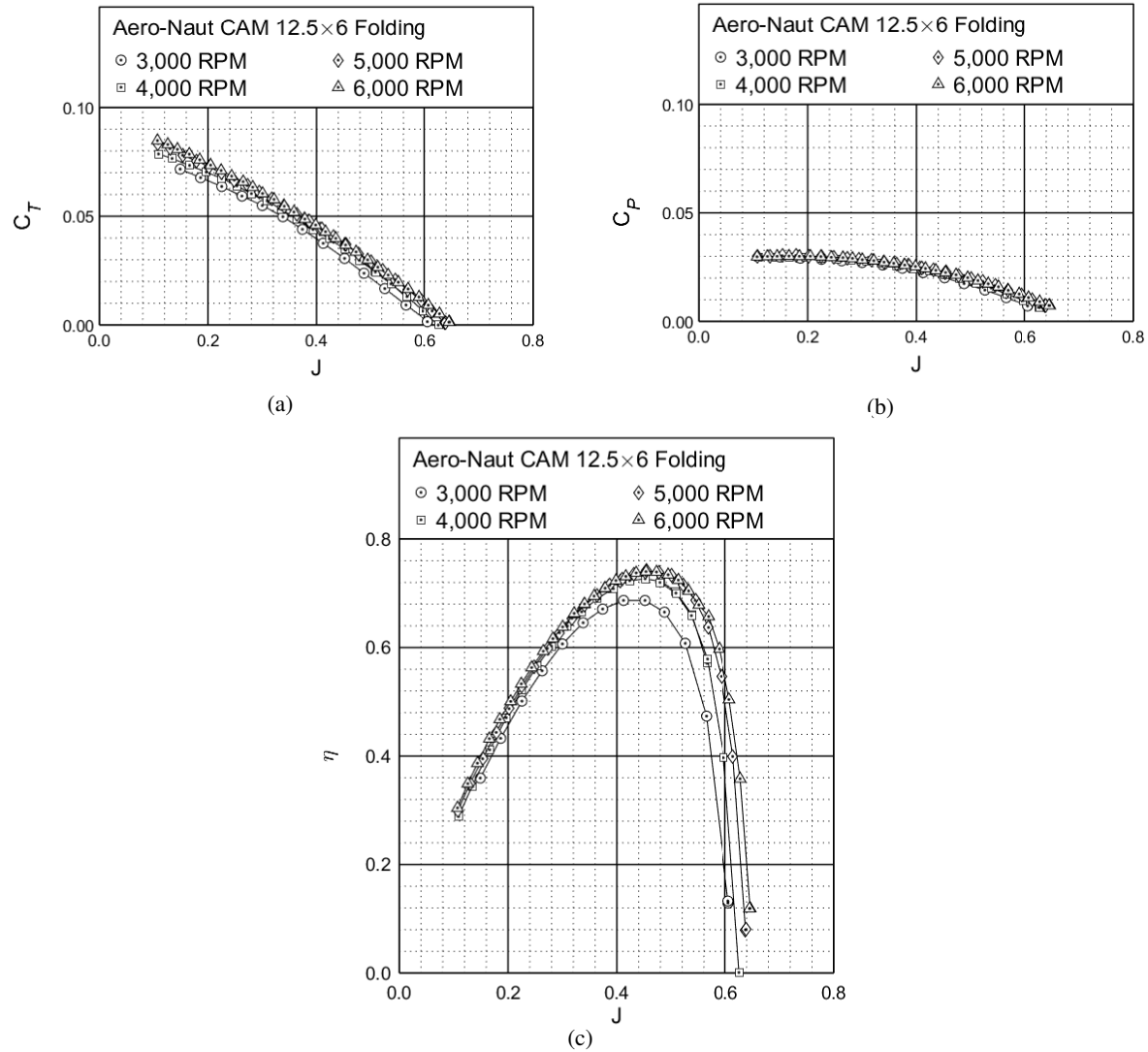
Figure 53: Performance of the Aero-Naut CAM 12.5×6 folding propeller: (a) thrust coefficient, (b) power coefficient, (c) efficiency.

American Institute of Aeronautics and Astronautics
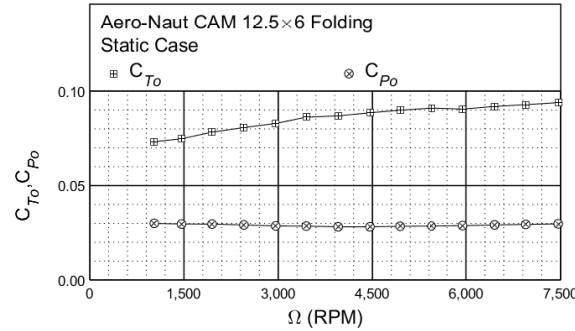
Figure 54: Static performance of the Aero-Naut CAM 12.5×6 folding propeller: thrust and power coefficient.

Aero-Naut CAM 12.5×7.5 Folding Propeller

(a)

(b)

(c)
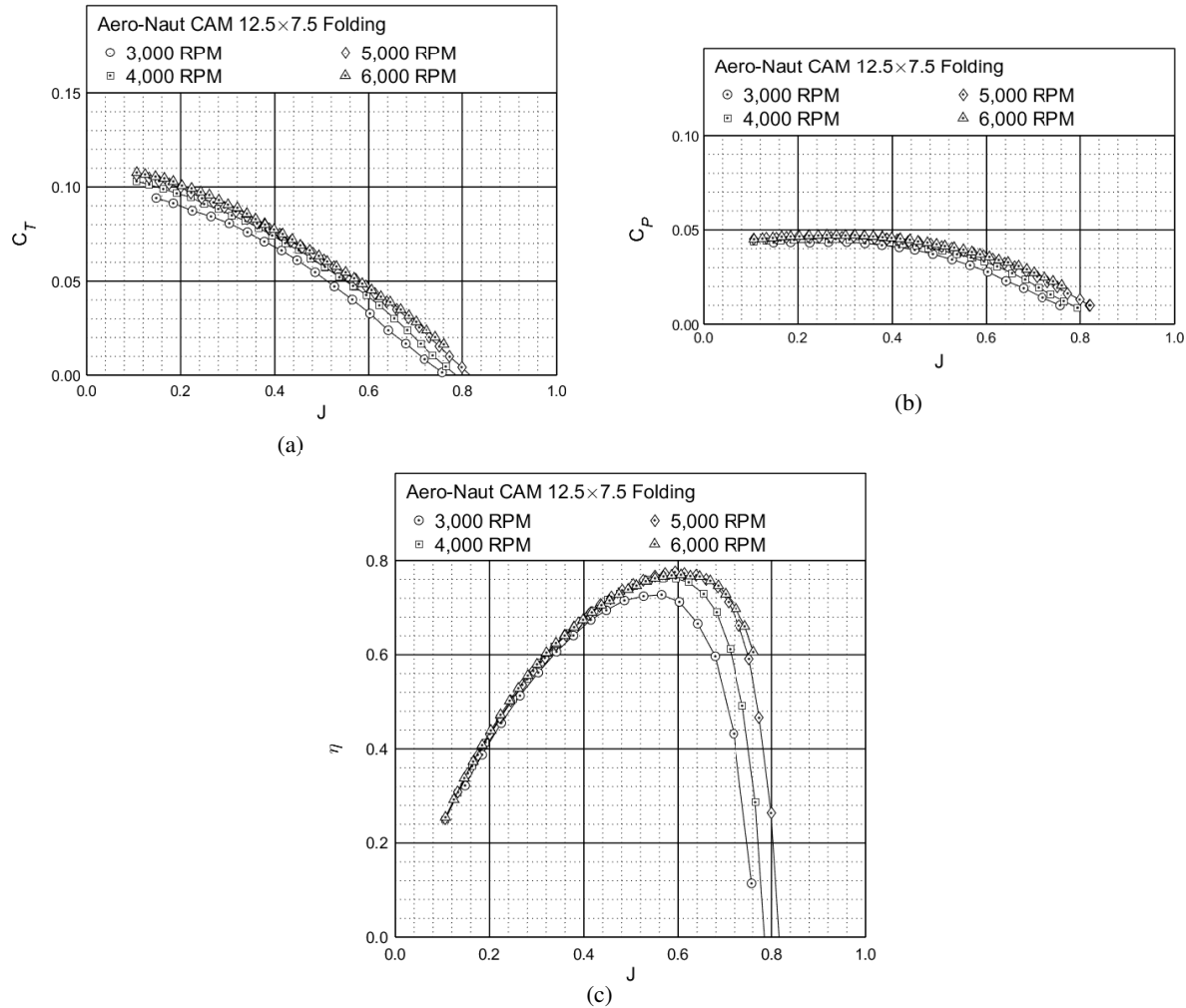
Figure 55: Performance of the Aero-Naut CAM 12.5×7.5 folding propeller: (a) thrust coefficient, (b) power coefficient, (c) efficiency.

American Institute of Aeronautics and Astronautics
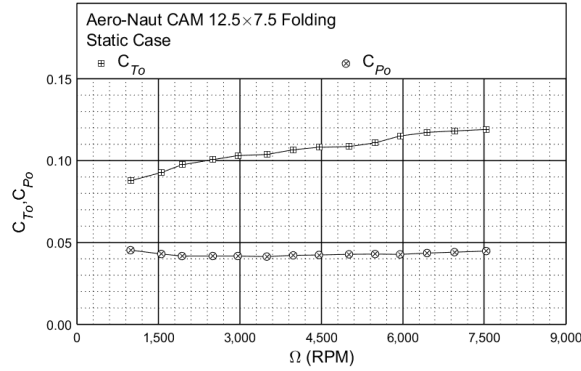
Figure 56: Static performance of the Aero-Naut CAM 12.5×7.5 folding propeller: thrust and power coefficient.

Aero-Naut CAM 12.5×9 Folding Propeller


(a)

(b)

(c)
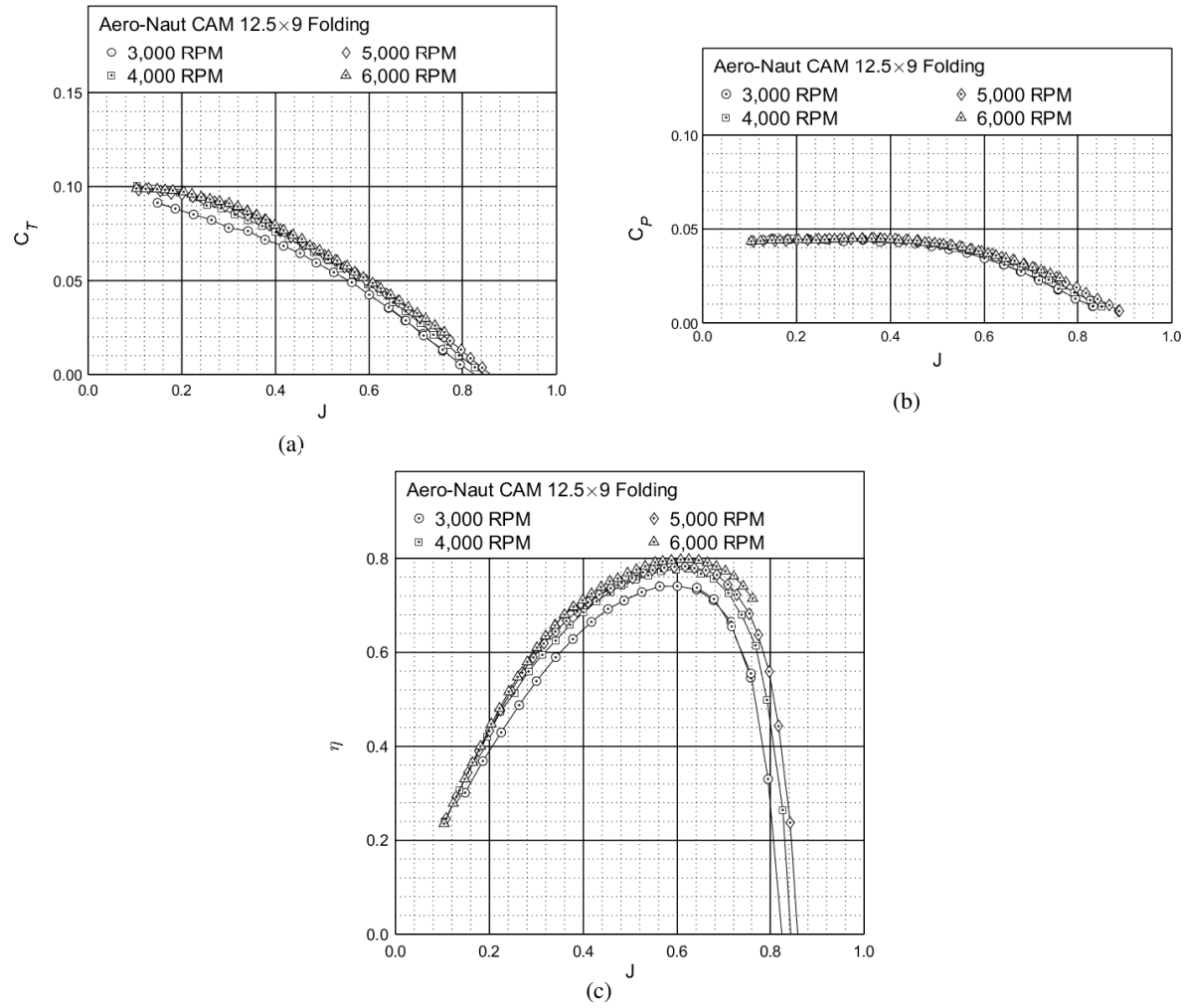
Figure 57: Performance of the Aero-Naut CAM 12.5×9 folding propeller: (a) thrust coefficient, (b) power coefficient, (c) efficiency.
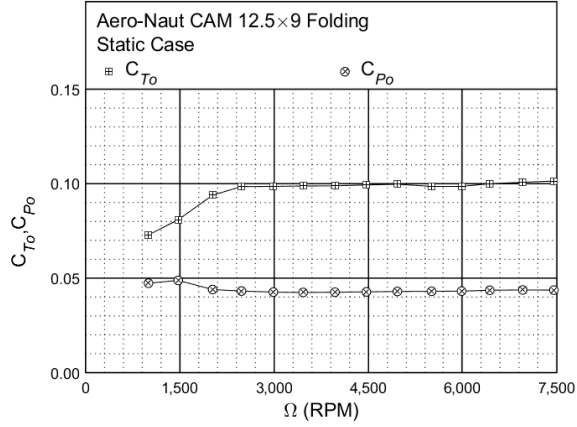
Figure 58: Static performance of the Aero-Naut CAM 12.5×9 folding propeller: thrust and power coefficient.

Aero-Naut CAM 13×5 Folding Propeller


(a)

(b)

(c)
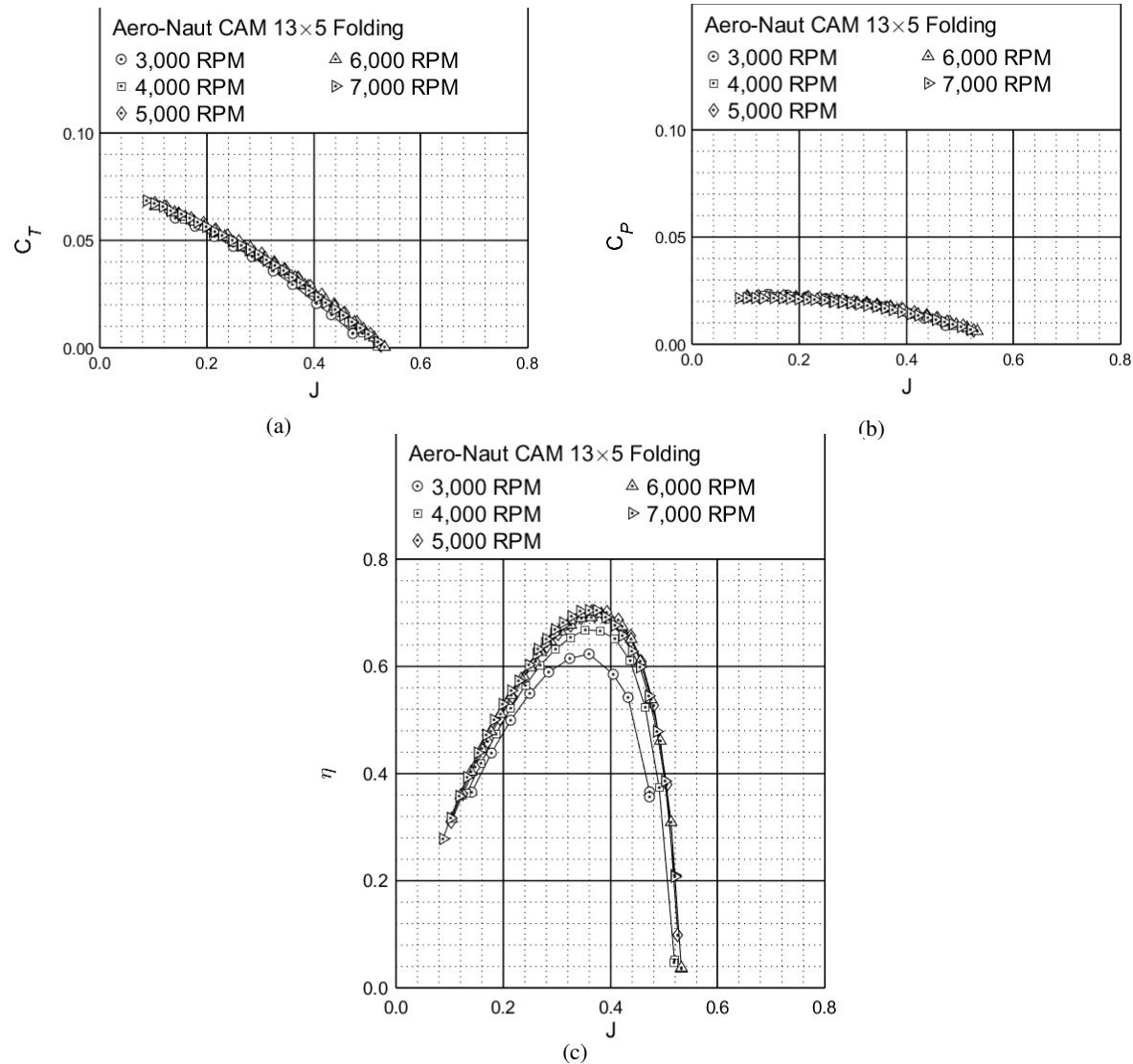
Figure 59: Performance of the Aero-Naut CAM 13×5 folding propeller: (a) thrust coefficient, (b) power coefficient, (c) efficiency.
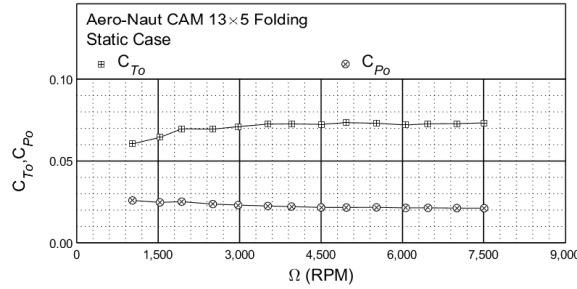
Figure 60: Static performance of the Aero-Naut CAM 13×5 folding propeller: thrust and power coefficient.

Aero-Naut CAM 13×6.5 Folding Propeller

(a)

(b)

(c)
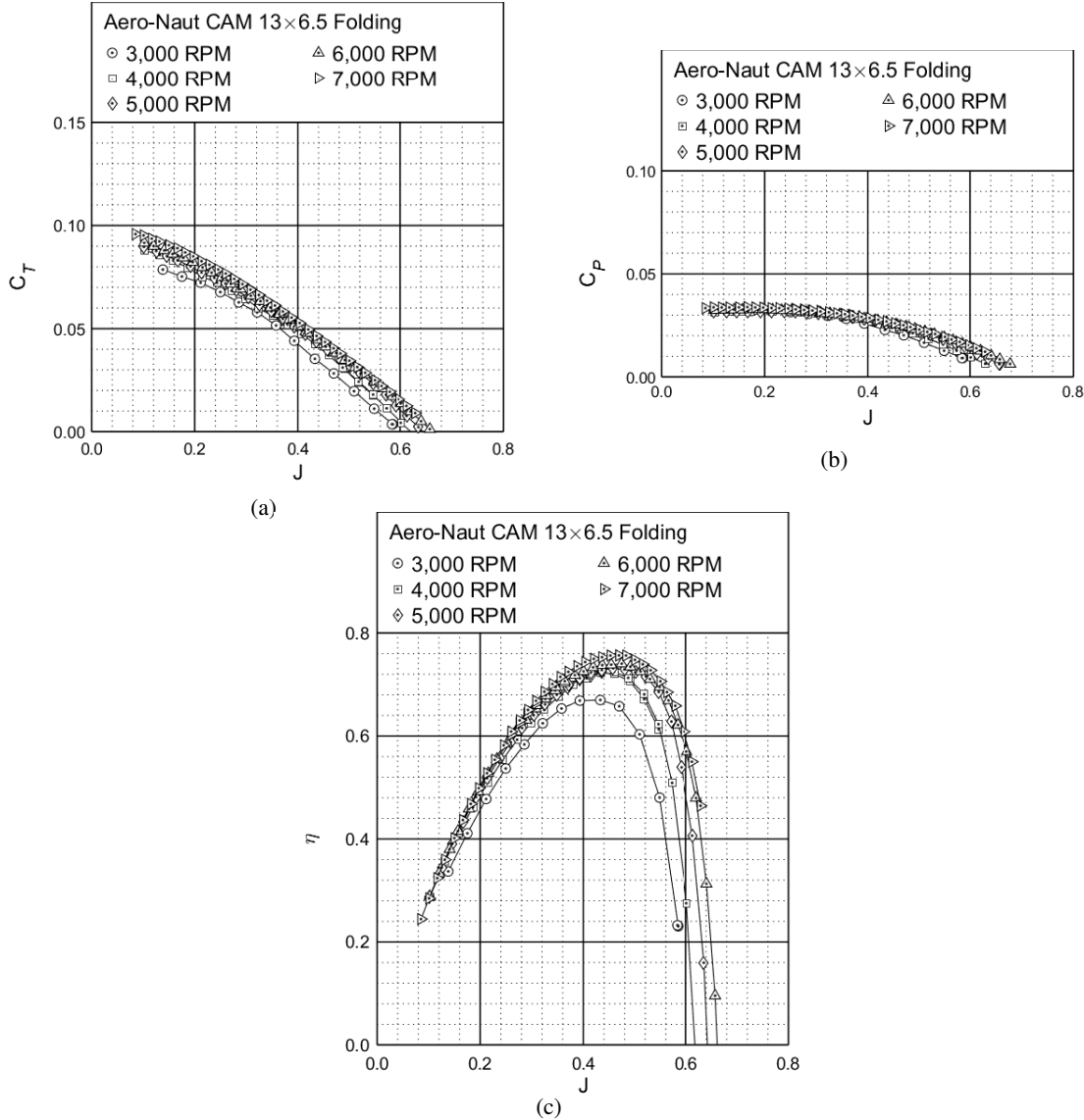
Figure 61: Performance of the Aero-Naut CAM 13×6.5 folding propeller: (a) thrust coefficient, (b) power coefficient, (c) efficiency.

American Institute of Aeronautics and Astronautics
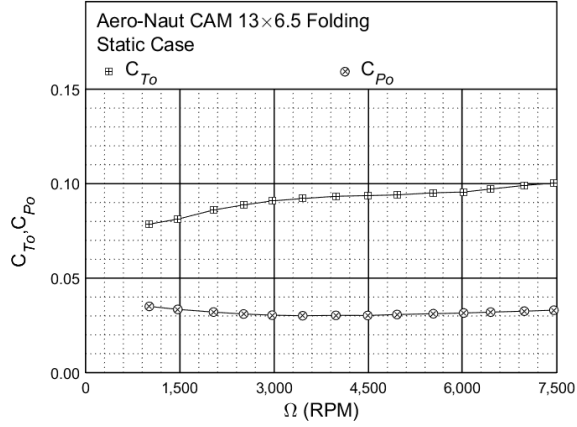
Figure 62: Static performance of the Aero-Naut CAM 13×6.5 folding propeller: thrust and power coefficient.

## Aero-Naut CAM 13×8 Folding Propeller

(a)

(b)

(c)
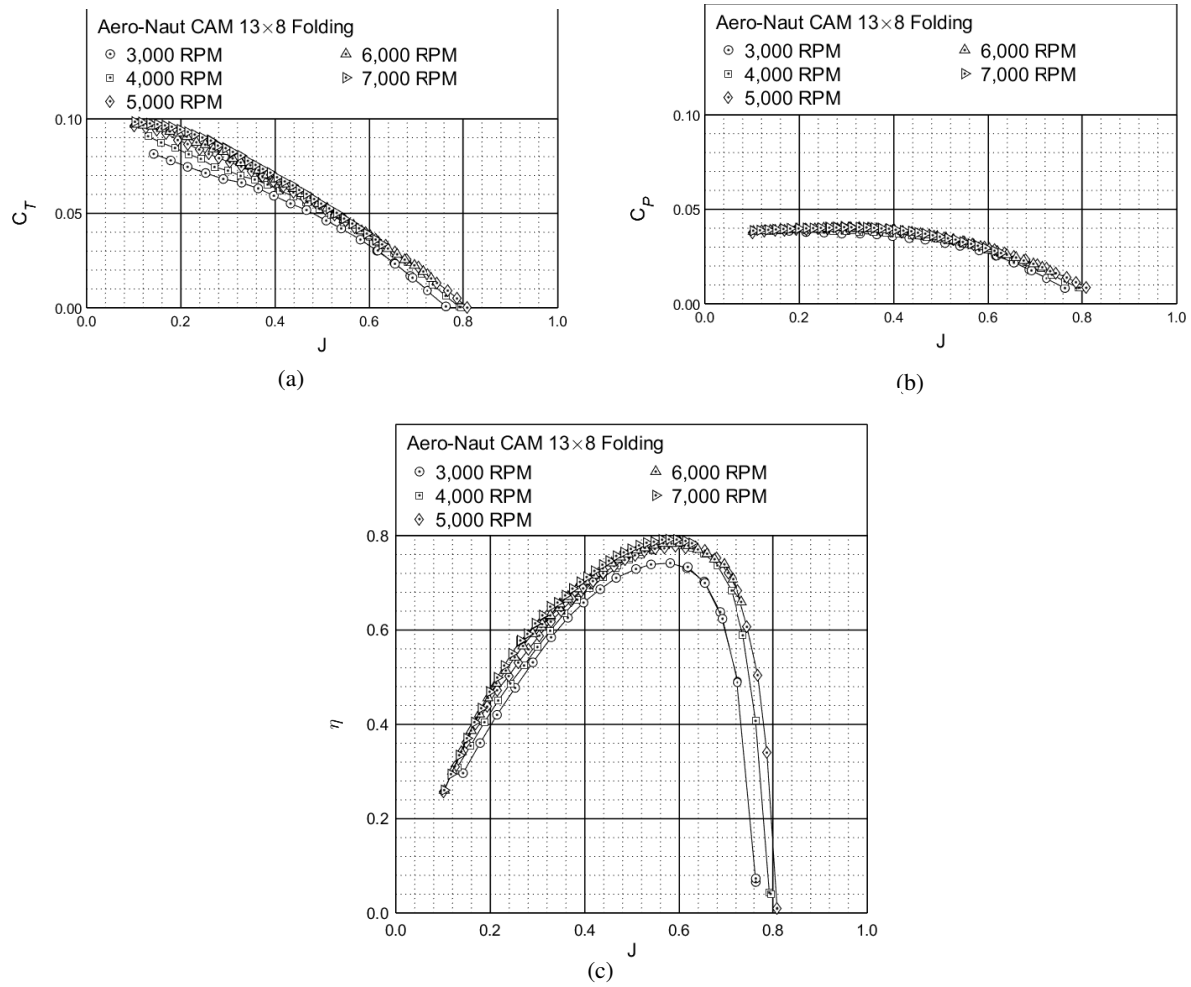
Figure 63: Performance of the Aero-Naut CAM 13×8 folding propeller: (a) thrust coefficient, (b) power coefficient, (c) efficiency.
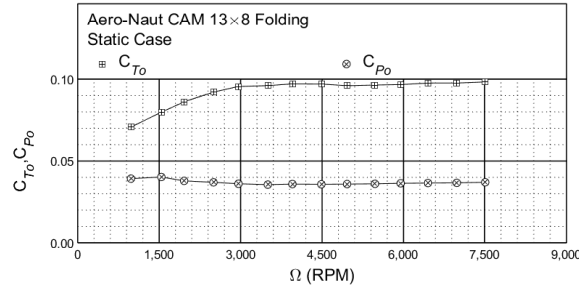
Figure 64: Static performance of the Aero-Naut CAM 13×8 folding propeller: thrust and power coefficient.

Aero-Naut CAM 13×10 Folding Propeller

(a)

(b)

(c)
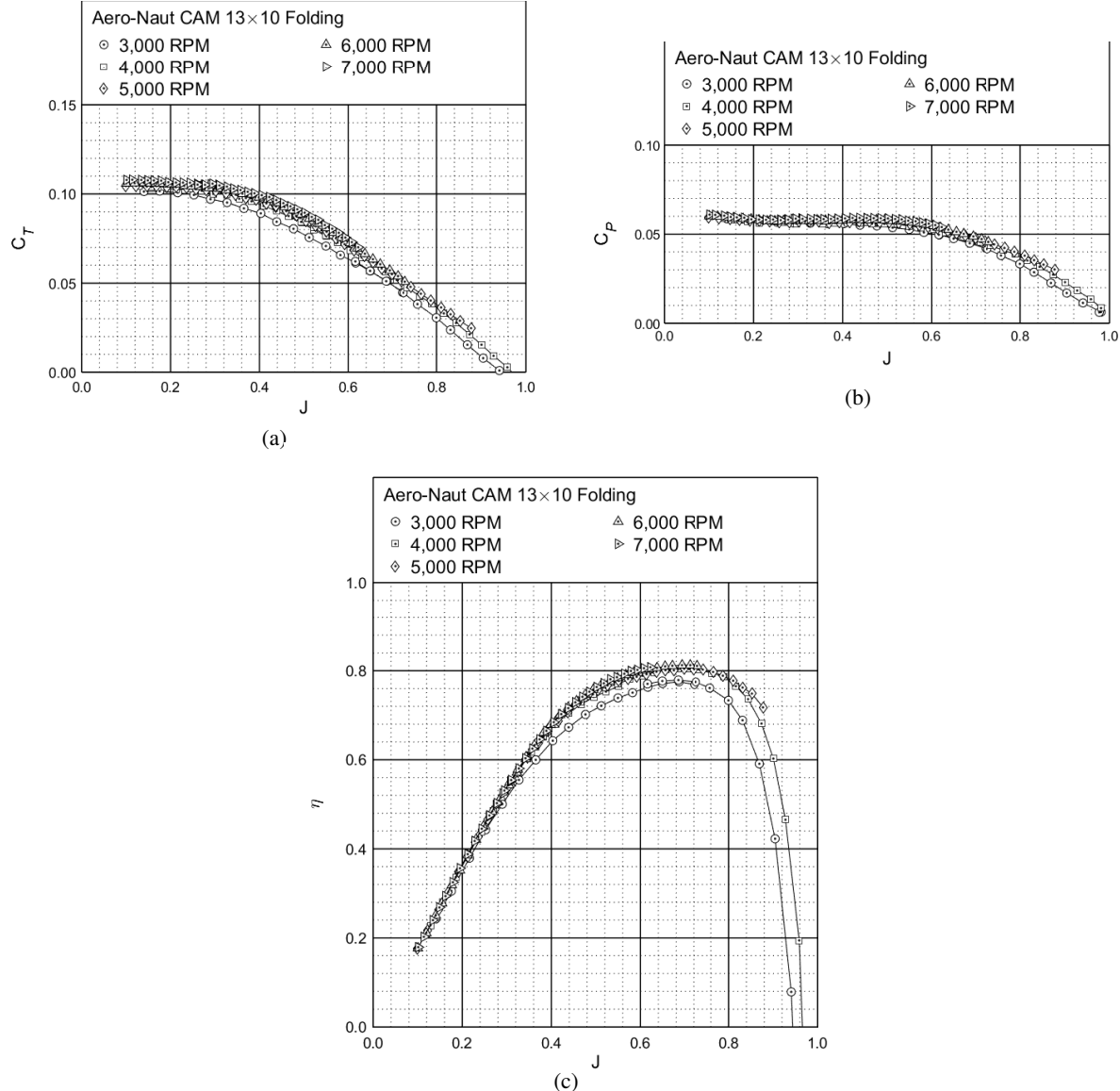
Figure 65: Performance of the Aero-Naut CAM 13×10 folding propeller: (a) thrust coefficient, (b) power coefficient, (c) efficiency.
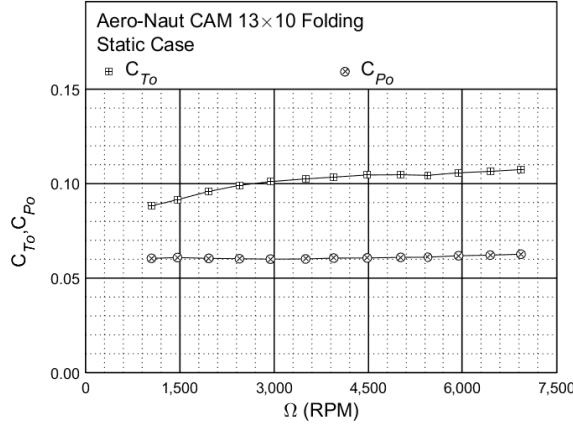
Figure 66: Static performance of the Aero-Naut CAM 13×10 folding propeller: thrust and power coefficient.

**Aero-Naut CAM 13×11 Folding Propeller**

(a)

(b)

(c)
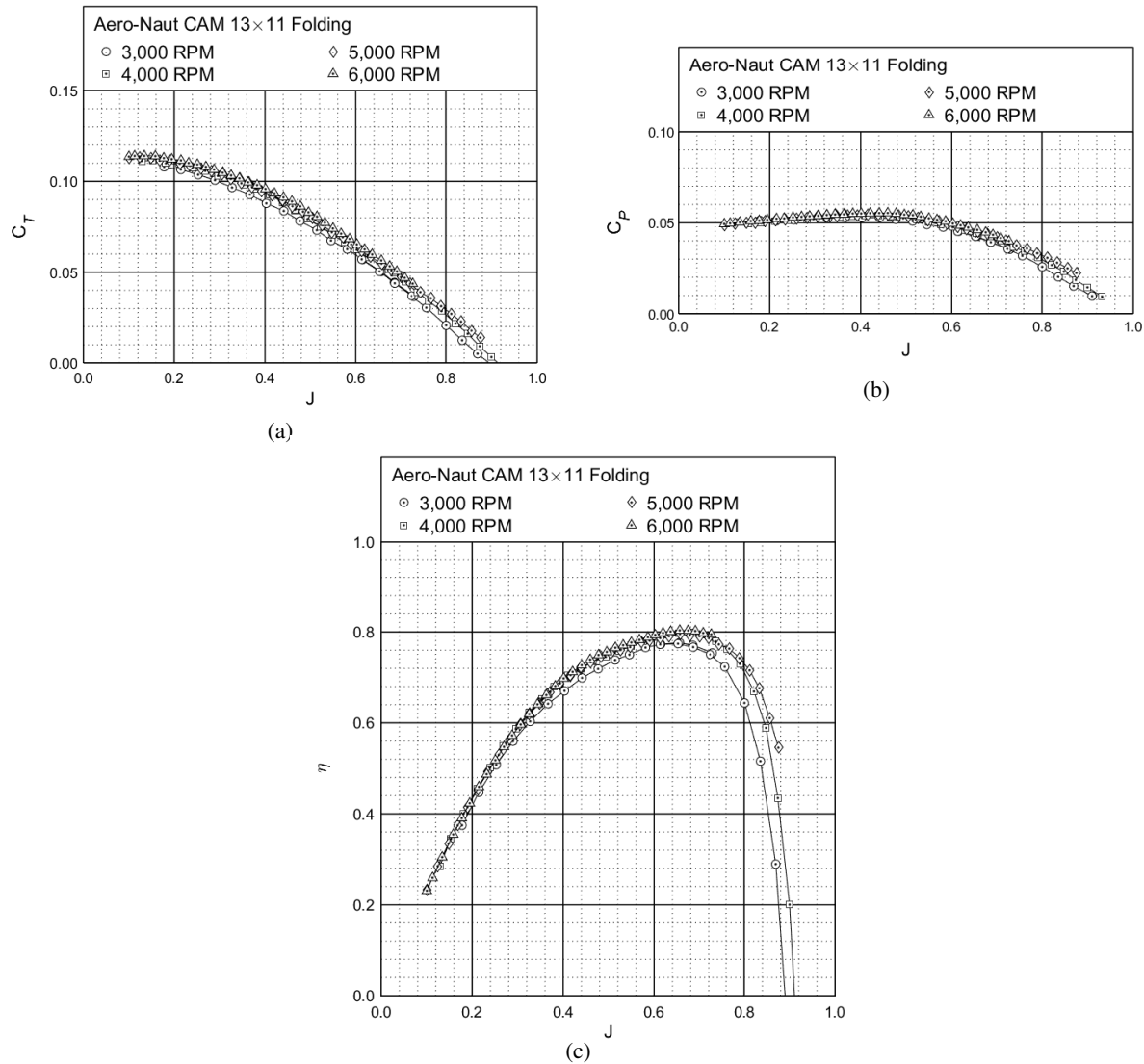
Figure 67: Performance of the Aero-Naut CAM 13×11 folding propeller: (a) thrust coefficient, (b) power coefficient, (c) efficiency.

American Institute of Aeronautics and Astronautics
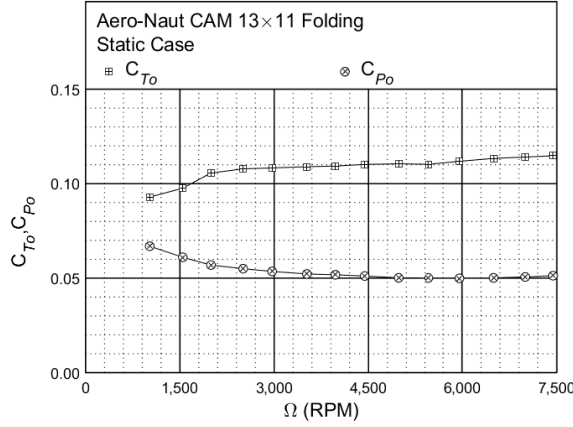
Figure 68: Static performance of the Aero-Naut CAM 13×11 folding propeller: thrust and power coefficient.

**Aero-Naut CAM 14×6 Folding Propeller**

(a)

(b)

(c)
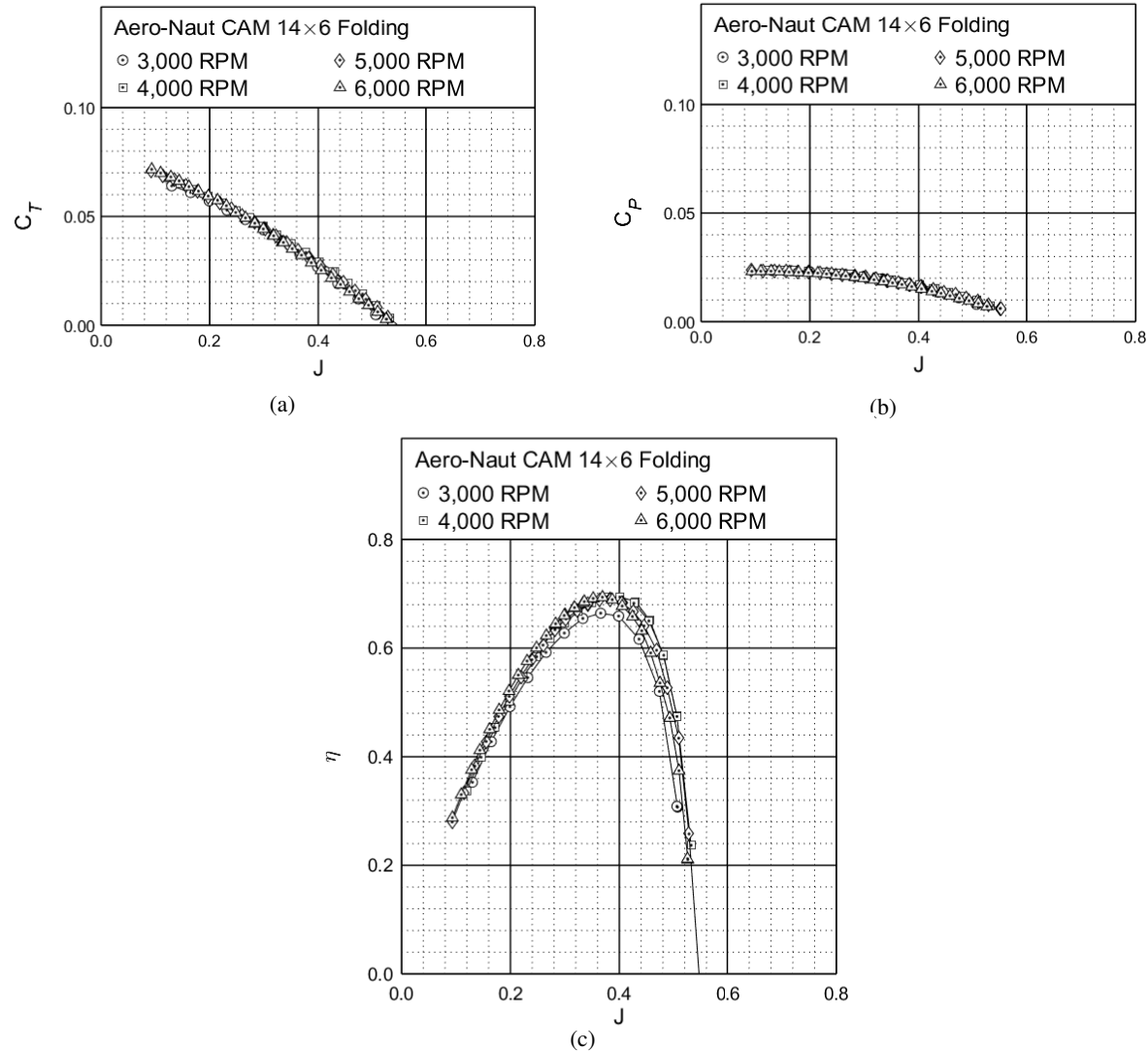
Figure 69: Performance of the Aero-Naut CAM 14×6 folding propeller: (a) thrust coefficient, (b) power coefficient, (c) efficiency.
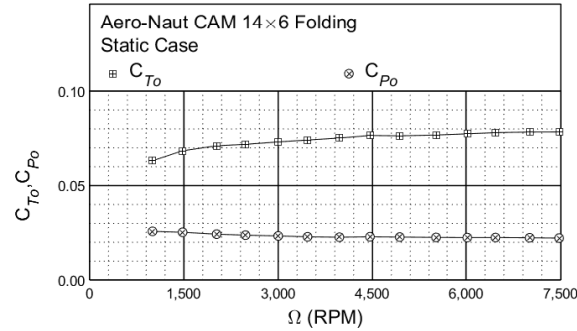
Figure 70: Static performance of the Aero-Naut CAM 14×6 folding propeller: thrust and power coefficient.

**Aero-Naut CAM 14×8 Folding Propeller**

(a)

(b)

(c)
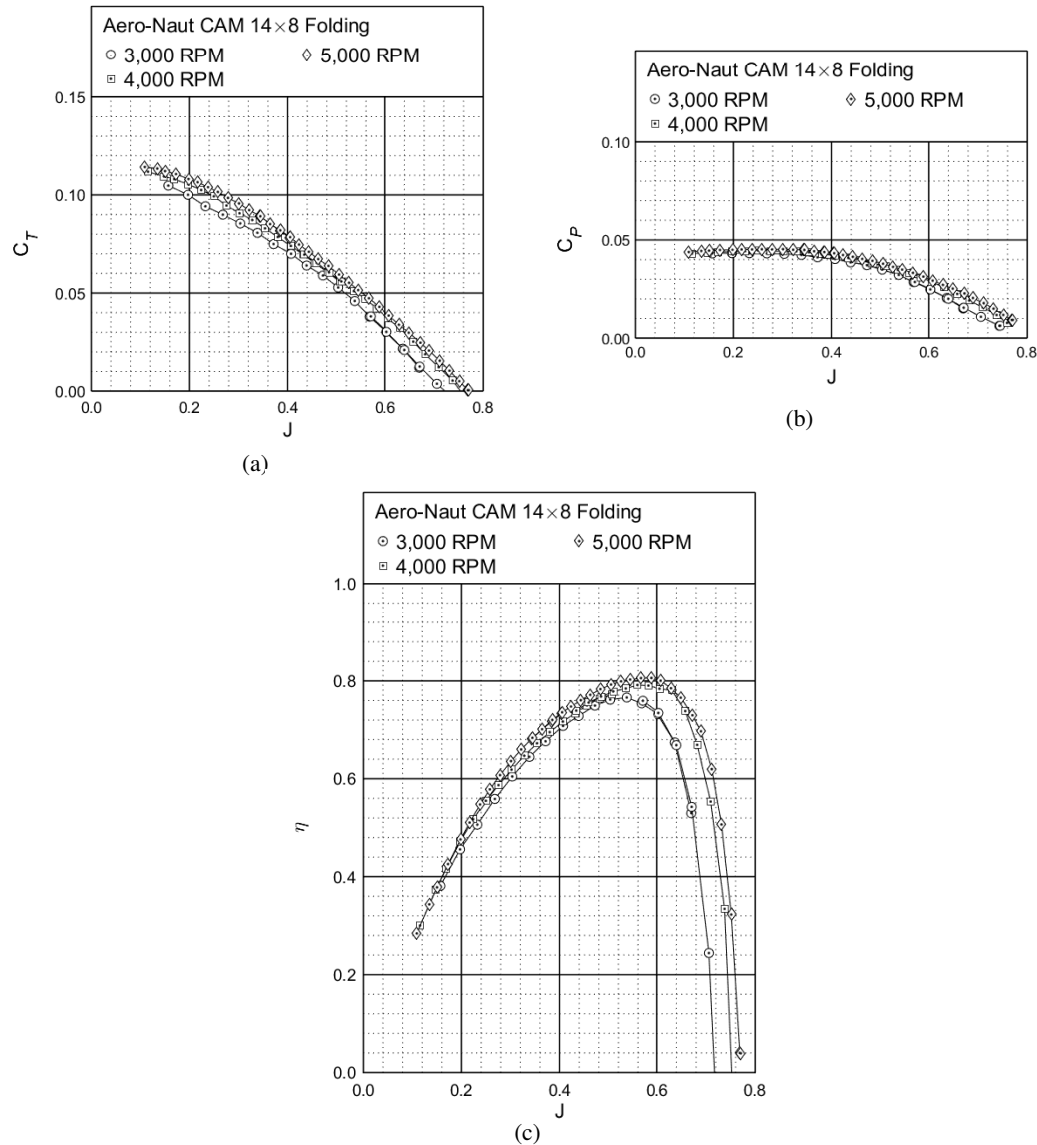
Figure 71: Performance of the Aero-Naut CAM 14×8 folding propeller: (a) thrust coefficient, (b) power coefficient, (c) efficiency.
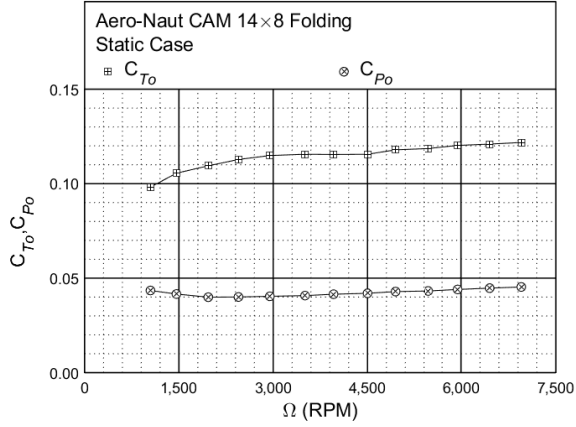
Figure 72: Static performance of the Aero-Naut CAM 14×8 folding propeller: thrust and power coefficient.

Aero-Naut CAM 14×9 Folding Propeller

(a)

(b)

(c)
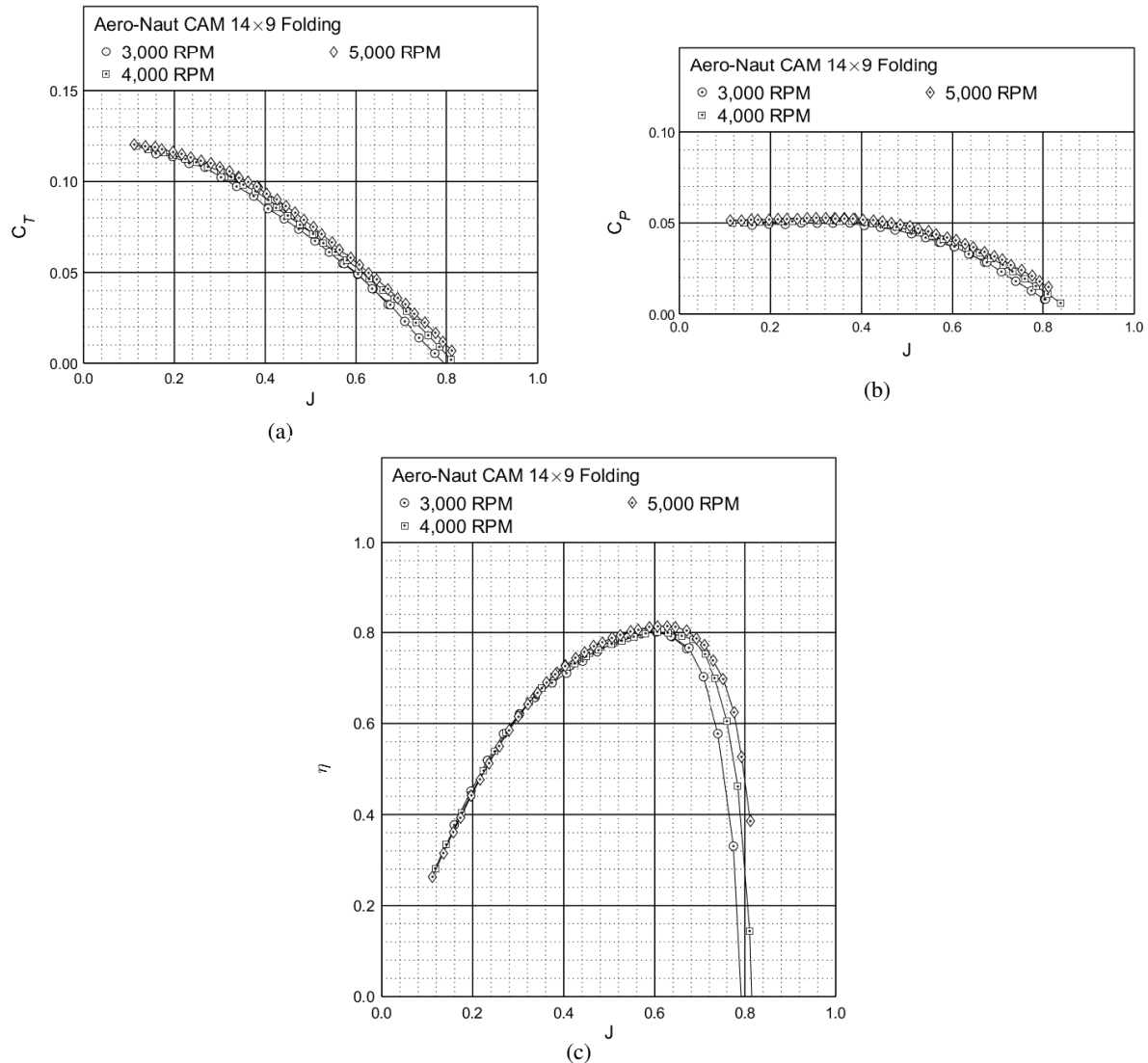
Figure 73: Performance of the Aero-Naut CAM 14×9 folding propeller: (a) thrust coefficient, (b) power coefficient, (c) efficiency.

American Institute of Aeronautics and Astronautics
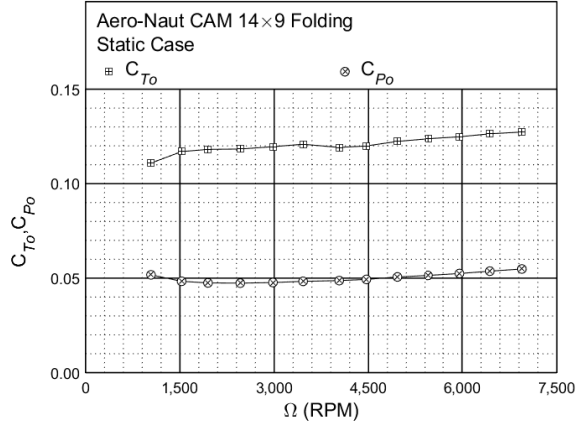
Figure 74: Static performance of the Aero-Naut CAM 14×9 folding propeller: thrust and power coefficient.

**Aero-Naut CAM 14×12 Folding Propeller**

(a)

(b)

(c)
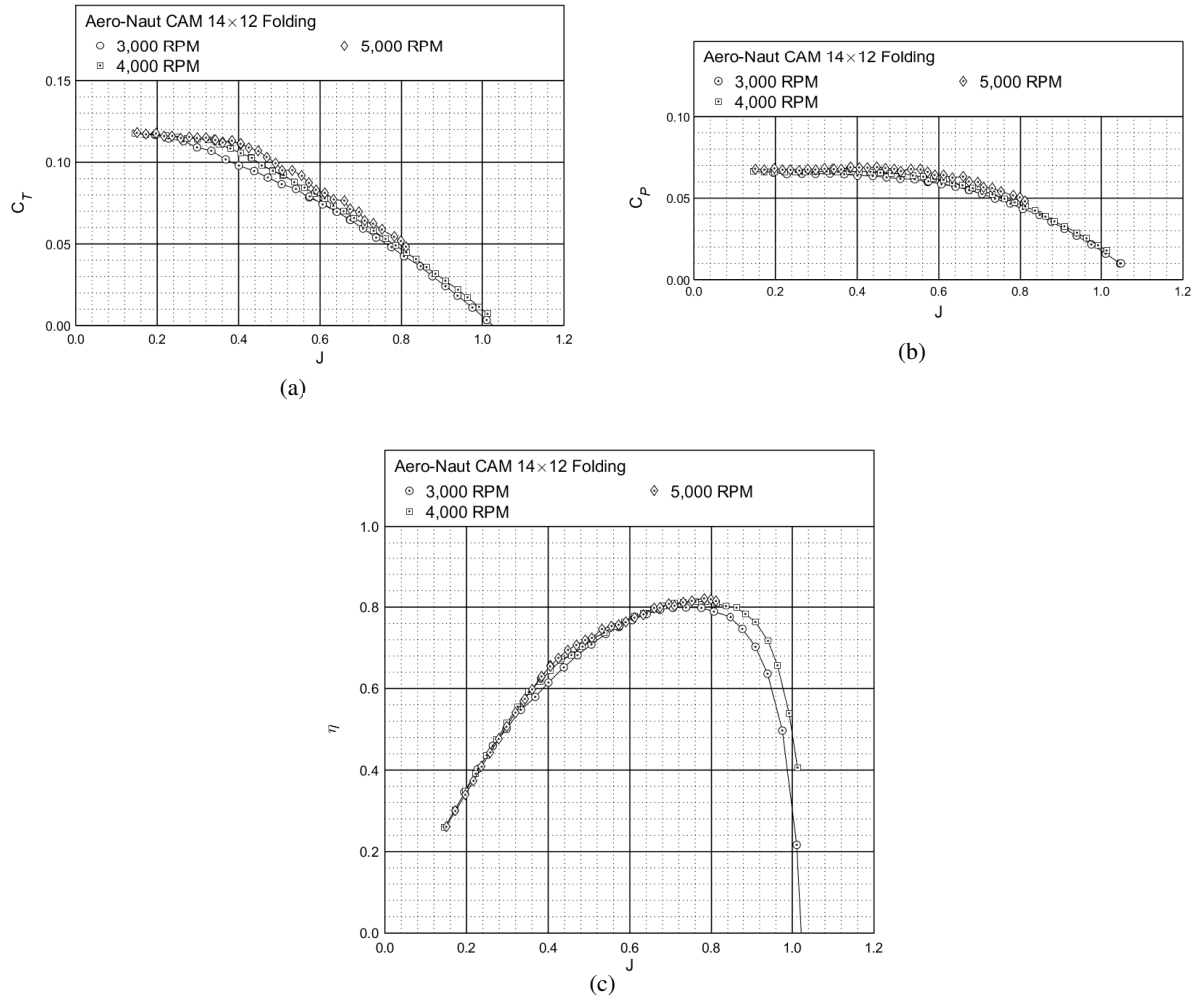
Figure 75: Performance of the Aero-Naut CAM 14×12 folding propeller: (a) thrust coefficient, (b) power coefficient, (c) efficiency.
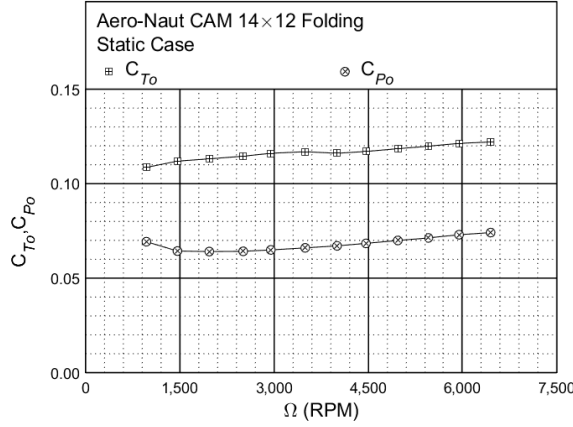
Figure 76: Static performance of the Aero-Naut CAM 14×12 folding propeller: thrust and power coefficient.

**Aero-Naut CAM 15×6 Folding Propeller**

(a)

(b)

(c)
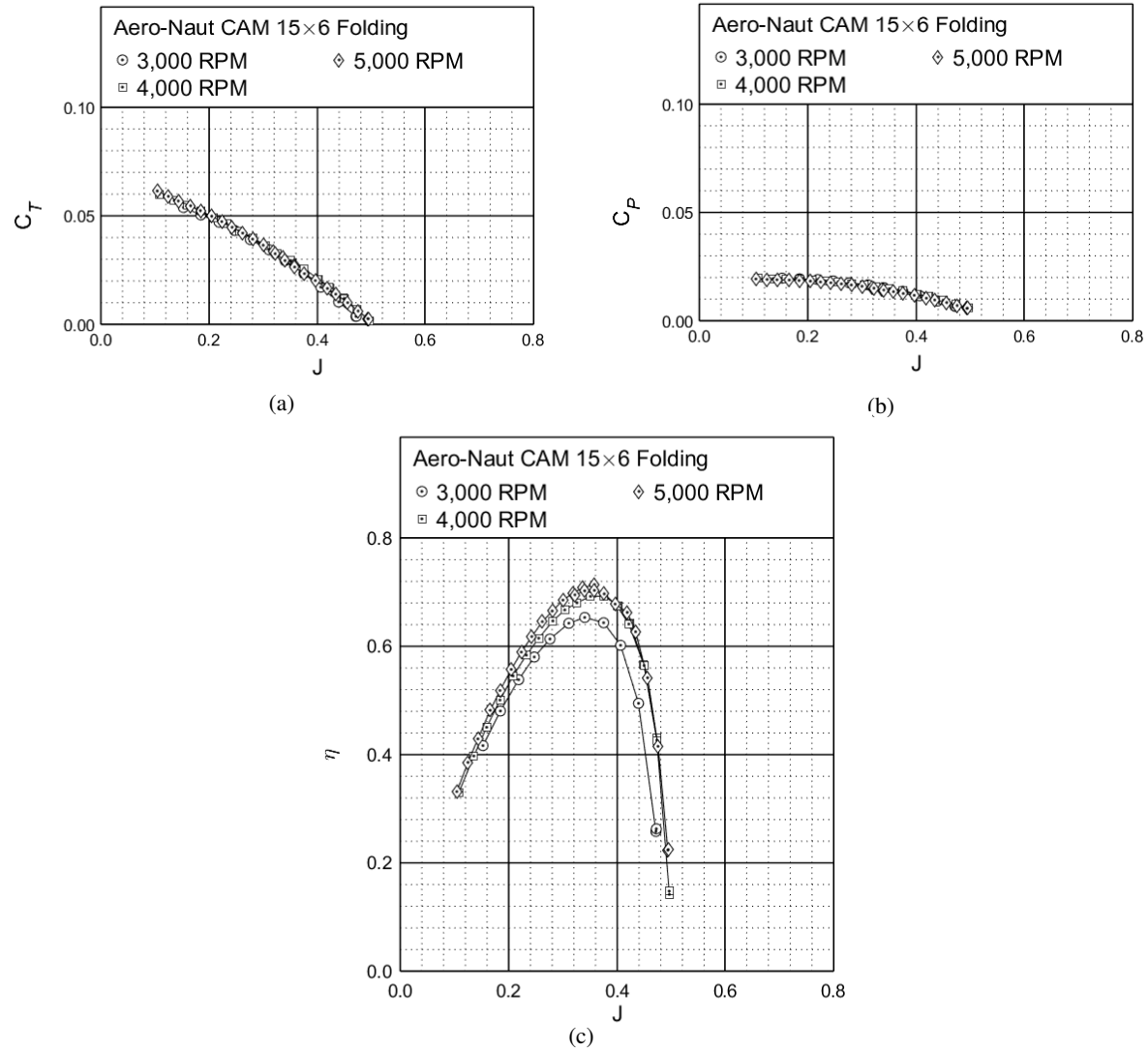
Figure 77: Performance of the Aero-Naut CAM 15×6 folding propeller: (a) thrust coefficient, (b) power coefficient, (c) efficiency.
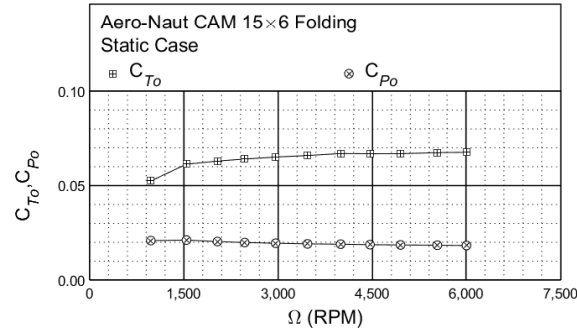
Figure 78: Static performance of the Aero-Naut CAM 15×6 folding propeller: thrust and power coefficient.

Aero-Naut CAM 15×8 Folding Propeller

(a)

(b)

(c)
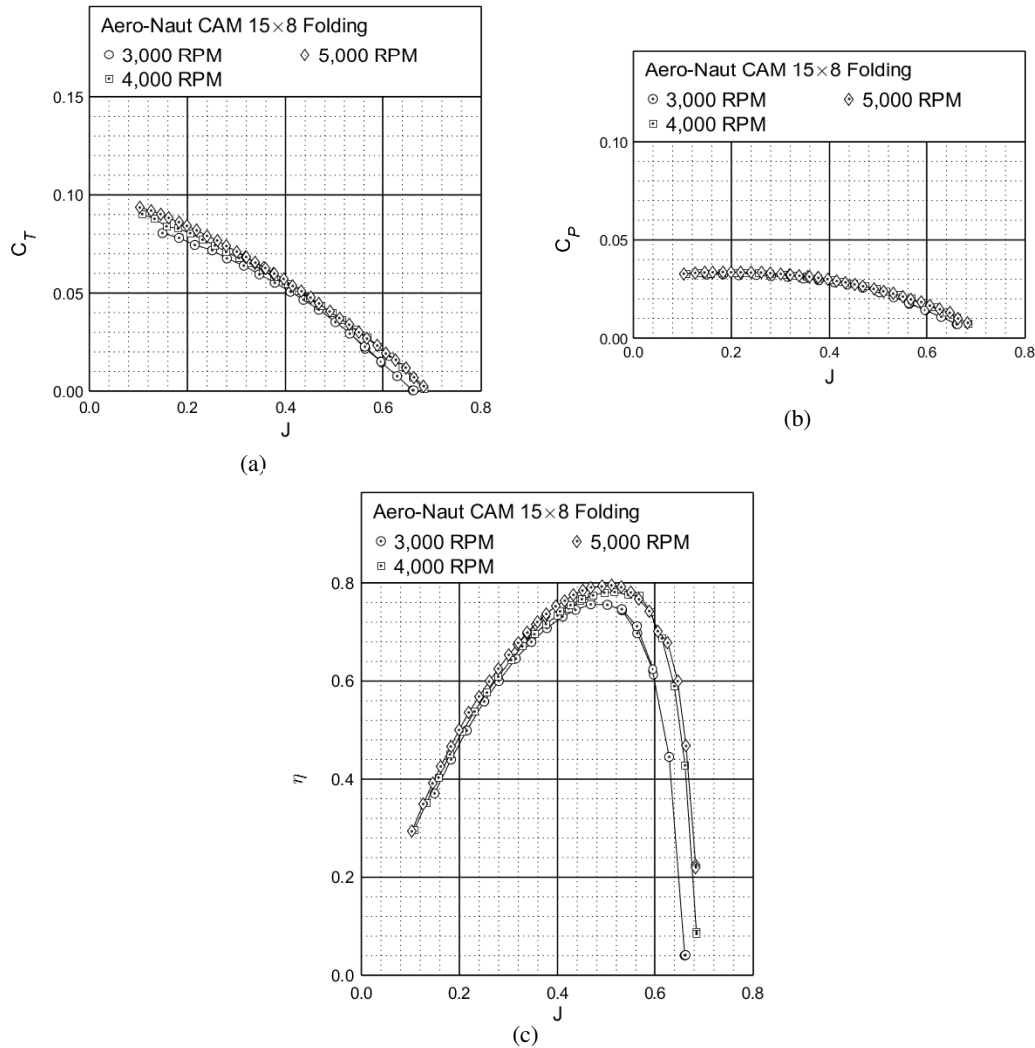
Figure 79: Performance of the Aero-Naut CAM 15×8 folding propeller: (a) thrust coefficient, (b) power coefficient, (c) efficiency.

American Institute of Aeronautics and Astronautics
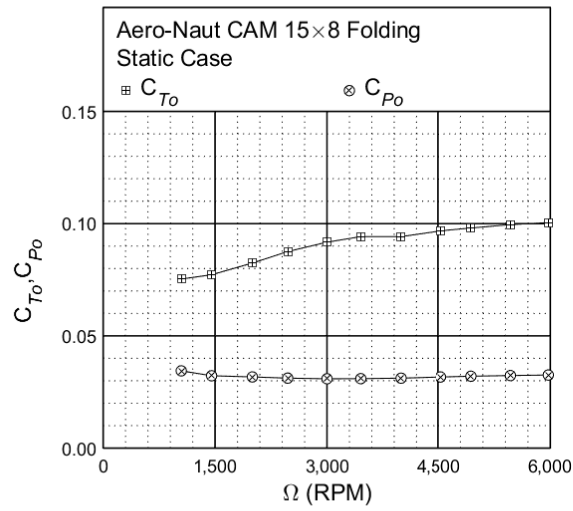
Figure 80: Static performance of the Aero-Naut CAM 15×8 folding propeller: thrust and power coefficient.

**Aero-Naut CAM 15×10 Folding Propeller**

(a)

(b)

(c)
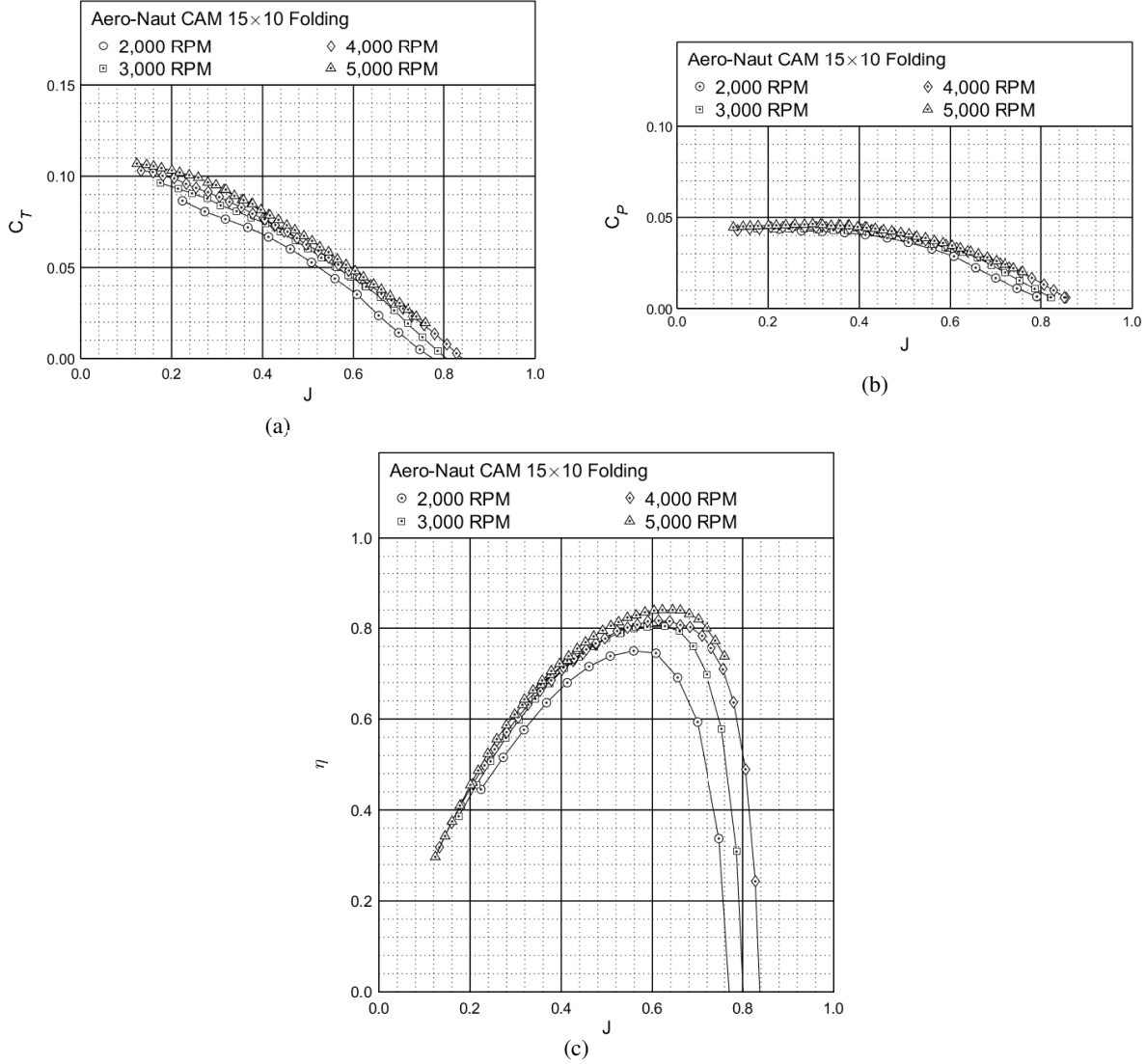
Figure 81: Performance of the Aero-Naut CAM 15×10 folding propeller: (a) thrust coefficient, (b) power coefficient, (c) efficiency.
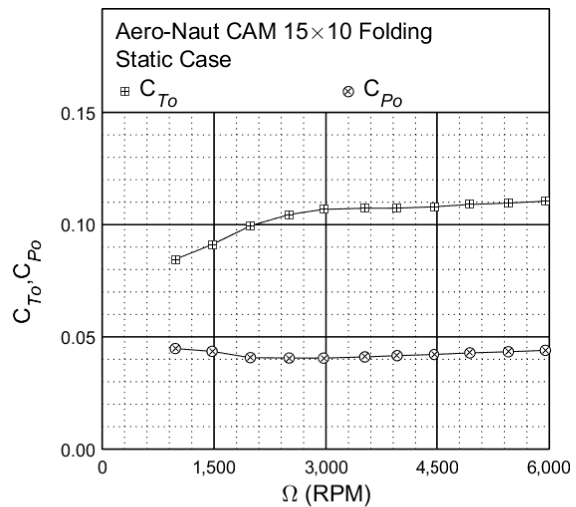

Figure 82: Static performance of the Aero-Naut CAM 15×10 folding propeller: thrust and power coefficient.

Aero-Naut CAM 16×6 Folding Propeller

(a)

(b)

(c)
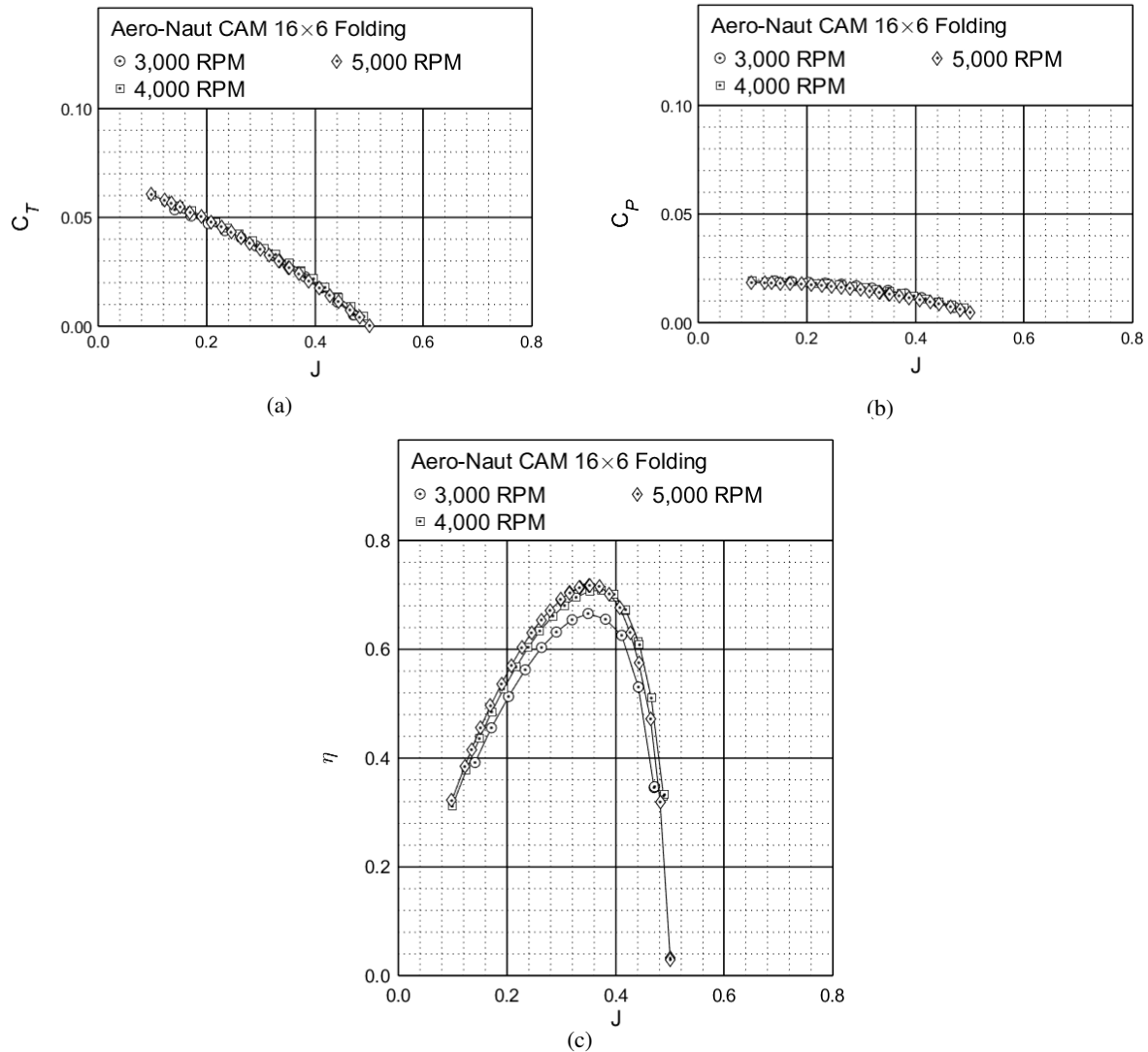
Figure 83: Performance of the Aero-Naut CAM 16×6 folding propeller: (a) thrust coefficient, (b) power coefficient, (c) efficiency.
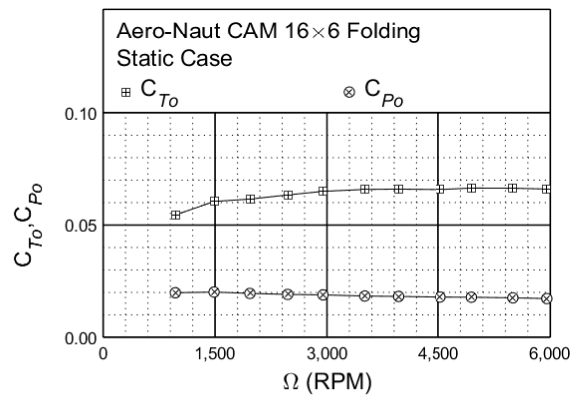
Figure 84: Static performance of the Aero-Naut CAM 16×6 folding propeller: thrust and power coefficient.

**Aero-Naut CAM 16×8 Folding Propeller**

(a)

(b)

(c)
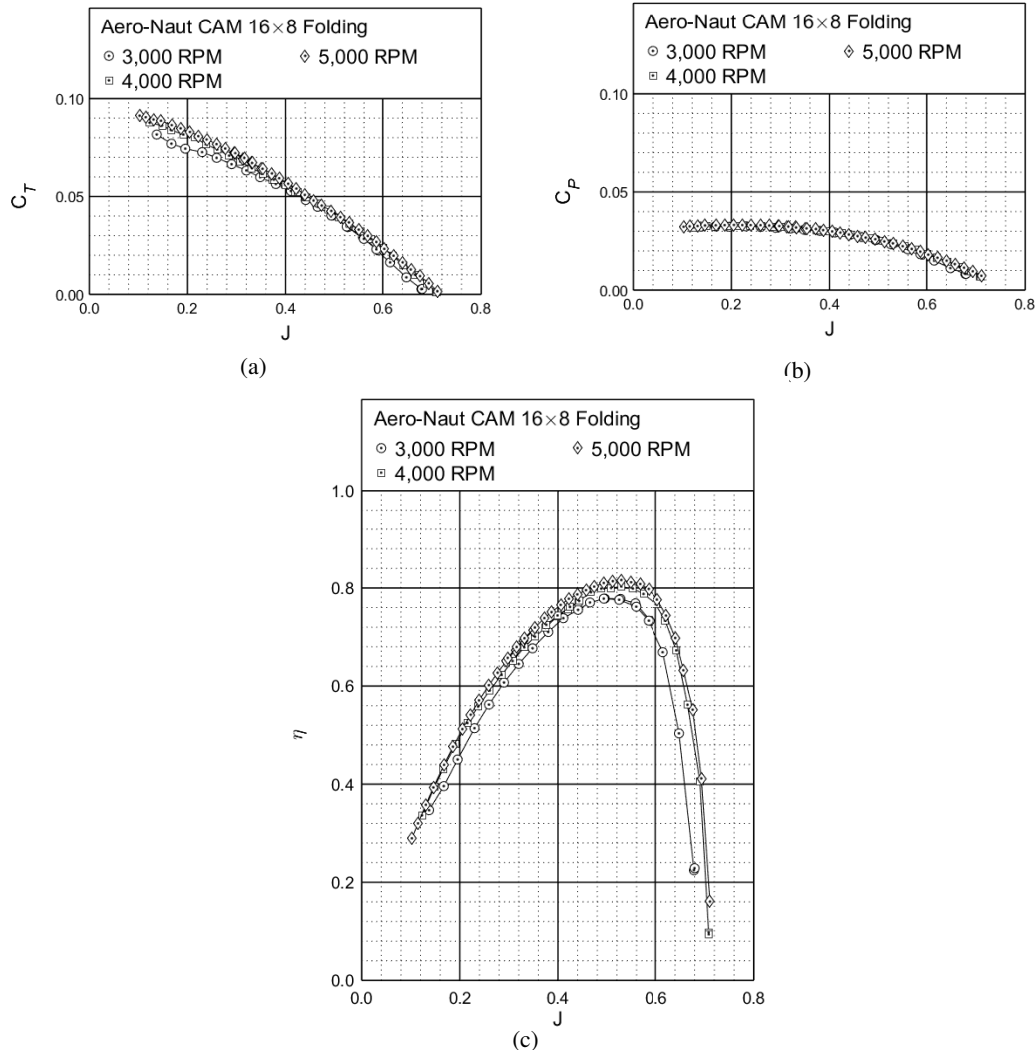
Figure 85: Performance of the Aero-Naut CAM 16×8 folding propeller: (a) thrust coefficient, (b) power coefficient, (c) efficiency.
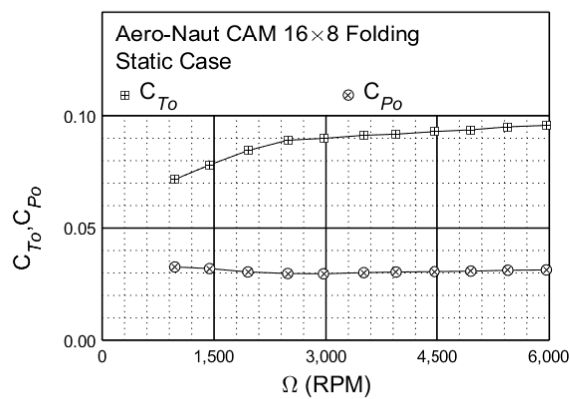

Figure 86: Static performance of the Aero-Naut CAM 16×8 folding propeller: thrust and power coefficient.

American Institute of Aeronautics and Astronautics

IV.   Summary and Future Work

This paper described the performance testing of 40 Aero-Naut CAM carbon folding propellers in 2-blade configuration with diameters of 9 to 16 in with various pitch values. The propellers were tested at rotation rates of 3,000 to 7,000 RPM and advancing flows of 8 to 80 ft/s, depending on the propeller and testing equipment limitations. The motivation of this testing was the optimization of a computationally-intensive, long-endurance, solar-power unmanned aircraft, the UIUC-TUM Solar Flyer. It was observed that Aero-Naut CAM carbon folding propeller blade geometry varied among propellers of the same diameter with different pitch values and among propellers of identical pitch-to-diameter ratios with different diameters. This geometry difference results in unique performance data for each propeller, therefore requiring individual performance testing of all propellers of interest. It was also found that increasing the pitch of a given diameter of propeller increases the non-dimensional performance and efficiency of the propeller, while shifting these characteristics toward higher advance ratios. The performance and efficiency increases continue with pitch until the propeller pitch-to-diameter ratio reaches approximately 0.8 to 1.0, after which the increase stabilizes, flattens over larger advance ratios, and sometimes then decreases. Similarly, for static conditions (zero velocity), increased propeller pitch increases thrust and power coefficients. Finally, Reynolds number effects were observed, with performance and efficiency increasing as RPM increases until a sufficiently high RPM is reached where there is marginal continued gain.

In future work, additional testing is planned in order to refine and broaden the range of possible propellers that can be optimally selected for efficient use on long-endurance aircraft, e.g. the UIUC-TUM Solar Flyer. Testing could be expanded for these aforementioned 40 Aero-Naut CAM carbon folding propellers at increased and decreased rotation rates and advance ratios, which likely correspond to certain flight conditions/profiles and could expose compressibility effects at higher RPM. Additionally, other Aero-Naut CAM carbon folding propeller diameter and pitch values should be tested. In this regard, it would also be of interest to test folding propellers from other manufactures to compare performance. Additional future work would also include measurement of the blade geometry (chord and twist distribution) for the tested propellers as well as future propellers that would be tested, allowing Reynolds number to be estimated. Finally, enabling testing at higher tunnel speeds would enable more complete performance and efficiency curves to be measured for high RPMs and for high pitch-to-diameter ratio propellers.

Acknowledgments

References

[1] "Altavian," http://www.altavian.com/, Accessed May 2020.

[2] Precision Hawk, "Precision Agriculture, Commercial UAV and Farm Drones," http://precisionhawk.com/, Accessed May 2020.

[3] MicroPilot, "MicroPilot - MP-Vision," http://www.micropilot.com/products-mp-visione.htm, Accessed May. 2015.

[4] Dantsker, O. D., Theile, M., and Caccamo, M., "Design, Development, and Initial Testing of a Computationally-Intensive, Long-Endurance Solar-Powered Unmanned Aircraft," AIAA Paper 2018-4217, AIAA Applied Aerodynamics Conference, Atlanta, GA, June 2018.

[5] Dantsker, O. D., Theile, M., Caccamo, M., Yu, S., Vahora, M., and Mancuso, R., "Continued Development and Flight Testing of a Long-Endurance Solar-Powered Unmanned Aircraft: UIUC-TUM Solar Flyer," AIAA Paper 2020-0781, AIAA SciTech Forum, Orlando, Florida, Jan. 2020.

[6]Real Time and Embedded System Laboratory, University of Illinois at Urbana-Champaign, "Solar-Powered Long-Endurance UAV for Real-Time Onboard Data Processing," http://rtsl-edge.cs.illinois.edu/UAV/, Accessed Jan. 2018.

[7]Dantsker, O. D., Imtiaz, S., and Caccamo, M., "Electric Propulsion System Optimization for Long-Endurance and Solar-Powered Unmanned Aircraft," AIAA Paper 2019-4486, 2019 AIAA/IEEE Electric Aircraft Technologies Symposium, Indianapolis, IN, Aug. 2019.

[8]aero-naut Modellbau GmbH & Co. KG, "CAMcarbon folding propellers," http://www.aero-naut.de/en/products/airplanes/accessories/propellers/camcarbon-folding-prop/, Accessed May 2020.

[9]Lockheed Martin Corporation, "Stalker XE UAS," https://www.lockheedmartin.com/en-us/products/stalker.html, Accessed May 2020.

[10]Silent Falcon UAS Technologies, "Silent Falcon," http://www.silentfalconuas.com/silent-falcon, Accessed May 2020.

[11]Zipline International, "Zipline - Lifesaving Deliveries by Drone," https://flyzipline.com/, Accessed May 2020.

[12]Israel Aerospace Industries Ltd., "Military Malat Products Bird Eye 400," http://www.iai.co.il/2013/36943-34720-en/Bird_Eye_Family.aspx, Accessed May. 2019.

[13]Brandt, J. B., *Small-Scale Propeller Performance at Low Speeds*, Master's thesis, University of Illinois at Urbana-Champaign, Department of Aerospace Engineering, Urbana, IL, 2005.

[14]Brandt, J. B. and Selig, M. S., "Propeller Performance Data at Low Reynolds Numbers," AIAA Paper 2011-1255, AIAA Aerospace Sciences Meeting, Orlando, Florida, Jan. 2011.

[15]Uhlig, D. V., *Post Stall Propeller Behavior at Low Reynolds Numbers*, Master's thesis, University of Illinois at Urbana-Champaign, Department of Aerospace Engineering, Urbana, IL, 2007.

[16]Uhlig, D. V. and Selig, M. S., "Post Stall Propeller Behavior at Low Reynolds Numbers," AIAA Paper 2008-407, AIAA Aerospace Sciences Meeting, Reno, NV, Jan. 2008.

[17]Lundstrom, D., *Aircraft Design Automation and Subscale Testing*, Ph.D. thesis, Linkoping University, Department of Management and Engineering, Linkoping, Sweden, 2012.

[18]Lundstrom, D. and Krus, P., "Testing of Atmospheric Turbulence Effects on the Performance of Micro Air Vehicles," *International Journal of Micro Air Vehicles*, Vol. 4, No. 2, Jun. 2012, pp. 133–149.

[19]Deters, R. W. and Selig, M. S., "Static Testing of Micro Propellers," AIAA Paper 2008-6246, AIAA Applied Aerodynamics Conference, Honolulu, HI, Aug. 2008.

[20]Deters, R. W., *Performance and Slipstream Characteristics of Small-Scale Propelllers at Low Reynolds Numbers*, Ph.D. thesis, University of Illinois at Urbana-Champaign, Department of Aerospace Engineering, Urbana, IL, 2014.

[21]Deters, R. W., Kleinke, S., and Selig, M. S., "Static Testing of Propulsion Elements for Small Multirotor Unmanned Aerial Vehicles," AIAA Paper 2017-3743, AIAA Aviation Forum, Denver, CO, June 2017.

[22]Deters, R. W., Dantsker, O. D., Kleinke, S., Norman, N., and Selig, M. S., "Static Performance Results of Propellers Used on Nano, Micro, and Mini Quadrotors," AIAA Paper 2018-4122, AIAA Aviation Forum, Atlanta, GA, June 2018.

[23]Lindahl, P., Moog, E., and Shaw, S. R., "Simulation, Design, and Validation of an UAV SOFC Propulsion System," *IEEE Transactions on Aerospace and Electronic Systems*, Vol. 48, No. 3, Jul. 2012, pp. 2582–2593.

[24]Chaney, C. S., Bahrami, J. K., Gavin, P. A., Shoemake, E. D., Barrow, E. S., and Matveev, K. I., "Car-Top Test Module as a Low-Cost Alternative to Wind Tunnel Testing of UAV Propulsion Systems," *Journal of Aerospace Engineering*, Vol. 27, No. 6, Nov. 2014.

[25]Dantsker, O. D., Selig, M. S., and Mancuso, R., " A Rolling Rig for Propeller Performance Testing," AIAA Paper 2017-3745, AIAA Applied Aerodynamics Conference, Denver, CO, June 2017.

[26]Dantsker, O. D., Deters, R. W., and Caccamo, M., "Propulsion System Testing for a Long-Endurance Solar-Powered Unmanned Aircraft," AIAA Paper 2019-3688, AIAA Aviation and Aeronautics Forum and Exposition, Dallas, TX, June 2019.

[27]Drela, M., "DC Motor / Propeller Matching," http://web.mit.edu/drela/Public/web/qprop/motorprop.pdf, Accessed May 2020.

[28]Drela, M., "First-Order DC Electric Motor Model," http://web.mit.edu/drela/Public/web/qprop/motor1_theory.pdf, Accessed May 2020.

[29]Drela, M., "Second-Order DC Electric Motor Model," http://web.mit.edu/drela/Public/web/qprop/motor2_theory.pdf, Accessed May 2020.

[30]Green, C. R. and McDonald, R. A., "Modeling and Test of the Efficiency of Electronic Speed Controllers for Brushless DC Motors," AIAA Paper 2015-3191, AIAA Aviation Forum, Dallas, TX, Jun. 2015.

[31]Gong, A. and Verstraete, D., "Experimental Testing of Electronic Speed Controllers for UAVs," AIAA Paper 2017-4955, AIAA/SAE/ASEE Joint Propulsion Conference, Atlanta, GA, July 2017.

[32]Gong, A., MacNeill, R., and Verstraete, D., "Performance Testing and Modeling of a Brushless DC Motor, Electronic Speed Controller and Propeller for a Small UAV," AIAA Paper 2018-4584, AIAA Propulsion and Energy Forum, Cincinnati, OH, July 2018.

[33]Gong, A., Maunder, H., and Verstraete, D., "Development of an in-fight thrust measurement system for UAVs," AIAA Paper 2017-5092, AIAA/SAE/ASEE Joint Propulsion Conference, Atlanta, GA, July 2017.

[34]Deters, R. W., Ananda, G. K., and Selig, M. S., "Reynolds Number Effects on the Performance of Small-Scale Propellers," AIAA Paper 2014-2151, AIAA Applied Aerodynamics Conference, Atlanta, GA, Jun. 2014.

[35]Khodadoust, A., "An Experimental Study of the Flowfield on a Semispan Rectangular Wing with a Simulated Glaze Ice Accretion," Ph.D. Thesis, University of Illinois at Urbana-Champaign, Urbana, IL, 1993.

[36]Anderson, J.D., Jr., *Fundamentals of Aerodynamics*, 2nd ed., McGraw-Hill, Inc., New York, 1991.

[37]Glauert, H., "Wind Tunnel Interference on Wings, Bodies and Airscrews," Aeronautical Research Committee R&M 1566, 1933.

[38]Barlow, J.B., Rae, W.H., Jr., and Pope, A., *Low-Speed Wind Tunnel Testing*, 3rd ed., John Wiley & Sons, Inc., New York, 1999.

[39]UIUC Applied Aerodynamics Group, "UIUC Propeller Data Site," http://m-selig.ae.illinois.edu/props/propDB.html.

[40]Dantsker, O. D., Mancuso, R., Vahora, M., and Caccamo, M., "Unmanned Aerial Vehicle Database," http://www.uavdb.org.